Prolate Spheroidal Sequence Based Transceivers for Time-Frequency Dispersive Channels

Karim A. Said

Dissertation submitted to the Faculty of the

Virginia Polytechnic Institute and State University

in partial fulfillment of the requirements for the degree of

Doctor of Philosophy

In

Electrical Engineering

A. A. (Louis) Beex, Chair

Lamine M. Mili

Peter M. Athanas

Harpreet Singh Dhillon

Mazen H. Farhood

May 10, 2017

Blacksburg, VA

Keywords: Doubly Dispersive Channels, Discrete Prolate Spheroidal Sequences, Banded Matrices

Prolate Spheroidal Sequence Based Transceivers for Time-Frequency Dispersive Channels

Karim A. Said

ABSTRACT

Most existing transceivers are Fourier-centric where complex sinusoids play a central role in the internals of the core building blocks. From the channel perspective, complex sinusoids constitute the fundamental effects in the wireless baseband equivalent channel model; exemplified by the time-invariant and time-varying transfer functions in static and time-varying channel conditions respectively. In addition, complex sinusoids are used as signaling waveforms for data transmission through the channel.

The dominant mode of transmission in modern communications is in the form of finite time duration blocks having approximately finite bandwidth. As a result, the time-frequency space becomes projected to a time-frequency subspace having essentially limited support where complex sinusoids suffer from leakage effects due to the finite time extent of a block. In addition, Kronecker delta signals (duals of complex sinusoids) suffer from the same vulnerability due to the finite extent bandwidth. Gabor signaling bases using non-rectangular pulse shapes can attain good confinement in the time-frequency space, however, at the expense of completeness which reduces the utilization efficiency of the time-frequency signaling resources.

Over a signaling block period, a doubly dispersive (DD) channel is projected onto an essentially limited time-frequency subspace. In this subspace, the Discrete Prolate Spheroidal (DPS) basis matched to the channel parameters is known to be optimally compact in representing the channel using a basis expansion decomposition. Unlike the Discrete Fourier Transform (DFT) basis which lacks compactness due to the leakage effect.

Leakage in the expansion coefficients of a particular channel using the DFT basis has a direct correspondence with the Inter-symbol Interference (ISI) between the DFT signaling

components when transmitted through the same channel. For the DPS basis, however, the correspondence is not as obvious. Nevertheless, DPS when used for signaling results in ISI compactness in the form of an exponential decay of distant ISI components.

The efficacy of DPS signaling in DD channels in addition to its efficiency in modeling DD channels motivates the investigation of a new transceiver baseband architecture where DFT is supplanted by DPS.

Prolate Spheroidal Sequence Based Transceivers for Time-Frequency Dispersive Channels

Karim A. Said

ABSTRACT (General Audience)

Radio communication technology is undeniably a vital organ in modern societies, witnessed by its compelling socio-economic impact. Social media terms such as Facebook and Twitter, etc., have spurred a trans-geographical neologism in the vernacular of nations across the globe. This is all thanks to the seamless ubiquity afforded by untethered wireless communication technology.

High data rate wireless communication for nomadic modes of operation, movement across locations with intermittent dwelling, has been an uncontested success. However, the quality of communications while on the move at ambitiously high speeds, up to 500Km/h, is a completely different state of affairs.

Orthogonal Frequency Division Multiplexing (OFDM) is the working horse technology driving all modern communication systems including Bluetooth, WiFi, 4G Long Term Evolution (LTE), High Definition TV broadcast (HDTV) and more.

As the adage goes “no one size fits all”, OFDM so far has been the size that fits nomadic and relatively slow mobility modes of operation which correspond to the majority of behavior patterns of communicating entities. However, scenarios that rely on high mobility modes are gradually moving out of the fringes and into the center scene, examples being Wide-band Vehicle-to-Vehicle (V2V) and Vehicle-to-Anything (V2X) communication.

Because of OFDM’s inadequacy in such high mobility conditions, both academic and industrial bodies have embarked on their research efforts to investigate signaling schemes resilient to hostile channel effects that arise in high mobility conditions. The thesis of this work is that Discrete Prolate Spheroidal (DPS) Sequences is the most suitable candidate from the list of competitors, DPS being our discovery, that has been presented by the

research community so far. We provide both theoretical arguments to demonstrate the essential merits of DPS as well as case-specific simulations to demonstrate its efficacy.

ACKNOWLEDGEMENTS

I have never been good at expressing my emotions in words because I always believed that actions speak louder than words, but here goes.

Thank you Dr. Beex for dispelling the morbid worldview governed by the principle that *"No good deed goes unpunished"*. Thank you for going against all odds and helping a struggling eagle after his wings have been shattered. Indeed, your good deeds will always be remembered and honored.

During my PhD journey, I observed how you stoically dealt with the loss of a potential achievement. I learned from you how not to get emotionally attached to one's desire to achieve, but to tread gently and slowly and, most importantly, conscientiously towards one's goal. And to relentlessly get up after getting knocked down. Thank you for everything.

My thanks go to Dr. Lamine M. Mili, Dr. Harpreet S. Dhillon, Dr. Peter M. Athanas and Dr. Mazen Farhood for giving me the honor of being on my committee.

Last but not least, I would like to thank my family for being supportive during my PhD journey and tolerating my negative inclinations. Special thanks go to my elder sister, Dina, who always helped me when I was in need.

TABLE OF CONTENTS

LIST OF FIGURES

LIST OF TABLES

LIST OF ABBREVIATIONS

AWGN	Additive White Gaussian Noise
BEM	Basis Expansion Model
BTI	Block Time Invariant
BLE	Block Linear Equalizer
CE-BEM	Complex Exponential Basis Expansion Model
CEE	Channel Estimation Error
CP	Cyclic Prefix
CSI	Channel State Information
DD	Doubly Dispersive
DFT	Discrete Fourier Transform
DPS	Discrete Prolate Spheroidal
DoVD	Direction of Velocity Diversity
ICC	Inverse Channel Condition
ICI	Inter-Carrier Interference
IoT	Internet-of-Things
ISI	Inter-Symbol Interference
JABR	Joint Aprroximate Bandwidth Reduction
KD	Kronecker Delta

LS	Least Squares
LTV	Linear Time-Varying
MIMO	Multiple Input Multiple Output
MKD	Multi-Kronecker Delta
MMSE	Minimum Mean Square Error
NMSE	Normalized Mean Square Error
OFDM	Orthogonal Frequency Division Multiplexing
ONB	Orthonormal Basis
PDP	Power Delay Profile
PR	Pilot Restoration
R-ICI	Residual Inter Component Interference
RMS	Root Mean Square
RSS	Received Signal Strength
RTV	Rapidly Time Varying
SER	Symbol Error Rate
SIMO	Single Input Multiple Output
SKD	Single Kronecker Delta
TI	Time Invariant
TV	Time Variant
WSSUS	Wide-Sense Stationary Uncorrelated Scattering

ZP	Zero Prefix

CHAPTER 1 INTRODUCTION

1.1 Outline and Overview

A communication signal is commonly represented as a function over the time-frequency space. However, this representation is paradoxical since changes in the signal along the time axis are not independent from the frequency of the signal, and therefore time and frequency cannot be treated simultaneously as independent variables. In a strictly mathematical sense, the time-frequency independent treatment is valid for functions that belong to an admissible set.

A sufficient admissibility condition can be defined in terms of a conceptual 2-D grid on the time-frequency plane. A signal is allowed to exist at a certain frequency on the grid and vary in time independently, i.e. its frequency is considered unchanged, as long as the time variation over the grid step along the time axis is negligible. OFDM is an example that satisfies the admissibility condition where the block period (OFDM symbol period) corresponds to the grid step along the time axis and its reciprocal is the step along the frequency axis. Frequency subcarriers exist along the grid in the y-axis direction and have a constant envelope for the whole period of the grid step along the time axis.

In time-varying channel conditions, time variations caused by the channel are imposed on the signal. If the time variation within a block period is negligible, such that the 2-D grid condition is not violated, the time-frequency independent treatment remains valid. However, when the time variation imposed by the channel is such that the rate of change is comparable to the frequency resolution of the grid, the time-frequency independent treatment is no longer valid.

For rapidly time-varying channel conditions, the grid resolution in the time domain can be increased to make the independent time-frequency treatment valid. However, increasing the resolution in the time domain leads to a reduction of resolution in the frequency domain.

While the time and frequency resolutions of the grid cannot be both increased due to their inverse proportionality relationship, the dispersion effects of the channel in time and frequency can both independently increase. As a result a channel condition can arise for which a grid resolution does not exist that validly accommodates the independent time-frequency treatment. In such a case, the distinction between variation over time and frequency becomes impossible and a single variable treatment, either time or frequency, must be used.

In Chapter 2, Doubly Dispersive channels and their mathematical representation as a linear operator having four possible forms is examined in detail. Two signaling parameters of central importance are block duration and bandwidth, which determine the granularity of the discretization of the channel operator to matrix form. The matrix form serves as the basis for the receiver processing operations, including channel estimation and equalization. Using appropriate matrix decompositions, the essential dimensionality of the channel can be captured which then allows for the use of efficient pilot schemes for channel estimation. The channel matrix structure determines the ISI between symbols in addition to the degree of data to pilot contamination which compromises channel estimation.

The essential dimensionality of the channel is not immediately exposed in the time and frequency domains, i.e. the time varying transfer function, but is embedded in the Doppler-Delay domain. The essential dimensions of the channel represent the minimum information required to uniquely identify a channel and hence the number of probing signals required.

To expose the essential dimensionality of the channel, a BEM is used which reduces the degrees of freedom (BEM coefficients) to a number approaching the dimensionality of the channel. The more agreement between a channel's BEM representation and the actual channel the closer the agreement between the number of degrees of freedom and the actual channel dimensionality.

A widely used model for the channel is based on a superposition of specular paths, each of which corresponds to a delayed and Doppler shifted version of the signal depending on the length of the path and the angle of signal arrival/departure respectively. The specular path model in the time-varying transfer function form corresponds to a BEM model with the

minimum number of coefficients. However, unlike other BEMs the basis components in the specular path model are not fixed, thus adding another dimension in terms of degrees of freedom.

BEMs with fixed bases require the least number of degrees of freedom when minimum a priori information – which consists of max delay and Doppler values – about the channel is known. Cisoidal components in time and frequency being the constituents of the specular path model suggests that a 2-D Fourier basis BEM is a suitable model. However, due to the leakage effects that Fourier bases suffer from when used over finite blocks, compactness is compromised. Discrete Prolate Spheroidal (DPS) bases which are eigenfunctions of the finite length Fourier transform are optimal bases with regards to compactness when minimal a priori knowledge about the channel is available.

Chapter 3 contains a detailed look at the characteristic properties of DPS sequences and the ramifications of using a DPS BEM on channel estimation. The DPS expansion coefficients can be divided into two sets: a set of coefficients of significant magnitude and a set of coefficients with decaying magnitudes known as transition coefficients. The cardinality of the set of significant coefficients is equal to the essential dimensionality of the channel and is typically assumed to be sufficient for representing the channel. However, the coefficients in the transition set are not insignificant and – if ignored – can have a considerable effect on the channel estimation accuracy.

Incorporating some of the transition coefficients in the channel estimation process incurs additional cost in terms of signal probes. However, a fixed upper bound on transition coefficient magnitudes was derived and facilitates placing a constraint on the extra transition coefficients. Such a constraint is equivalent to additional a priori information that balances the additional unknown transition coefficients and substitutes for the need of having to use additional signal probes.

The key contributions of this chapter resulted in the following publications:

[1] K. Said and A. A. Beex, "Per-symbol ICI mitigation for frequency non-selective time-varying channels," in *2015 IEEE International Symposium on Signal Processing and Information Technology (ISSPIT)*, 2015, pp. 449-453.

[2] K. Said and A. A. Beex, "Per-symbol ICI mitigation for low-dimensional doubly dispersive channels using pilot restoration," in *2015 IEEE International Symposium on Signal Processing and Information Technology (ISSPIT)*, 2015, pp. 460-465.

Switching from channel estimation to the signaling context, finite length signaling blocks are prone to the leakage effect which manifests as ISI between data symbols in a block.

Unlike in the channel estimation case where the cisoidal frequencies of the delay and Doppler components can take any arbitrary real value, the signaling components, subcarriers in OFDM, are restricted by design to a grid of frequencies that are integer multiples of the block length reciprocal. This grid alignment of signaling components causes the leakage effect to be inconsequential. However, due to the channel dispersion effects the signaling components are no longer aligned to the grid and the leakage results in ISI between the data symbols.

Chapter 4 contains a detailed look at the various mathematical frameworks that can be used to construct signals with properties that are pertinent to communications. State-of-the-art frameworks such as Gabor systems and Staggered Lattices are analyzed and the limitations of each discussed. The Orthonormal Basis (ONB) signaling framework is proposed, with one example being the DPS ONB and its desirable properties for communications signaling are detailed.

Multicarrier communication signals can be described by the family of mathematical functions known as Gabor systems; the latter consist of time-frequency shifted versions of a prototype pulse shape. The ISI effect that arises in finite length signal blocks can be reduced by increasing the rate of decay of the leakage which is controlled by the pulse shape. Nyquist pulse shapes can lead to rapid decay rates and almost perfect confinement in frequency, however, the resulting Gabor system will no longer be complete. This is

explained by the so called Balian-Low theorem which states that a dichotomy exists between rapid decay in both time and frequency (leading to good confinement in both domains) and completeness, the latter being required to attain maximum bandwidth efficiency.

Staggered lattice signaling is a framework that is based on time-frequency shifts of a prototype pulse shape but uses a different definition for orthogonality than that of Gabor systems, thus releasing it from the clutches of the Balian-Low dichotomy. By restricting the prototype pulse shape to even functions, a set of pulse shapes exists which can lead to maximum bandwidth efficiency when symbols are placed according to an arrangement of two staggered grids. Each grid consists of either exclusively real symbols or exclusively imaginary symbols. The set of admissible pulse shapes is subject to a constraint that can be turned into an algebraic equation in the Zak transform domain.

For signaling frameworks based on a prototype pulse shape, which include Gabor Systems and Staggered Lattices, simultaneous time and frequency confinement can only be attained using pulse shapes that extend over the duration of multiple blocks. This results in a frame length that is extended by the tail of the pulse of the final block. For frames consisting of a small number of blocks, the frame length extension is a considerable fraction of the block duration. As a result, the effective data throughput is reduced.

A signaling set must satisfy the following three requirements: 1) separability/orthogonality, 2) good time-frequency confinement, and 3) maximum bandwidth efficiency. Any ONB readily satisfies properties 1 & 3. However, for non-Gabor ONBs property 2 must be generalized from the time-frequency domains to the signaling correlation domain. Thus, ONBs that are suitable for signaling must satisfy good confinement in the signal correlation domain.

The DPS ONB was shown to exhibit the property of quasi-orthogonality with respect to non-frequency-selective time-dispersive channels and a weaker version of the same property is inherited in doubly dispersive channels. In matrix form, the equivalent channel matrix exhibits rapid out-of-band decay and good confinement. Thus, unlike pulse

prototype based signaling, DPS ONBs are strictly limited to the duration of a symbol and exhibit rapid decay.

For a given set of channel parameters, an optimization problem can be formulated to solve for a signaling ONB that satisfies optimal confinement. The optimization is based on the joint approximate bandwidth reduction of the matrix components of the BEM representation of a channel for a given set of parameters.

The design of the main building blocks of a communication transceiver is determined by the choice of the signaling waveform.

In Chapter 5, the ramifications of using the DPS ONB for signaling on the different blocks of the receiver and transmitter are analyzed from the performance-complexity tradeoff viewpoint.

From the transmitter viewpoint, modulation using Gabor basis signaling has the lowest complexity due to its amenability to FFT processing. When non-rectangular pulse shapes are used, efficient implementation is made possible using polyphase filterbank implementations. For DPS ONB signaling, modulation has the complexity of matrix vector products. This complexity can be reduced if a common structure exists between the different components of the DPS basis.

The PAPR of the modulated signal is another metric of importance that is determined by the signaling waveform. PAPR for Gabor basis signaling, including OFDM, reach a max level equal to N when all signaling components are in phase. DPS ONB results in a much smaller PAPR.

The input-output relationship from the receiver perspective is represented by the equivalent channel matrix which incorporates the signaling waveform in addition to the channel. The structure of the equivalent channel matrix consists of a main diagonal band and decaying out-of-band components, with a rate of decay determined by the signaling waveform used. The rate of decay is of significant importance to two main receiver functions: 1) channel estimation and 2) equalization.

In the context of pilot-aided channel estimation, where pilots are embedded amidst data symbols in a block, a high out-of-band decay rate in the equivalent channel matrix implies less ISI spread and thus higher isolation of pilots to contamination from adjacent data symbols. In Doubly Dispersive (DD) channels, when DPS signaling is used, the equivalent channel matrix exhibits a structure that consists of a diagonal band with tapered width and out-of-band decaying elements. The decay rate of the out-of-band elements is higher compared to time-limited Gabor signaling waveforms. Exploiting this property, a pilot scheme with high data-to-pilot isolation can be devised by placing pilots at locations where the main diagonal band has the least width, i.e. the narrow edge of the taper. This facilitates the usage of fewer guard symbols around pilots for attaining the same level of performance as a less efficient pilot scheme using other waveforms. As a result, the same level of performance is obtained using fewer pilot resources and thus resulting in higher throughput efficiency.

Another function on the receiver side that is critical to achieving acceptable performance in DD channels is the equalization block. The complexity of the equalizer is determined by the computational burden of the matrix inversion step which is determined by the degree of sparsity in the matrix. Banded approximations can be applied to the equivalent channel matrix for the different signaling waveforms with the accuracy of the approximation depending on the out-of-band decay rate. Using the inverse of the equivalent channel matrix banded approximation, results in an SER performance for DPS signaling that is orders of magnitude higher compared to other Gabor signaling waveforms. This performance improvement is obtained for banded approximations using widths orders of magnitude smaller than the matrix size.

The key contributions of this chapter resulted in the following submissions to IEEE letters:

1) High Data-to-Pilot Isolation using Discrete Prolate Spheroidal Basis Signaling

2) Improved Tradeoff of Performance and Equalization Complexity in Doubly Dispersive Channels using DPSS Signaling

The time variation in the channel being a result of mobility suggests that it can be controlled by altering the effective direction of mobility of the antenna element. Using a rotating antenna configuration, the effective velocity vector can be steered without having to change the direction of motion of the platform. The subspace of possible channel realizations is a result of the sum of complex exponentials with cosines of a set of angles relative to a reference.

In Chapter 6, a new diversity method is investigated that is based on the rotating antenna configuration. Preliminary results are provided that show improvement. However this work is still in progress and is an open venue for future work.

Chapter 7 provides the general conclusions from the major building blocks completed in this dissertation and proposes directions for future work.

CHAPTER 2 TIME FREQUENCY VIEW OF COMMUNICATIONS

A communication signal is commonly represented as a function over the time-frequency space. However, this representation is paradoxical since changes in the signal along the time axis are not independent from the signal's frequency, therefore time and frequency cannot be treated simultaneously as independent variables. In a strict mathematical sense, the time-frequency independent treatment is valid for functions that belong to an admissible set.

A sufficient admissibility condition can be defined in terms of a conceptual 2-D grid on the time-frequency plane. A signal is allowed to exist at a certain frequency on the grid and vary in time independently, i.e. its frequency is considered unchanged, as long as the time variation over a grid step along the time axis is negligible. OFDM is an example that satisfies the admissibility condition where the block period (OFDM symbol period) corresponds to the grid step along the time axis and its reciprocal is the step along the frequency axis. Frequency subcarriers exist at discrete locations $f = n/T$ in the direction of the frequency axis and have a constant envelope for the whole period of the grid step along the time axis as shown in Fig. 1.

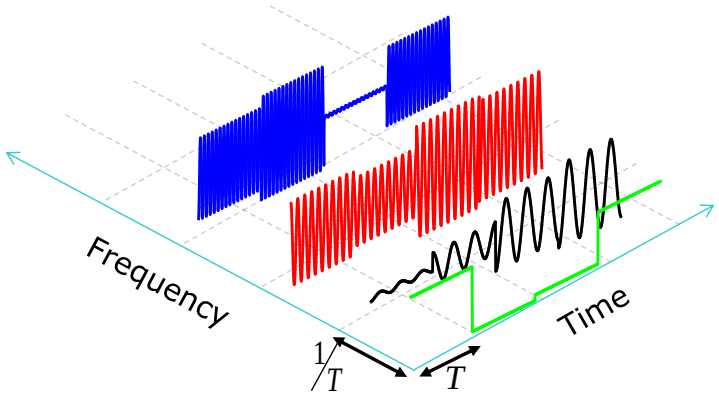

Figure 1: 2D Time-Frequency Signal Synthesis Grid

2.1 Time-Frequency Interrelatedness

The first quantitative description of the interdependence of time and frequency was given by Gabor in his foundational work [3] by the following fundamental bound on the time and frequency spread of a pulse shape $g(t)$:

$$T_{rms} BW_{rms} \leq \frac{1}{2} \tag{0.1}$$

where T_{rms} and BW_{rms} are the root-mean-square (rms) spread in time and frequency respectively, which are defined as:

$$T_{rms} = \sqrt{\int_{-\infty}^{\infty} t^2 \left| g(t) \right|^2 dt} \tag{0.2}$$

$$BW_{rms} = \sqrt{\int_{-\infty}^{\infty} f^2 \left| G(f) \right|^2 df} \tag{0.3}$$

where $G(f) = \int_{-\infty}^{\infty} f(t) e^{-j2\pi ft} dt$

A graphical illustration of this constraint is given in Fig. 2, where pulse shapes are depicted by rectangles of area $T_{rms} BW_{rms}$. The rectangles can have different aspect ratios but the area cannot go below 0.5, which is attained by the Gaussian pulse shape.

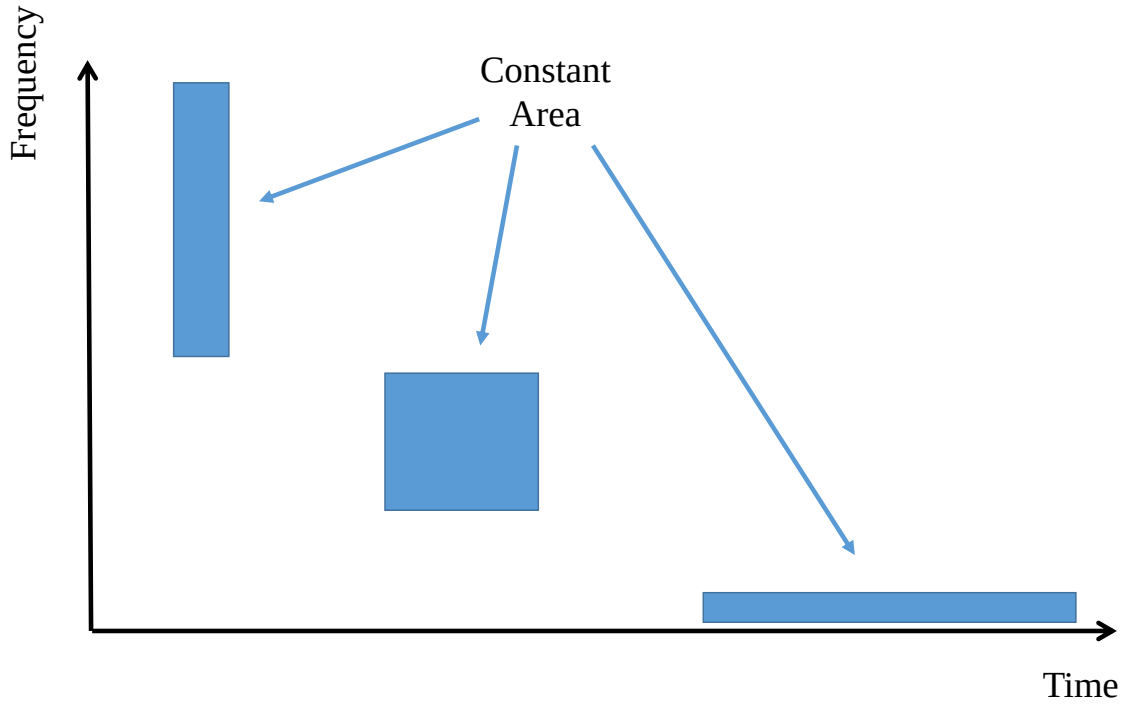

Figure 2: Time-Frequency Product Constraint

According to practical experience, signaling pulses are localized and can be treated as having definite strict limits in time and frequency. Thus, tessellating tile locations across the time-frequency plane represent orthogonal signals. However, in a strictly mathematical sense a pulse shape cannot be strictly time-limited and band-limited simultaneously. A strict limit in one domain will lead to infinite extent in the other.

To avoid a mathematical contradiction and to satisfy the intuition of thinking in terms of localized partitions in time and frequency, the description ***essentially limited*** was proposed in [4]. The property refers to a pulse having most of its energy (95% say) contained within finite extents of time, T_e, and frequency, BW_e, such that for practical purposes that pulse can be considered as being essentially localized. The pulse shapes used in practice are all essentially limited.

A typical energy concentration measure in the time and frequency domains is given by the following equations respectively:

$$\alpha = \frac{\int_{\frac{-T_e}{2}}^{\frac{T_e}{2}} |g(t)|^2 \, dt}{\int_{-\infty}^{\infty} |g(t)|^2 \, dt} \tag{0.4}$$

$$\beta = \frac{\int_{\frac{-BW_e}{2}}^{\frac{BW_e}{2}} |G(f)|^2 \, df}{\int_{-\infty}^{\infty} |G(f)|^2 \, df} \tag{0.5}$$

A signal is considered essentially limited in time (frequency) when α (β) is close to 1.

2.2 Filterbank Framework for Multicarrier Signals

A complete and general representation of signaling involves both time and frequency which is represented by a phase-space lattice, as illustrated in Fig. 3.

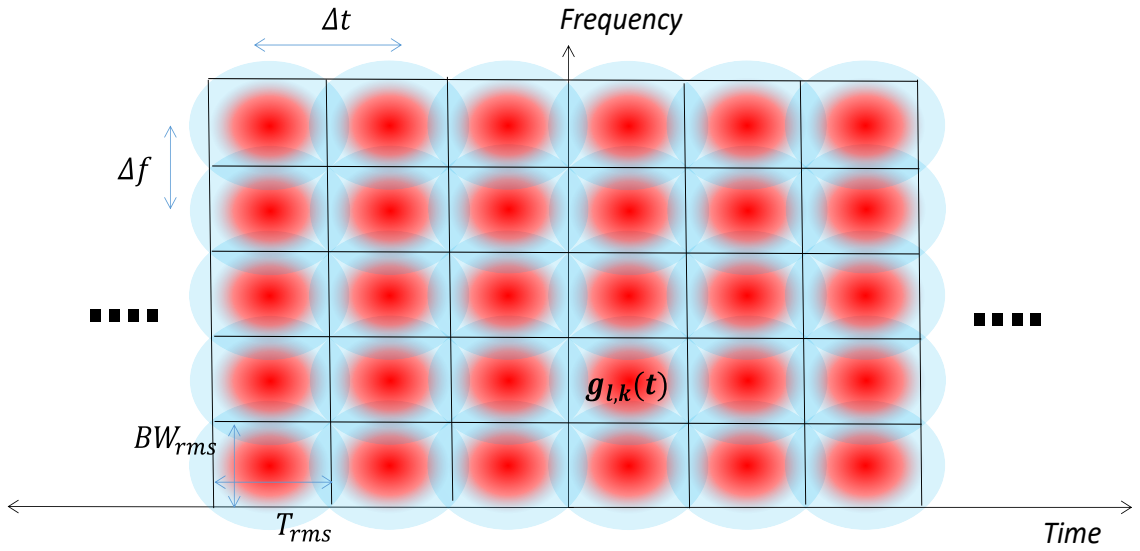

Figure 3: Phase Space Lattice

Figure 3 shows a 2-D lattice of signaling blocks, each containing $g_{l,k}(t)$, $l \in \mathbb{Z}$, $\{0,...,K-1\}$ which correspond to a set of signaling pulse shapes that are time-frequency shifted versions of an atomic pulse shape $g(t)$:

$$g_{l,k}(t) = g(t - l\Delta t)e^{j2\pi k\Delta f(t-l\Delta t)} \tag{0.6}$$

where Δf and Δt are spacings in frequency and time (symbol rate) respectively. The frequency index k runs up to a finite limit $K-1$ to represent the typical situation of a signaling scheme operating within a certain bandwidth and ongoing for all time. It should be noted that in the general case, the extent of a pulse in time (frequency), T_{rms} (BW_{rms}) and the pulse placement spacing in time (frequency), Δt (Δf), are distinct parameters that are not necessarily equal. For example, the time extent of a pulse, T_{rms}, can exceed the signaling duration, Δt, to overlap with adjacent neighbors.

The transmitted signal is given by:

$$s(t) = \sum_{l=-\infty}^{\infty}\sum_{k=0}^{K-1} a_k(l)\, g_{l,k}(t) \tag{0.7}$$

As illustrated in Fig. 3, the signaling blocks have fuzzy edges that can overlap (with more than one adjacent neighbor) to emphasize the fact that practical pulse shapes are neither strictly limited in time nor in frequency. Thus the blocks cannot tessellate as one would ideally desire.

According to inequality (2.1), the area of a single block/atom out of all possible pulse shapes of finite energy, $g(t) \in L^2(\mathbb{R})$, cannot go below a certain value. Thus, there exists a maximum number of signaling blocks that can be packed within a certain time-frequency interval $[0,T]\times[-B/2, B/2]$. This number cannot be exceeded regardless of the pulse shape and is commonly known as the ***signal space dimension*** D, which with good approximation is equal to:

$$D = BT + 1 \tag{0.8}$$

It would seem that due to the inevitable time-frequency overlap of signaling elements interference-free separation is impossible at the receiver. However, the true requirement for separation is ***orthogonality***, which does not always translate to disjointness in frequency. The processing used to separate signals with this kind of orthogonality demands

the stringent constraint of ***time synchronization***. This point is central to the frequency packing efficiency property of OFDM.

The general transmitter/receiver architecture corresponding to the signaling structure in Fig. 3 in its discrete time realization takes the form of a ***transmultiplexer***, which consists of a synthesis filter bank followed by an analysis filter bank (see Fig. 4). This is in contrast to the sub-band coding configuration [6]. The transmultiplexer representation allows the use of multi-rate filter bank theory to obtain insights into analyzing multicarrier systems as well as to provide a tool for efficient implementation.

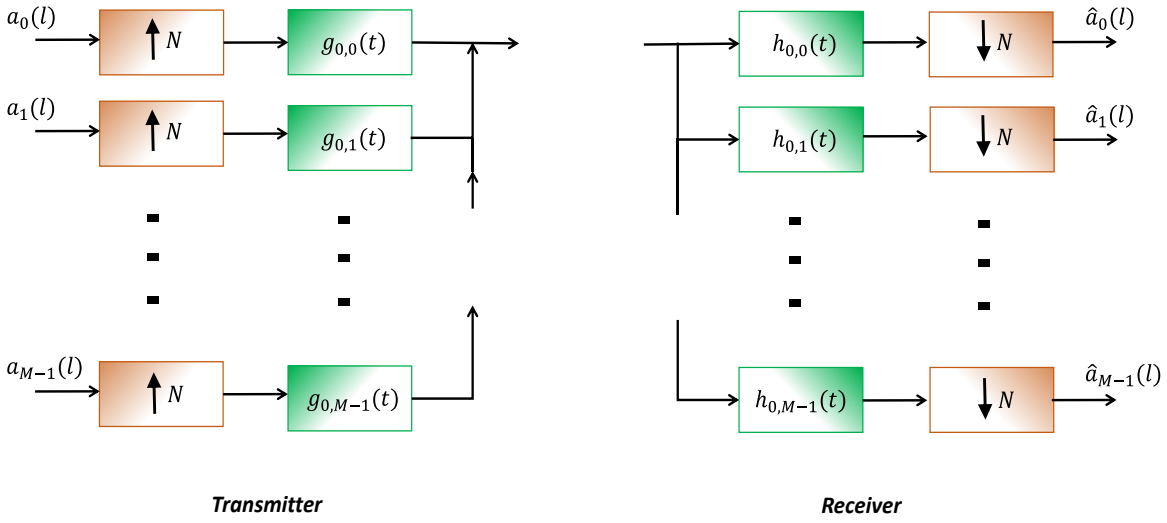

Figure 4: Trans-multiplexer Configuration for Multicarrier Signaling

On the transmit side, the input data streams are upsampled and then pulse shaped with FIR filters effectively replacing the data symbol with a pulse shape function weighted by that symbol. The impulse response of the k-th filter is a sampled version of the transmit pulse shape $g_{0,k}(t)$. Similarly, at the receiver side the filter pulse shape $h_{0,j}(t)$ is convolved with an input data stream of pulses, effectively performing an inner product which for a single input pulse is given by:

$$\int_{t-T'}^{t} g_{0,k}(\tau)\, h_{0,j}(t-\tau)\, d\tau = \int_{t-T'}^{t} g_{0,k}(\tau)\, h_{0,j}\left(-(\tau-t)\right) d\tau \qquad (0.9)$$

Downsampling (sampling with rate $\frac{1}{\Delta t}$ at the symbol rate) at the receiver side with a delay T' equal to the receiver and transmitter pulse durations as a requirement for the receive filter bank to be causal, and making the substitution $h_{0,j}(-t) = \tilde{h}_{0,j}(t)$:

$$\begin{aligned} y_0(t)\big|_{t=nT+T'} &= \int_{nT}^{nT+T'} g_{0,k}(\tau)\tilde{h}_{0,j}(\tau - nT - T')d\tau \\ &= \int_{nT}^{nT+T'} g_{0,k}(\tau)\tilde{h}_{n,j}(\tau - T')d\tau \\ &= \left\langle g_{0,k}(\nu)\tilde{h}_{n,j}(\nu - T') \right\rangle \end{aligned} \tag{0.10}$$

Choosing the set of functions $h_{l,k}(t),\ l \in \mathbb{Z},\ k \in \{0,...,K-1\}$ to satisfy orthogonality:

$$\left\langle g_{0,k}(\nu)\tilde{h}_{n,j}(\nu - T') \right\rangle = \delta_{n,j-k} \tag{0.11}$$

guarantees zero interference in time Inter-Symbol Interference (ISI), and frequency, Inter-Carrier Interference (ICI).

Therefore, the output for the full signal $s(t)$ given in (2.7) is going to be:

$$\begin{aligned} y_j(t)\big|_{t=nT+T'} &= \sum_{l=-\infty}^{\infty}\sum_{k=0}^{K-1} a_k(l)\left\langle g_{l,k}(\nu), \tilde{h}_{n,j}(\nu - T') \right\rangle \\ &= a_k(l)\delta_{n-l,j-k} \\ &= a_j(n) \end{aligned} \tag{0.12}$$

The channel effect was not considered here; that will be the subject of Chapter 3.

1.2.1 OFDM Signaling Structure

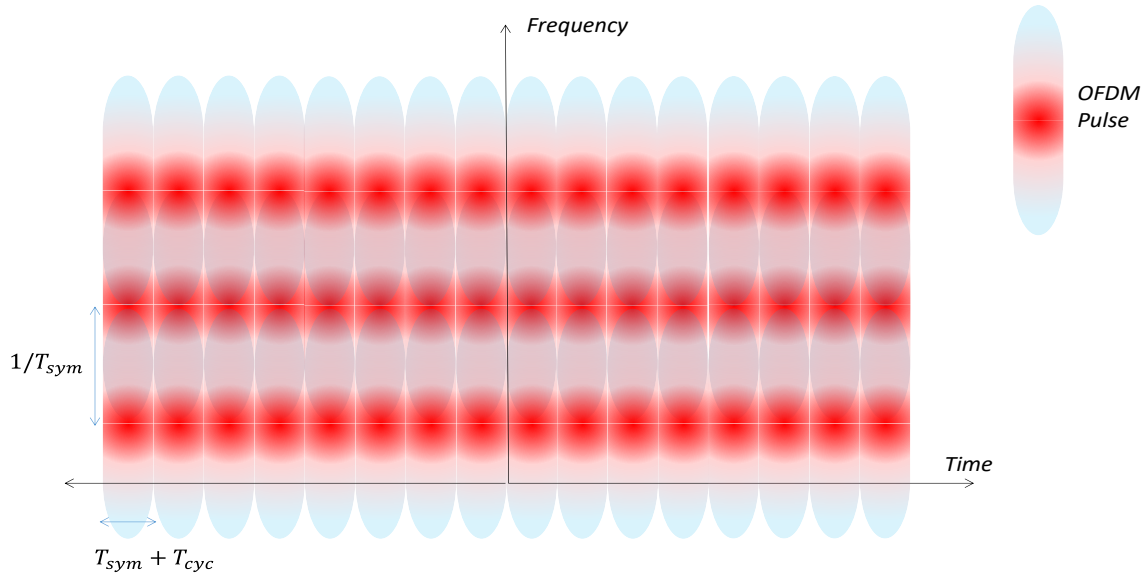

Figure 5: OFDM Phase Space Lattice

Classical OFDM uses strictly time limited rectangular pulses in time where the transmit and receive pulse sets are given by:

$$g_{l,k}(t) = \chi_{\left[-T_{cyc},T_{sym}\right]}\left(t - l(T_{sym} + T_{cyc})\right)e^{\frac{j2\pi k}{T_{sym}}\left(t - l(T_{sym}+T_{cyc})\right)} \tag{0.13}$$

$$h_{l,k}(t) = \chi_{\left[0,T_{sym}\right]}\left(t - l(T_{sym} + T_{cyc})\right)e^{\frac{-j2\pi k}{T_{sym}}\left(t - l(T_{sym}+T_{cyc})\right)} \tag{0.14}$$

where $\chi_{[0,T]}$ is the indicator function over the interval $[0,T]$, T_{cyc} is the cyclic prefix duration and T_{sym} is the effective symbol duration.

In discrete time:

$$g_{l,k}[n] = \chi_{[-C,M]}(n - lN)W_M^{k(n-lN)} \tag{0.15}$$

$$h_{l,k}[n] = \chi_{[0,M]}(n - lN)W_M^{-k(n-lN)} \tag{0.16}$$

where $N = \frac{T_{sym} + T_{cyc}}{T_s}$, $M = \frac{T_{sym}}{T_s}$, $W_M^{k(n-lN)} = e^{\frac{j2\pi k}{M}(n-lN)}$, $C = \frac{T_{cyc}}{T_s}$.

The time extent of the transmit rectangular pulse differs from that of the receive pulse in that the first is on for the entire symbol duration $\left[-T_{cyc}, T_{sym}\right]$ while the latter is on only for the interval $\left[0, T_{sym}\right]$. Due to the cyclic prefix in the transmit signal, adjacent sinc functions in the frequency spectrum are ***not*** aligned at the zero crossings, contrary to common marketing illustrations of OFDM spectrum. This however has no bearing on the interference-free separation of the subcarriers at the receiver. However, this nuance is responsible for high mutual interference between adjacent subcarriers that are not synchronized in time.

The corresponding filter bank representation is given in Fig. 6.

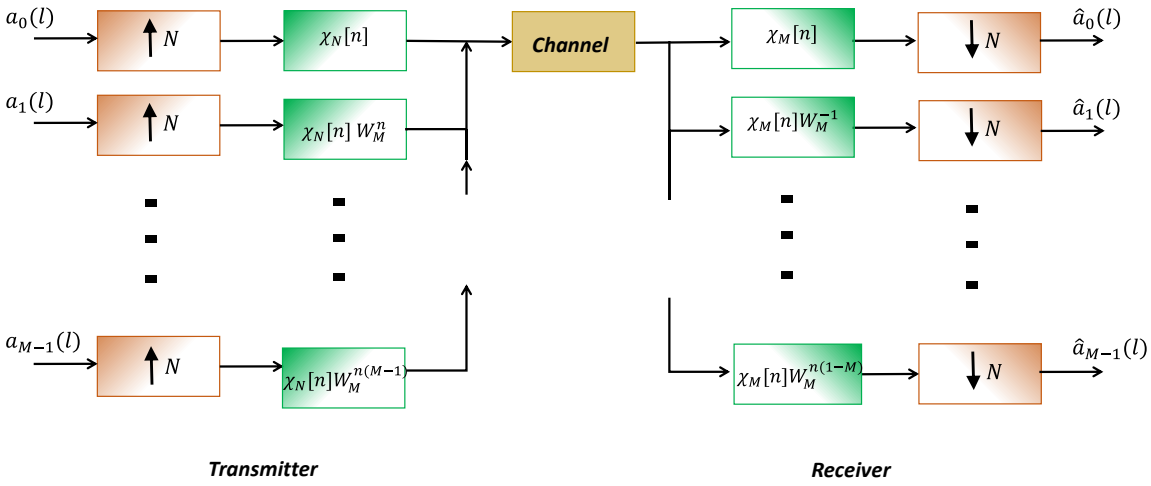

Figure 6: OFDM Trans-multiplexer Configuration

Using the polyphase decomposition on both the transmit and receive filter banks gives the well-known IDFT/DFT based architecture:

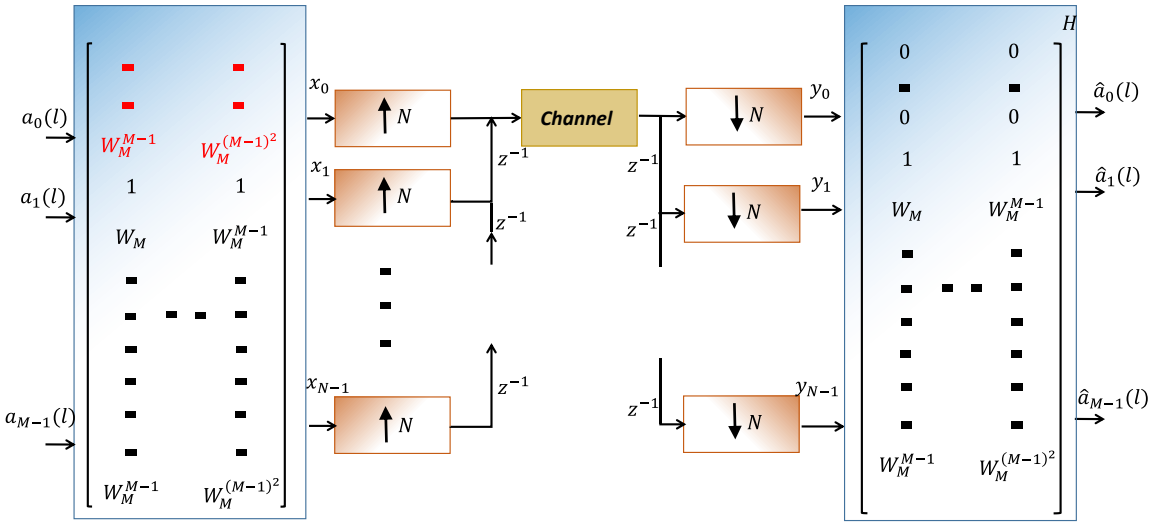

Figure 7: OFDM Cyclic Prefix Extended IDFT/DFT Configuration

The transmit IDFT on the transmitter side is extended to become a rectangular matrix, as indicated by the red elements, to account for the $N-M$ cyclic prefix samples in the output signal. The receive DFT is prefixed with zeros to account for the cyclic prefix removal in the receiver. The transmit side commutator (bank of upsamplers + delay line) acts as a parallel to serial converter while the receive side commutator (delay line + bank of downsamplers) does the opposite function.

The combination of the transmit commutator, the channel and the receive commutator can be represented by a doubly-infinite matrix [7], [8] acting on the sequence $...,x_{-1},x_0,x_1,...$ and generating the output sequence $...,y_{-1},y_0,y_1,...$.

Considering only the finite output sequence segment $...,y_{-1},y_0,y_1,...$ the channel matrix will have the following structure:

$$\mathbf{C} = \begin{bmatrix} c_{0,L-1} & \cdot & \cdot & c_{0,L-1} & & & & & & & \\ & \cdot & \cdot & \cdot & \cdot & & & & & & \\ & & \cdot & \cdot & \cdot & \cdot & & & & & \\ & & & c_{L-1,L-1} & \cdot & \cdot & c_{L-1,0} & & & & \\ & & & & \cdot & \cdot & \cdot & \cdot & & & \\ & & & & & c_{N-M,L-1} & \cdot & \cdot & c_{N-M,0} & & \\ & & & & & & \cdot & \cdot & \cdot & \cdot & \\ & & & & & & & \cdot & \cdot & \cdot & \cdot \\ & & & & & & & & c_{N-1,L-1} & & c_{N-1,0} \end{bmatrix}$$

The elements c_{ij} of the matrix $\mathbf{C}$ represent the gain/attenuation of j^{th} tap delay at the i^{th} time instant. L is the max tap delay of the channel, which determines the cyclic prefix having length $N-M \geq L$. When time variation is negligible over a symbol period the channel matrix becomes Toeplitz. The input-output relationship is given by:

$$\mathbf{y} = \mathbf{C}\mathbf{x} \tag{0.17}$$

where $\mathbf{y} = \left[y_0, ..., y_{N-1}\right]^T$ and $\mathbf{x} = \left[x_0, \ldots, x_{N-1}\right]^T$.

The DFT matrices at the receiver and transmitter can be given as:

$$\mathbf{F}_{TX} = \begin{bmatrix} \mathbf{0}_{(N-M)\times(2M-N)} \mid \mathbf{I}_{N-M} \\ \mathbf{I}_M \end{bmatrix} \mathbf{F} \tag{0.18}$$

$$\mathbf{F}_{RX} = \begin{bmatrix} \mathbf{0}_{(N-M)\times M} \\ \mathbf{F} \end{bmatrix}^H \tag{0.19}$$

where $\left[\mathbf{F}\right]_{lk} = e^{j2\pi lk/M}$.

The input-output relationship describing Fig. 7 is given by:

$$\begin{aligned} \hat{\mathbf{a}} &= \mathbf{F}_{RX}\mathbf{C}\mathbf{F}_{TX} \\ &= \mathbf{F}^H \begin{bmatrix} \mathbf{0}_{(N-M)\times M} \\ \mathbf{I}_M \end{bmatrix} \mathbf{C} \begin{bmatrix} \mathbf{0}_{(N-M)\times 2M-N} \mid \mathbf{I}_{N-M} \\ \mathbf{I}_M \end{bmatrix} \mathbf{F}\mathbf{a} \\ &= \mathbf{F}^H \tilde{\mathbf{C}} \mathbf{F}\mathbf{a} \end{aligned} \tag{0.20}$$

where $\mathbf{a}$ and $\hat{\mathbf{a}}$ are vectors of input symbols and recovered symbols at the receiver respectively.

In (2.20), the matrix to the left of $\mathbf{C}$ removes the top $N-M$ rows while the matrix $\mathbf{F}_{TX}$ on the right of $\mathbf{C}$, adds the leftmost $N-M$ columns to the right-most $N-M$ ones resulting in a square matrix having the following structure:

$$\tilde{\mathbf{C}} = \begin{bmatrix} c_{N-M,0} & & & & & c_{N-M,L-1} & \cdot & \cdot \\ \cdot & \cdot & & & & & \cdot & \cdot \\ \cdot & \cdot & & & & & & \cdot \\ \cdot & \cdot & \cdot & \cdot & & & & \\ c_{N-M+L-1,L-1} & \cdot & \cdot & \cdot & c_{N+M+L-1,0} & & & \\ & \cdot & \cdot & \cdot & \cdot & \cdot & & \\ & & c_{N-1,L-1} & \cdot & \cdot & \cdot & c_{N-1,0} & \end{bmatrix}$$

2.3 Time-varying Channel Description

It can be argued that the problem of communications in essence concerns finding the right ways to deal with the channel and its effects, be it physical or artificial, to pass messages through in the most efficient way. Hence, the channel plays a central role in the design and analysis of message processing devices, i.e. transmitter and receiver.

From the transmitter perspective, the channel dictates the signal waveforms that must be used in order to maximize the communications capacity metrics, such as throughput, with the most efficient usage of resources, such as bandwidth and power. The transmitter can play a role in the compensation of the channel effects by adapting the signals to the channel based on ***channel state information*** (CSI) feedback from the receiver. However, in TV channels which experience significant change over the time required for CSI feedback to arrive at the transmitter, transmitter feedback techniques become useless.

From the receiver perspective, the undesirable channel effects inflicted on the message carrying signal must be undone by the receiver in order to be able to recognize the transmitted symbols and extract the constituent information. This process is generally

referred to as ***equalization***. To perform this function, the receiver must have a sufficiently accurate representation of the pertinent channel effects known as the channel model. Receiver based channel equalization techniques will discussed in Chapter 3.

In its most general form, the wireless channel can be described as a time-varying non-linear system. Aside from the artificial components in the communication system, such as power amplifiers, the channel medium is not known to cause amplitude-dependent effects on the wave-carrying signal except for applications where the signal power level is excessively high. Thus, the channel description takes the form of a linear time-varying system/filter (LTV).

A general input-output relationship for an LTV system is given by:

$$\begin{aligned} y(t) &= \int_{-\infty}^{\infty} x(t-\tau)\, h(t,\tau)\, d\tau \qquad \text{(Direct-Form I)} \\ &= \int_{-\infty}^{\infty} x(t-\tau)\, g(t-\tau,\tau)\, d\tau \quad \text{(Direct-Form II)} \end{aligned} \tag{0.21}$$

where $x(t)$ is the input, $y(t)$ is the output and $h(t,\tau)$ is referred to as the time-varying impulse response or the delay spreading function.

A representation which reflects the physical mechanism behind the channel behavior is that of a tapped-delay line filter having a continuum of taps with time varying coefficients as illustrated in Fig. 8. The continuum of weighted taps captures all possibilities of propagation path scenarios, either diffuse or specular (delta function weights) of any number.

Due to the mobility of the objects that constitute the channel: transmitter, receiver, or any of the objects in the environment that interact with the signal, two mechanisms come into play typically acting on different time scales. First, the geometry of the propagation paths changes with time causing the gains/attenuations along each path to change over a coarse time scale. Second, on a finer time scale the geometry of the propagation paths can be considered constant yet due to the Doppler spread time variation is still present in the channel.

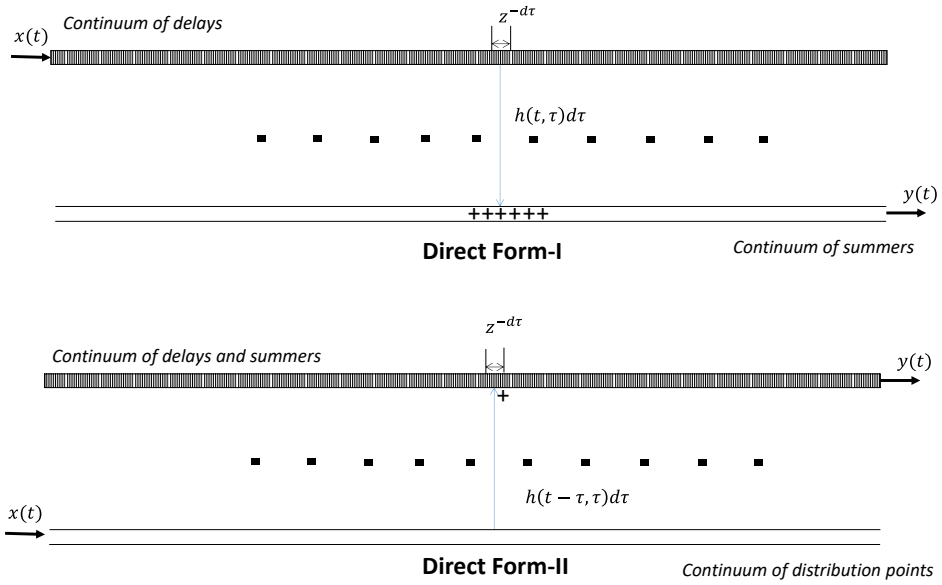

Figure 8: Time-varying Tapped Delay Line Model

A subtle point worth noting is that the Direct Form-II is in better agreement with physical reality. This is due to the fact that the time-varying coefficients for the different delays are predetermined simultaneously at the instant an input sample is launched into the channel since from that instant the propagation paths are decided. Another note, unlike in the case of a time-invariant FIR filter, the Direct Form-II is not the transpose structure of the Direct form-I configuration, i.e. the matrix-operator of the first is not the transpose of the latter.

The channel input-output relationship can take four possible forms depending on the possible representation domains of the input and the output signals, either time or frequency. As will be shown, each representation is suited for a particular signaling scheme and expression of the relevant channel characteristics.

1- <u>Time-Delay Domain</u>

In this form, the input and output are related in terms of the Time-Variant Impulse Response, $h_{t,\tau}(t,\tau)$, where the subscripts t and τ denote the domain of the first and second variables respectively:

$$y(t) = \int_{-\infty}^{\infty} x(\tau) h_{t,\tau}(t, t-\tau)\, d\tau \tag{0.22}$$

Substituting using $\tilde{h}_{t,\tau}(t,\tau) = h_{t,\tau}(t, t-\tau)$ in (2.22) gives the standard linear integral operator form:

$$y(t) = \int_{-\infty}^{\infty} \tilde{h}_{t,\tau}(t,\tau)\, x(\tau)\, d\tau \tag{0.23}$$

thus the generality of this representation for any LTV system.

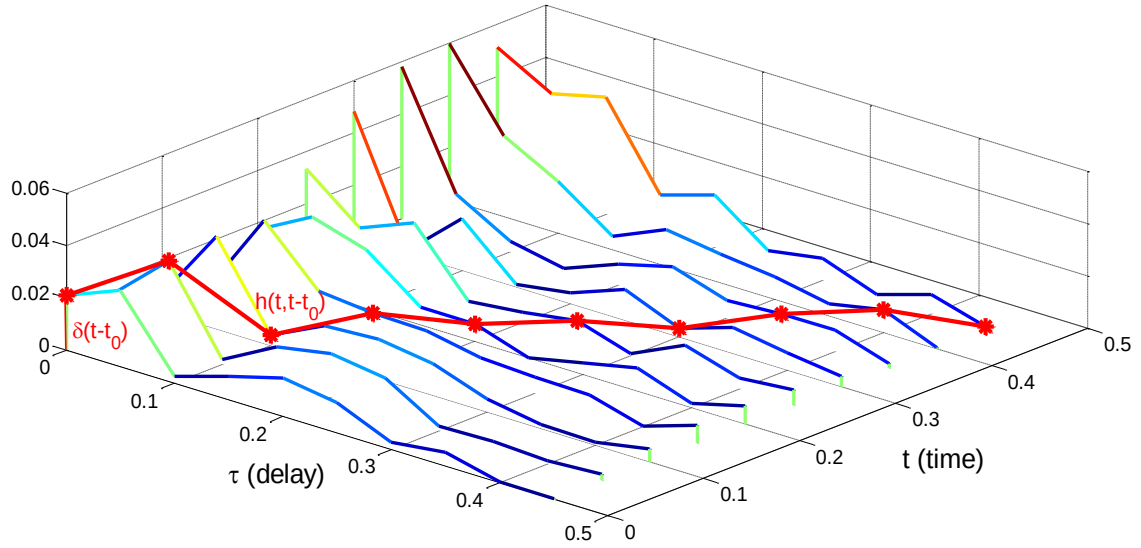

Figure 9: TV Impulse Response $h_{t,\tau}(t,\tau)$

A typical TV impulse response function is shown in Fig. 9. An important point worth nothing is that, unlike in the TI case, the response to an impulse excitation at time t_0 is not a slice function along the τ-axis, $h_{t,\tau}(t_0,\tau)$, but instead is the diagonal slice $h_{t,\tau}(t_0, t-t_0)$.

2- <u>Delay-Doppler Domain</u>

Taking the Fourier transform of $h_{t,\tau}(t,\tau)$ over the time variable t gives the **Spreading Function:**

$$h_{d,\tau}(\nu,\tau) = \int_{\infty}^{\infty} h(t,\tau)\, e^{-j2\pi\nu t}\, dt \tag{0.24}$$

Correspondingly, the input-output relationship is given by:

$$y(t) = \int_{-\infty}^{\infty}\int_{-\infty}^{\infty} h_{d,\tau}(\nu,\tau)\, x(t-\tau)\, e^{j2\pi\nu t}\, d\tau\, d\nu \tag{0.25}$$

Based on the interpretation of (2.25), the spreading function quantifies the spread of the input to different time delays and different frequency shifts in the output.

Due to the underlying physics governing the channel behavior, the max Doppler spread has to be strictly limited and the delay spread is essentially limited, thus the function $h_{d,\tau}(\upsilon,\tau)$ becomes one of finite 2-D support. Out of the four representations, the delay-doppler form is the only phenomenologically accurate model that reflects the effect of a continuum of scatterers causing delay and Doppler. The remaining models are instrumental in nature [9].

The magnitude of a typical spreading function is given in Fig. 10.

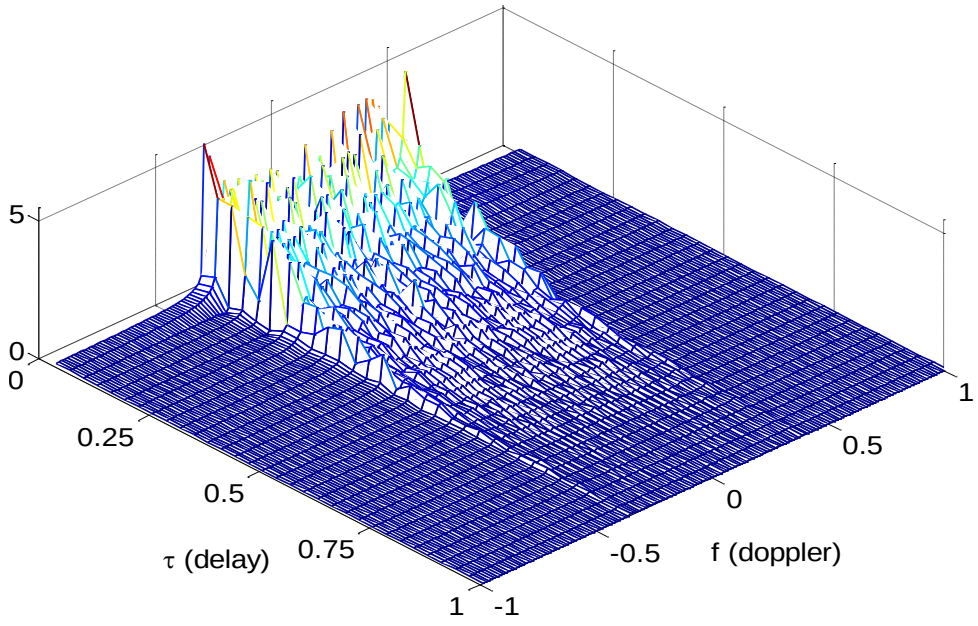

Figure 10: Spreading Function $h_{d,\tau}(\upsilon,\tau)$

3- <u>Time-Frequency Domain</u>

Taking the Fourier transform of $h_{t,\tau}(t,\tau)$ over the delay variable τ gives the **Time-Varying Transfer Function.**

$$h_{t,f}(t,f) = \int_{-\infty}^{\infty} h(t,\tau) e^{-j2\pi f\tau} d\tau \tag{0.26}$$

The input-output relationship where the input is represented in terms of its frequency spectrum, $X(f) = \int_{\infty}^{\infty} x(t) e^{-j2\pi ft} dt$, is given by:

$$y(t) = \int_{-\infty}^{\infty} h_{t,f}(t,f) X(f) e^{j2\pi ft} df \tag{0.27}$$

This form has close resemblance to the transfer function in the TI case where it describes the "transference" of cisoidal (complex sinusoidal) signals from input to output only altered by a constant weighting factor. The latter is a direct consequence of cisoids being eigenfunctions for TI channels, which is not true for TV channels. This can be shown by taking the Fourier transform of (2.27):

$$\begin{aligned} Y(f) &= \int_{-\infty}^{\infty} y(t) e^{-j2\pi ft} dt \\ &= \int_{-\infty}^{\infty}\int_{-\infty}^{\infty} h_{t,f}(t,f) X(f) e^{j2\pi ft} df \; e^{-j2\pi ft} dt \\ &= \int_{-\infty}^{\infty} X(f) \int_{-\infty}^{\infty} h_{t,f}(t,f) e^{j2\pi(f-f')t} dt\, df \end{aligned} \tag{0.28}$$

The inner integral would have reduced to a delta function if it were not for the time dependence of $h_{t,f}(t,f)$. Over short intervals where the time-variation is negligible, the transference property is approximately satisfied. In such situations when the time variation over segmented periods of time corresponding to blocks of data (symbols or frames) is negligible, the channel is known to be ***quasi-static***. For OFDM signals, the single tap

equalizer can only be used in channels satisfying this quasi-static condition as will be discussed at the end of this Chapter.

4- Doppler-Frequency Domain

Up till the quasi-static case, time and frequency can be viewed as orthogonal dimensions/resources. Beyond this point, the two dimensions merge and thus the separation becomes meaningless. A unidimensional representation of the channel effect, in the frequency domain, is given by the **Frequency Coupling Function** which is obtained by taking the double Fourier transform of $h_{t,\tau}(t,\tau)$:

$$h_{d,f}(d,f) = \int_{-\infty}^{\infty}\int_{-\infty}^{\infty} h(t,\tau) e^{-j2\pi dt} e^{-j2\pi f\tau} dt d\tau \tag{0.29}$$

The frequency domain input-output relationship is given by:

$$\begin{aligned} Y(f') &= \int_{-\infty}^{\infty}\int_{-\infty}^{\infty} h_{t,f}(t,f) X(f) e^{j2\pi ft} df \; e^{-j2\pi ft} dt \\ &= \int_{-\infty}^{\infty} X(f) \int_{-\infty}^{\infty} h_{t,f}(t,f) e^{-j2\pi(f'-f)t} dt df \\ &= \int_{-\infty}^{\infty} X(f) h_{d,f}(f'-f,f) df \end{aligned} \tag{0.30}$$

Equation (2.30) expresses the mutual coupling between the input frequencies, which is not present in the quasi-static channel case.

The following table summarizes the utility of each input-output form from two perspectives: the underlying physical mechanism and the signal processing suitability for certain signals.

Table 1: Different forms of the time-varying channel representation and the utility of each

input-output form	**Physical Mechanism**	**Signal Processing**
Time-Delay	*Continuum of delays with time varying coefficients*	*Single-carrier*
Delay-Doppler	*Scatterers with time-varying delay*	N/A
Time-Frequency	*Filter with time varying transfer function*	*Multi-carrier (in quasi-static channels)*
Doppler-Frequency	*Continuum of weighted modulators*	*Multi-carrier*

2.4 Essential Dimensionality of Signal Pulse and Channel

Up till this point, the representation of channels and their operation on the input signal were given in terms of continuous functions and continuous operators respectively, in time (t), delay (τ), frequency (f), and Doppler (d) variables. For practical reasons, the continuous operations must be converted into discretized versions. This is more involved than simply discretizing the operator, such as sampling the variables in $h(t,\tau)$ and the operand $x(t)$.

Relying on the concepts of essential limitedness in both time and frequency, discretized channel representations are obtained [10],[11]. Thus, we consider a typical practical communication input pulse $x(t)$ that is both essentially time and band limited. A typical example would be a rectangular shaped OFDM pulse with virtual edge subcarriers (edge subcarriers turned off) so that most of the sinc spectrum, "the essence", is well contained within the nominal radian bandwidth B.

Starting from (2.22) and substituting for $x(t)$ in terms of its Fourier transform:

$$y(t)=\int_{-\infty}^{\infty}h_{t,\tau}(t,\tau)\left[\frac{1}{2\pi}\int_{\frac{-B}{2}}^{\frac{B}{2}}X(\omega)e^{j\omega(t-\tau)}d\omega\right]d\tau \tag{0.31}$$

Due to the limited support of $X(\omega)$ over $\left[\frac{-B}{2},\frac{B}{2}\right]$, we can expand $X(\omega)e^{j\omega t}$ in terms of a Fourier series as follows:

$$y(t)=\int_{-\infty}^{\infty}h_{t,\tau}(t,\tau)\left[\frac{1}{2\pi}\int_{\frac{-B}{2}}^{\frac{B}{2}}\left[\sum_{k=-\infty}^{\infty}\frac{1}{B}\int_{\frac{-B}{2}}^{\frac{B}{2}}X(\nu)e^{j\nu\left(t-\frac{2\pi k}{B}\right)}d\nu\, e^{\frac{j2\pi\omega k}{B}}\right]e^{-j\omega\tau}d\omega\right]d\tau \tag{0.32}$$

Reordering integrals and the sum:

$$\begin{aligned}y(t)&=\sum_{k=-\infty}^{\infty}\frac{1}{B}\int_{\frac{-B}{2}}^{\frac{B}{2}}\frac{1}{2\pi}\int_{\frac{-B}{2}}^{\frac{B}{2}}X(\nu)e^{j\nu\left(t-\frac{2\pi k}{B}\right)}d\nu\, e^{\frac{j2\pi\omega k}{B}}\int_{-\infty}^{\infty}h_{t,\tau}(t,\tau)e^{-j\omega\tau}d\tau d\omega\\&=\frac{1}{B}\sum_{k=-\infty}^{\infty}x\left(t-\frac{2\pi k}{B}\right)\int_{\frac{-B}{2}}^{\frac{B}{2}}e^{\frac{j2\pi\omega k}{B}}H_{t,\tau}(t,\omega)d\omega\\&=\frac{2\pi}{B}\sum_{k=-\infty}^{\infty}x\left(t-\frac{2\pi k}{B}\right)\bar{h}_{t,\tau}\left(t,\frac{2\pi k}{B}\right)\end{aligned} \tag{0.33}$$

where $H_{t,\tau}(t,\omega)$ is the Fourier transform of $h_{t,\tau}(t,\tau)$ over the variable τ and $\bar{h}_{t,\tau}$ is the projection of $h_{t,\tau}(t,\tau)$ as a function of τ onto the space of functions bandlimited to the interval $\left[\frac{-B}{2},\frac{B}{2}\right]$. The limited bandwidth of the input signal was imposed on the channel making it amenable to sampling, a property reminiscent of ***adjoint operators.***

Sampling the output in time at the Nyquist rate of the input signal $T_s = \frac{2\pi}{B}$, the discrete convolution form is obtained:

$$y(n) = \frac{2\pi}{B} \sum_{k=-\infty}^{\infty} x\big((n-k)T_s\big) \bar{h}_{t,\tau}\left(\frac{2\pi n}{B}, \frac{2\pi k}{B}\right) \tag{0.34}$$

In a dual fashion, the time-limitedness of the input leads to a discretized input-output relationship in the frequency domain:

$$Y(n) = \frac{2\pi}{T} \sum_{k=-\infty}^{\infty} X\left(\frac{n-k}{T}\right) \bar{h}_{d,f}\left(\frac{2\pi k}{T}, \frac{2\pi(n-k)}{T}\right) \tag{0.35}$$

where $\bar{h}_{d,f}$ is the projection of $h_{d,f}$ as a function of the variable f onto the space of functions bandlimited to the interval $[0, T]$.

In a similar fashion, the other two channel forms can be discretized, however, the forms in (2.34) and (2.35) are the most relevant in describing channel matrices for single carrier and multicarrier systems.

The physical laws governing the behavior of the channel dictate limits on the channel model parameters. Due to the wave propagation path-loss the signal paths with delays beyond a certain limit, $\tau_{\max}$, are highly attenuated and can be considered negligible. As for the Doppler spread, it is strictly limited to the max Doppler, $\upsilon_{\max}$, which is determined by the maximum velocity of objects moving in the channel environment.

Imposing the conditions of causality and the limit on the maximum path delay, $[0, N_\tau]$, (2.35) becomes (using sequence notation):

$$\begin{aligned} y[n] &= \sum_{k=0}^{N_\tau} \bar{h}_{t,\tau}[n,k]\, x[n-k] \\ &= \sum_{m=n-N_\tau}^{n} \bar{h}_{t,\tau}[n, n-m]\, x[m] \end{aligned} \tag{0.36}$$

where $\frac{2\pi N_\tau}{B} = \tau_{\max}$.

In a dual fashion, (2.36) (frequency domain case), imposing the limit on the Doppler frequency, $[-\upsilon_{\max}, \upsilon_{\max}]$ becomes:

$$\begin{aligned} Y[n] &= \sum_{k=-M_d}^{M_d} \bar{h}_{d,f}[k, n-k] X[n-k] \\ &= \sum_{m=n-M_d}^{n+M_d} \bar{h}_{d,f}[n-m, m] X[m] \end{aligned} \tag{0.37}$$

where $M_d = \upsilon_{\max} T$.

Defining the following transformed versions of the channel representations $\bar{h}_{t,\tau}$ and $\bar{h}_{d,f}$:

$$\tilde{h}_{t,\tau}[n, m] = \bar{h}_{t,\tau}[n, n-m] \tag{0.38}$$

$$\tilde{h}_{d,f}[n, m] = \bar{h}_{d,f}[n-m, m] \tag{0.39}$$

This facilitates writing (2.36) and (2.37) in a matrix-vector product form where columns(rows) of the 2-D matrix having elements $\bar{h}_{t,\tau}[n, m]\left(\bar{h}_{d,f}[n, m]\right)$ are placed along the diagonals of a matrix having elements $\tilde{h}_{t,\tau}[n, m]\left(\tilde{h}_{d,f}[n, m]\right)$. This is illustrated in Fig. 11 where the time domain channel matrix on the left is lower triangle and diagonally banded, while on the right is the frequency domain channel matrix which is also banded but with band centered around the main diagonal.

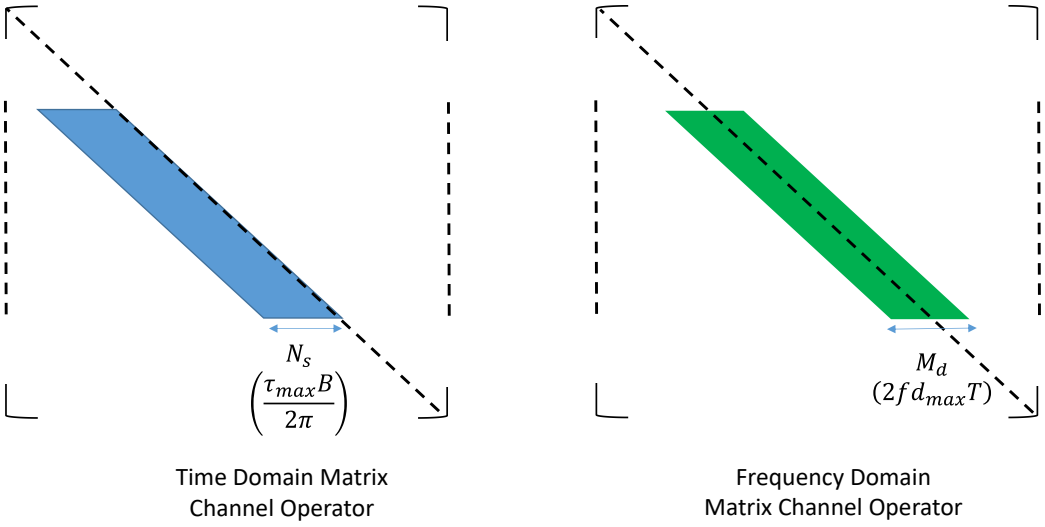

Figure 11: Time Domain (Left) and Frequency Domain (Right) Channel Matrix Operators

Time Domain matrix form, from (2.36):

$$y[n] = \sum_{m=-\infty}^{\infty} \tilde{h}_{t,\tau}[n,m]x[m] \quad \Rightarrow \quad \mathbf{y_t} = \tilde{\mathbf{H}}_\mathbf{t}\mathbf{x_t} \tag{0.40}$$

where $\left[\tilde{\mathbf{H}}_t\right] = \tilde{h}_{t,\tau}[n,m]$.

Frequency Domain matrix form, from (2.37):

$$Y[n] = \sum_{m=-\infty}^{\infty} \tilde{h}_{d,f}[n,m]X[m] \quad \Rightarrow \quad \mathbf{y_f} = \tilde{\mathbf{H}}_\mathbf{f}\mathbf{x_f} \tag{0.41}$$

where $\left[\tilde{\mathbf{H}}_f\right] = \tilde{h}_{d,f}[n,m]$.

2.4.1 Channel Block Model

Equation (2.40) describes the input-output relationship over an infinite stream of samples in time. Practically, the receiver is required to operate on finite segments of time to extract a set of transmitted symbols. This requires the channel to act as a ***correspondence*** (one-to-one mapping) between blocks of transmit symbols in the input and segments of time in the observed output in order for the recovery of the transmitted symbols to be possible.

Square Time Domain Channel Matrix due to Cyclic Prefix

Square Time Domain Channel Matrix due to Zero Prefix

Figure 12: Rectangular to Square Matrix Transformation using Data Redundancy. (Left) Cyclic-prefix redundancy, (Right) Zero-prefix redundancy

However, as is the case for any channel with memory, the channel effectively acts as a $M \to N$ (many to one) mapping, where $M > N$ due to non-zero length impulse responses. By introducing redundancy in the transmitted symbol stream the channel can be converted into a one-to-one mapping [8]. Furthermore, the introduced redundancy must be chosen so that the resulting fat rectangular matrix is rank equivalent to a square matrix so it can be inverted. The two most common examples are the cyclic prefix (CP) and zero prefix (ZP) which are used in CP-OFDM and ZP-OFDM respectively.

For the cyclic prefix case the expressions for the channel matrices are given as follows:

Time Domain

$$\left[\mathbf{H}_{\mathbf{t}}\right]_{n,m} = \bar{h}_{t,\tau}\left[n, < n-m >_N\right] \text{ for } n,m = 0,1,\ldots,N-1 \qquad (0.42)$$

Frequency Domain

$$\left[\mathbf{H_f}\right]_{d,f} = \mathbf{F^H H_t F} \tag{0.43}$$

2.5 Receiver Processing: Channel Estimation and Equalization

Since the main impediment to communication is the channel, the main function of the receiver is to recover the transmitted data symbols by undoing the channel effect. Besides ancillary functions such as time and frequency synchronization, equalizing the channel effect consists of inverting the channel matrix either in the time domain or the frequency domain as given by (2.41) and (2.42) respectively. A practical design consideration is reducing the complexity of the matrix inversion, which can take advantage of the structure in the channel matrix.

Prior to the equalization step, information about the channel must be known in order to reconstruct the channel matrix at the receiver. The channel state information is either known a priori, inferred from observations, or a combination of both, i.e. partial state information in addition to inference. Due to the ever-present noise in the channel, the version of the channel matrix that is obtained is an estimate; the estimation accuracy is limited by the level of noise in the observations and thus the whole process is known as ***channel estimation***.

From (2.40) and (2.41), using a known input vector $\mathbf{x}$ and the corresponding output vector $\mathbf{y}$ an algebraic system of equations in the matrix elements is formed. In its most general form the problem is clearly unsolvable due to the fact that there are N^2 unknowns and only N equations, a situation of zero data communication capacity (since all transmitted elements are known). However for a large class of practical channels the dimensionality or the number of unknowns is reasonably low. Such classes include TI channels, quasi-TI channels, and ***underspread*** TV channels. In contrast, ***overspread*** TV channels have a number of unknown elements in the channel matrix that always exceeds the number of equations.

There are two distinct criteria for classifying channels: the degree of spreading and the rapidity of time variation. The degree of spreading is a measure of the time variation over the time extent of the delay spread with a value of less than 1 corresponding to the under-spread case and the opposite for the overspread case. The rapidity of variation on the other hand measures the time variation over the period of a block in time, such as a symbol or frame period, with a continuum of cases in ascending order of rapidity: Time-invariant or static (TI), Block time-invariant (BTI) or quasi-static, time-varying, and rapidly time-varying, which are illustrated in Fig. 13.

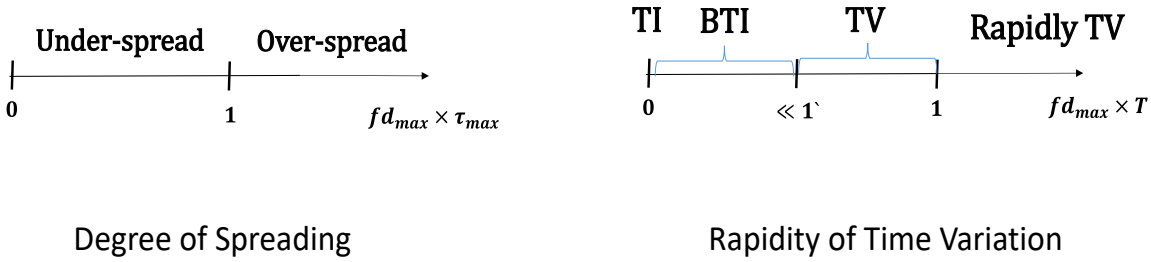

Figure 13: Criteria for Classifying Channels: (Left) Degree of Spreading, (Right) Rapidity of Time Variation.

2.5.1 TI and BTI Channels

In both the TI and BTI cases the time variation is considered non-existent or negligible over the symbol period. As a result the time domain channel matrix $\mathbf{H}_t$ in (2.43) becomes ***circulant*** and the corresponding frequency domain matrix $\mathbf{H}_f$ is then diagonal. The frequency domain diagonal matrix has only *N* unknowns, which can be estimated directly by solving a system of *N* linear equations but would lead to zero data capacity. However, the essential number of unknowns is truly equal to the number of channel delay taps, N_s, which is much less than N for under-spread channels where:

$$\tau_{max} \leq T \leq \frac{1}{\upsilon_{max}} \tag{0.44}$$

From (2.43), the frequency domain channel matrix is given by:

$$\mathbf{H_f} = \mathbf{D}\left(\mathbf{F}\mathbf{h_t}\right) \tag{0.45}$$

where $\mathbf{h_t} = \left[h_0, \ldots, h_{N_s-1}, 0, \ldots, 0\right]^T$ is the first column of the time domain channel matrix $\mathbf{H_t}$ and $\mathbf{D}(.)$ forms a diagonal matrix from a given vector. According to Nyquist sampling, the vector $\mathbf{F}\mathbf{h_t}$ can be reconstructed perfectly from N_s uniformly spaced samples. Pilot symbols, $\mathbf{p}$, are interleaved with data symbols, $\mathbf{d}$, to form the input vector

$$\mathbf{x_f} = \mathbf{p} + \mathbf{d} \tag{0.46}$$

where $\mathbf{p} = \left[p_0, 0, \ldots, 0, p_{\frac{N}{N_s}}, 0, \ldots, 0, p_{(N_s-1)\times\frac{N}{N_s}}\right]$, $\mathbf{d} = \left[0, \mathbf{d}_0^T, 0, \mathbf{d}_1^T, \ldots, \mathbf{d}^T_{(N_s-2)\times\frac{N}{N_s}}, 0\right]$ where $\mathbf{d}_l$ is a vector of data symbols.

For the set $\mathcal{O}$ of pilot location indices in the input symbol vector the corresponding output observation symbols are:

$$\begin{aligned}\mathbf{y_f}^{(\mathcal{O})} &= \mathbf{H_f}^{(\mathcal{O})}\mathbf{p}^{(\mathcal{O})} + \mathbf{n}^{(\mathcal{O})} \\ &= \mathbf{D}\left(\mathbf{p}^{(\mathcal{O})}\right)\mathbf{F}^{(\mathcal{O},[1,N_s])}\,\mathbf{h_t}^{([1,N_s])} + \mathbf{n}^{(O)} \\ &= \mathbf{D}\left(\mathbf{p}^{(\mathcal{O})}\right)\mathbf{F}_{N_s}\,\mathbf{h_t}^{([1,N_s])} + \mathbf{n}^{(\mathcal{O})}\end{aligned} \tag{0.47}$$

where $\mathbf{n}$ is a vector of circular complex Gaussian noise.

The superscript $s\ (s,l)$ denotes the extraction of a subvector (submatrix) of elements (rows, columns) in the sets $s\ (s\times l)$. The following was used to get the final form of (2.47):

$$\mathbf{F}^{(\mathcal{O},[1,N_s])} = \mathbf{F}_{N_s} \tag{0.48}$$

An LS estimate of the channel coefficients can be obtained by inverting the diagonal pilot matrix as follows:

$$\mathbf{D}\left(\mathbf{p}^{(\mathcal{O})}\right)^{-1}\mathbf{y_f}^{(\mathcal{O})} = \mathbf{F}_{N_s}\,\mathbf{h_t}^{([1,N_s])} + \mathbf{D}\left(\mathbf{p}^{(\mathcal{O})}\right)^{-1}\mathbf{n}^{(O)} \tag{0.49}$$

Assuming a constant value of 1 for all pilots gives:

$$\begin{aligned}\mathbf{F}_{N_s}^{H}\mathbf{y}_{\mathbf{f}}^{(\mathcal{O})} &= \mathbf{h}_{\mathbf{t}}^{([1,N_s])} + \mathbf{F}_{N_s}^{H}\mathbf{n}^{(\mathcal{O})} \\ &= \mathbf{h}_{\mathbf{t}}^{([1,N_s])} + \hat{\mathbf{n}}\end{aligned} \tag{0.50}$$

where $\hat{\mathbf{n}}$ is the inverse Fourier transform of the noise vector $\mathbf{n}$ which remains circularly complex Gaussian. Thus, the estimates of the delay taps can be found as follows:

$$\hat{\mathbf{h}}_{\mathbf{t}}^{([1,N_s])} = \mathbf{F}_{N_s}^{H}\mathbf{y}_{f}^{(\mathcal{O})} \tag{0.51}$$

The estimate of the channel matrix can be obtained by substituting (2.51) in (2.45) giving:

$$\hat{\mathbf{H}}_{f} = \mathbf{D}\left(\mathbf{F}^{([1,N],[1,N_s])}\mathbf{F}_{N_s}^{H}\mathbf{y}_{\mathbf{f}}^{(\mathcal{O})}\right) \tag{0.52}$$

The matrix $\mathbf{F}^{([1,N],[1,N_s])}\mathbf{F}_{N_s}^{H}$ when expanded has the familiar Dirichlet interpolation form:

$$\begin{aligned}\left[\mathbf{F}^{([1,N],[1,N_s])}\mathbf{F}_{N_s}^{H}\right]_{n,l} &= \frac{1}{N}\sum_{k=0}^{N_s-1} e^{\frac{-j2\pi k\left(n-\frac{lN}{N_s}\right)}{N}} \\ &= \frac{1}{N}\frac{e^{\frac{-j2\pi N_s\left(n-\frac{lN}{N_s}\right)}{N}}-1}{e^{\frac{-j2\pi\left(n-\frac{lN}{N_s}\right)}{N}}-1} \\ &= \frac{1}{N}e^{-\frac{j\pi(N_s-1)\left(n-\frac{lN}{N_s}\right)}{N}}\frac{\sin\left(\frac{\pi N_s}{N}\left(n-\frac{lN}{N_s}\right)\right)}{\sin\left(\frac{\pi}{N}\left(n-\frac{lN}{N_s}\right)\right)}\end{aligned} \tag{0.53}$$

Consequently, equalization consists of a division by a constant, which is known as single tap equalization, as follows:

$$\hat{\mathbf{x}}_{\mathrm{f}}(k) = \frac{\mathbf{y}_{\mathrm{f}}(k)}{\hat{\mathbf{H}}_{\mathbf{f}}(k,k)} \tag{0.54}$$

which gives the LS estimate for the data symbols.

To reduce the noise enhancement, MMSE equalization is used which takes the noise into account:

$$\hat{\mathbf{x}}_{\mathbf{f}}(k) = \frac{\mathbf{y}_{\mathrm{f}}(k)}{\hat{\mathbf{H}}_{\mathbf{f}}(k,k) + \sigma_n^2} \tag{0.55}$$

where σ_n^2 is the noise power.

2.5.2 TV Channels

In rapidly time varying channels the time-domain channel matrix is no longer circulant. Consequently the frequency domain matrix is no longer diagonal, however the diagonal bandedness property persists. Unlike the TI case the essential number of degrees of freedom is not always less than *N*, the number of observation samples per block. In the TV case, the essential number of degrees of freedom or the dimensionality *D* is given by:

$$\begin{aligned} D &= \left(\frac{\tau_{max} B}{2\pi}\right)\left(2\upsilon_{max} T\right) \\ &= \tau_{max} f_s \frac{2\upsilon_{max} N}{f_s} \\ &= 2\tau_{max}\upsilon_{max} N \end{aligned} \tag{0.56}$$

Thus, only underspread channels ($2\tau_{\max}\upsilon_{max} < 1$) are guaranteed to be ***identifiable.***

In the TI case, the frequency domain channel matrix was related to its essential number of degrees of freedom, the number of delay taps, which can be rewritten as:

$$\mathbf{H}_{\mathbf{f}} = \mathbf{D}\left(\mathbf{h}_{\mathbf{t}}^{([1,N_s])^T}\mathbf{F}^{([1,N],[1,N_s])^T}\right) \tag{0.57}$$

where the vector $\mathbf{h}_{\mathbf{t}}^{([1,N_s])^T}\mathbf{F}^{([1,N],[1,N_s])^T}$ can be thought of as the transfer function.

A small set of delay taps describes the correlation/smoothness of the channel transfer function in the frequency domain. By analogy, an essential representation of the time-varying transfer function can be given by:

$$\mathbf{H}_{\text{tf}} = \mathbf{F}^{\left([1,N],\left[-\frac{M_d}{2},\frac{M_d}{2}-1\right]\right)}\mathbf{\Lambda}\mathbf{F}^{([1,N],[1,N_s])^T} \tag{0.58}$$

Figure 14 shows the essential representations of both the time-invariant transfer function represented by the vector $\mathbf{h}_{\mathbf{t}}^{([1,N_s])^T}\mathbf{F}^{([1,N],[1,N_s])^T}$ in (2.57) in the top and the time-varying transfer function given by (2.58) in the bottom. In the TI case, the variation across frequency was expressed as a linear combination of the DFT basis sequences. For the time-varying case, both the time variation and variation across frequency are expressed in terms of DFT bases and the expansion coefficients are contained in the matrix $\mathbf{\Lambda}$. This representation is known as a Basis Expansion Model (BEM).

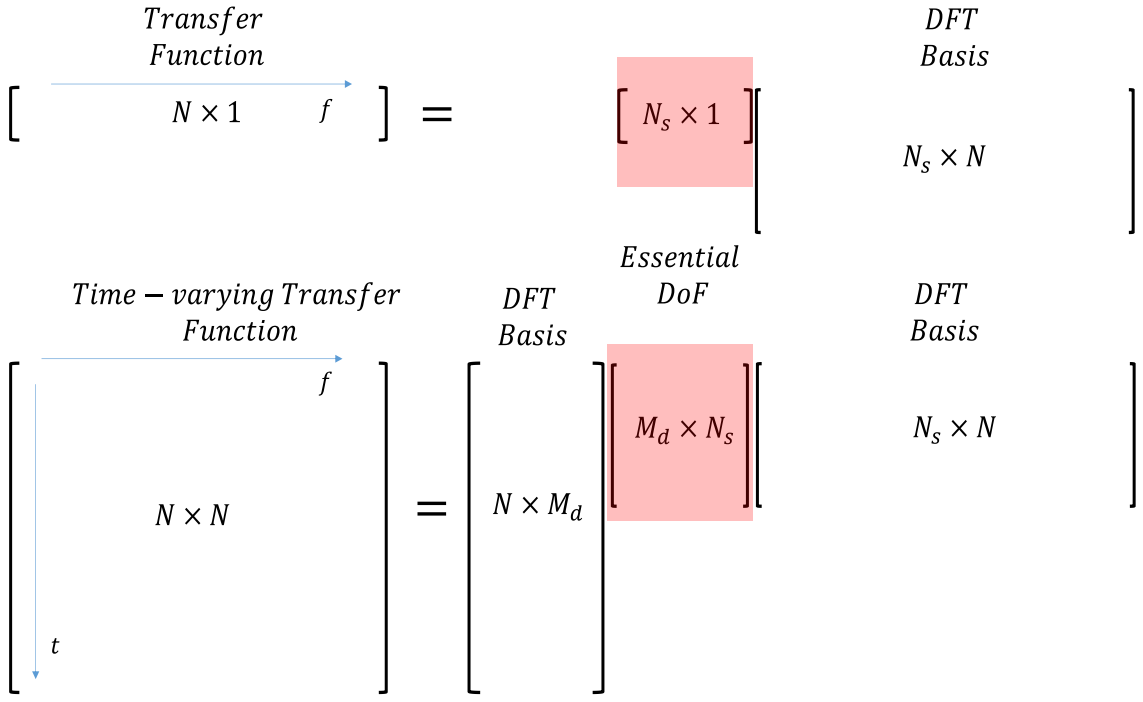

Figure 14: Essential Degrees of Freedom of a Channel: (Top) TI Channel Transfer Function, (Bottom) TV channel time-varying transfer function.

Similarly, the frequency domain and time domain channel matrices in (2.43) and (2.44) respectively can be expressed in terms of a BEM expansion [12]. Leaving out the right most DFT matrix in (2.59) gives a matrix $\underline{\underline{\mathbf{H}}}_{\mathrm{t},\tau}$ having the time varying taps on the columns:

$$\underline{\underline{\mathbf{H}}}_{\mathrm{t},\tau} = \mathbf{F}^{\left([1,N],\left[-\frac{M_d}{2},\frac{M_d}{2}-1\right]\right)}\boldsymbol{\Lambda} \tag{0.59}$$

The l-th column of $\underline{\underline{\mathbf{H}}}_{\mathrm{t},\tau}$ is given by:

$$\mathbf{h}_l = \mathbf{F}^{\left([1,N],\left[\frac{-M_d}{2},\frac{M_d}{2}-1\right]\right)}\left[\lambda_{l,0},...,\lambda_{l,M_d-1}\right]^T \tag{0.60}$$

where $\left[\lambda_{l,0},...,\lambda_{l,M_d-1}\right]^T$ is the l-th column of $\boldsymbol{\Lambda}$.

The time domain channel matrix, $\mathbf{H_t}$ is constructed by placing the columns of $\underline{\underline{\mathbf{H}}}_{\mathrm{t},\tau}$ along the circulant diagonals as follows:

$$\begin{aligned}\mathbf{H_t} &= \sum_{l=0}^{N_s-1}\mathbf{D}\left(\mathbf{h}_l\right)\mathbf{Z}^l \\ &= \sum_{l=0}^{N_s-1}\sum_{k=0}^{M_d-1}\lambda_{l,k}\mathbf{D}\left(\mathbf{f_k}\right)\mathbf{Z}^l \\ &= \sum_{l=0}^{N_s-1}\sum_{k=0}^{M_d-1}\lambda_{l,k}\boldsymbol{\Gamma}_{\boldsymbol{l,k}}\end{aligned} \tag{0.61}$$

where $\left[\mathbf{f}_k\right]_n = e^{\frac{j2\pi\left(k-\frac{M_d}{2}\right)n}{N}}$, $\mathbf{Z}$ is the identity matrix circularly shifted downwards by 1 position and $\boldsymbol{\Gamma}_{l,k} = \mathbf{D}\left(\mathbf{f}_k\right)\mathbf{Z}^l$.

Defining the following concatenated matrices:

$$\boldsymbol{\Gamma} = [\boldsymbol{\Gamma}_{0,0},\ldots,\boldsymbol{\Gamma}_{0,M_d-1},\boldsymbol{\Gamma}_{N_s-1,0},\ldots,\boldsymbol{\Gamma}_{N_s-1,M_d-1}] \tag{0.62}$$

$$\boldsymbol{\lambda} = \left[\lambda_{0,0},...,\lambda_{0,M_d-1},\lambda_{N_s-1,0},...,\lambda_{N_s-1,M_d-1}\right]^T \tag{0.63}$$

we can rewrite (2.61) as:

$$\mathbf{H}_t = \boldsymbol{\Gamma}\left(\boldsymbol{\lambda} \otimes \mathbf{I}_N\right) \tag{0.64}$$

Substituting (2.64) into (2.43) gives the frequency domain channel matrix:

$$\begin{aligned} \mathbf{H}_f &= \mathbf{F}\mathbf{H}_t\mathbf{F}^H \\ &= \mathbf{F}\boldsymbol{\Gamma}\mathbf{F}^H\left(\boldsymbol{\lambda} \otimes \mathbf{I}_N\right) \\ &= \boldsymbol{\Gamma}_f\left(\boldsymbol{\lambda} \otimes \mathbf{I}_N\right) \end{aligned} \tag{0.65}$$

where $\boldsymbol{\Gamma}_f = \mathbf{F}\boldsymbol{\Gamma}\mathbf{F}^H$.

The channel estimation consists of finding the vector of coefficients λ . As was shown in Fig. 11, both the time domain and frequency domain channel matrices have a banded structure which requires special considerations in the pilot symbol arrangement in order to estimate the channel coefficients. The pilot scheme used is illustrated in Fig. 15, which consists of an ON pilot at location p surrounded by a null interval, $\mathcal{G}:\left\{n \in \left[(g-1)/2 : (g-1)/2\right], n \neq p\right\}$, and has been shown to be optimal [13]. To reduce the effect of ICI contamination from adjacent data, a subset of the pilots, $\mathcal{O} \subset \mathcal{G}$ is used for the observation data and the highly corrupted peripheral pilots are avoided since – as will be shown in the following chapter – they lead to an increase in the estimation error.

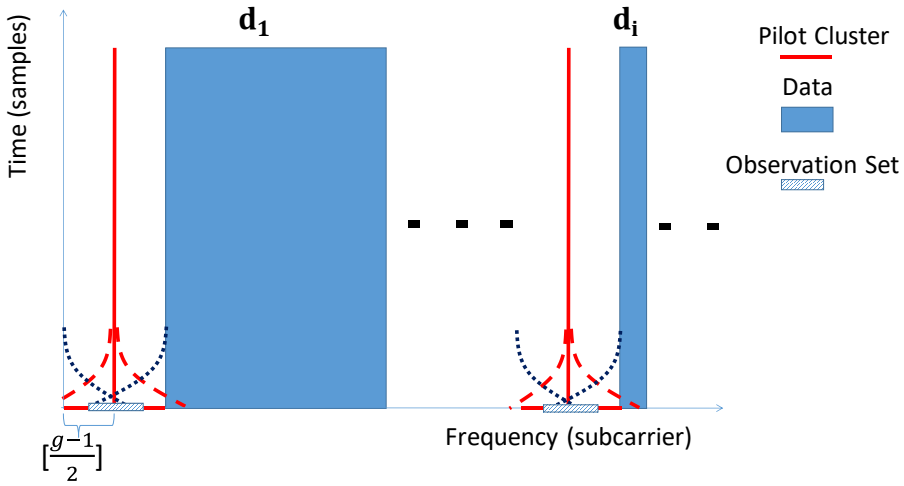

Figure 15: Uniformly-Spaced Zero Guarded Pilot Pattern

Due to the duality between the time and frequency domain channel matrices, the pilot-based channel estimation treatment in one of them is representative. The input-output relationship in the frequency domain is given by:

$$\begin{aligned}\mathbf{y_f} &= \mathbf{H_f x_f} + \mathbf{n} \\ &= \mathbf{\Gamma}_f \left(\boldsymbol{\lambda} \otimes \mathbf{I}_N\right)\mathbf{x_f} + \mathbf{n} \\ &= \mathbf{\Gamma}_f \left(\mathbf{I}_{N_s \times M_d} \otimes \mathbf{x_f}\right)\boldsymbol{\lambda} + \mathbf{n}\end{aligned} \tag{0.66}$$

Substituting (2.46) into (2.66) and using the subset of observation samples $\left(\mathcal{O}\right)$:

$$\begin{aligned}\mathbf{y}_f^{(\mathcal{O})} &= \left(\Gamma_{\mathbf{f}}\left(\mathbf{I}_{N_s \times M_d} \otimes \mathbf{p}\right)\right)^{(\mathcal{O})}\boldsymbol{\lambda} + \left(\Gamma_{\mathbf{f}}\left(\mathbf{I}_{N_s \times M_d} \otimes \mathbf{d}\right)\right)^{(\mathcal{O})}\boldsymbol{\lambda} + \mathbf{n}^{(\mathcal{O})} \\ &= \left(\boldsymbol{\psi}_{\mathrm{p}}\right)^{(\mathcal{O})}\boldsymbol{\lambda} + \left(\boldsymbol{\psi}_{\mathrm{d}}\right)^{(\mathcal{O})}\boldsymbol{\lambda} + \mathbf{n}^{(\mathcal{O})}\end{aligned} \tag{0.67}$$

The middle term in (2.67) represents side leakage from adjacent data symbols.

The LS estimate of the coefficient vector is obtained as follows:

$$\hat{\boldsymbol{\lambda}} = \left(\left(\boldsymbol{\psi}_p\right)^{(\mathcal{O})}\right)^{\dagger}\mathbf{y}_{\mathbf{f}}^{(\mathcal{O})} \tag{0.68}$$

where $(.)^{\dagger}$ denotes the pseudo-inverse operation.

CHAPTER 3 BEM REPRESENTATIONS OF TIME-VARYING CHANNELS

In Chapter 2, the complex exponential basis CE-BEM was used to represent the time variation of the delay taps leading to a channel matrix representation with only the essential number of unknowns $N_s\left(\tau_{max}\right)$ and $M_d\left(\upsilon_{max}\right)$. This was motivated by the underlying physical model where multiple signal versions arrive along different paths in clusters, each cluster corresponding to a time-varying delay tap. The time variation of each delay tap is a result of the sum of the components within a single cluster each having a different Doppler frequency shift due to an angle of arrival relative to the velocity of movement.

In the left side of Fig. 15 an illustration is given for paths belonging to a single cluster where only 4 components are shown incident on a moving antenna with angles $\theta_1,\ \theta_2,\ \theta_3,\ \theta_4$ relative to the velocity vector v.

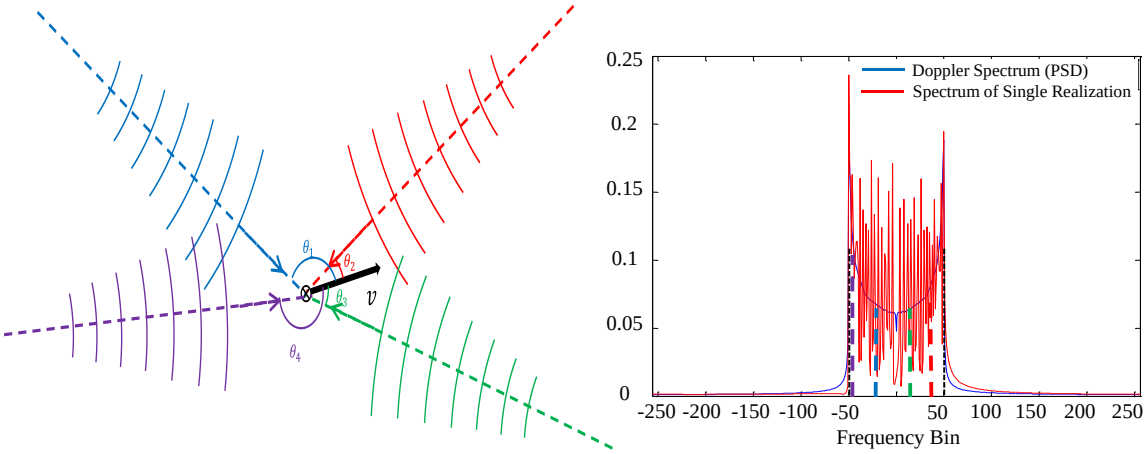

Figure 16: (Left) Signal Arrival Paths at Different Angles in the Azimuthal Plane. (Right) Doppler Spectrum due to 2-D Isotropic Distribution of Signal Arrival Paths.

On the right side of Fig. 15 is the PSD of the signal corresponding to time variation of a single tap and the 4 Doppler shifts corresponding to the wave components shown on the

left (in corresponding colors). The Doppler spectrum was generated for a sample window of length $N = 512$ for a signal having maximum Doppler of $\upsilon_{max} = 50$ cycles/window and taking the discrete Fourier transform. In theory, it is known that the Doppler PSD is strictly limited at the edges, however due to the Gibbs phenomenon frequency components can be observed beyond the edge frequencies of -50 and 50. From a BEM representation point of view, this shows that using the complex exponential basis (CE-BEM) requires more components than those in $[-\upsilon_{max}, \upsilon_{max}]$ to get a faithful representation of the time-varying taps. A BEM using the Discrete Prolate Spheroidal Sequence (DPS) basis set can give a faithful representation using only a number of parameters equal to the essential degrees of freedom of the channel [13].

3.1 Discrete Prolate Spheroidal Sequences

As explained in Chapter 2, no pulse shape exists that has strictly limited bandwidth and time extent. However, David Slepian in [14] solved the problem of finding sequences that are strictly bandlimited to a certain bandwidth interval, $\left[-B/2, B/2\right]$, and achieve the highest energy concentrations, i.e. essentially limited over a finite time segment of length L. In addition, when such sequences are truncated, and thus forced to be strictly time-limited to an interval of length L, they become maximally concentrated over the bandwidth $\left[-B/2, B/2\right]$. These properties are summarized in Table1.

Table 2: Infinite and finite versions of DPS sequences in time and frequency

	Bandwidth Extent	**Time Extent**	**Concentration**
$U(\nu)=\sum_{m=-\infty}^{\infty}u[m]e^{-j2\pi m\nu}$ $u[m]=\int_{-\frac{B}{2}}^{\frac{B}{2}}U(\nu)e^{j2\pi m\nu}d\nu$	$[-B/2, B/2]$	Infinite	Time $\lambda(B,L)=\frac{\sum_{m=0}^{L-1}\lvert u[m]\rvert^2}{\sum_{m=-\infty}^{\infty}\lvert u[m]\rvert^2}$
$U(\nu)=\sum_{m=0}^{L-1}u[m]e^{-j2\pi m\nu}$ $u[m]=\int_{-\infty}^{\infty}U(\nu)e^{j2\pi m\nu}d\nu$	Infinite	$[0, L-1]$	Frequency $\lambda(B,L)=\frac{\int_{-\frac{B}{2}}^{\frac{B}{2}}\lvert U(\nu)\rvert^2 d\nu}{\int_{-\infty}^{\infty}\lvert U(\nu)\rvert^2 d\nu}$

The DPS sequences are obtained by solving an optimization problem [14] that leads to a Rayleigh Quotient problem which has the same solution as the eigenvalue equation given in (3.1). The sequences and their corresponding concentrations are a function of the parameters (B,L).

$$\sum_{l=0}^{L-1}\frac{\sin\left(2\pi B(l-m)\right)}{\pi(l-m)}u[m]=\lambda u[m] \quad for \ \ m\in\mathbb{Z} \tag{0.69}$$

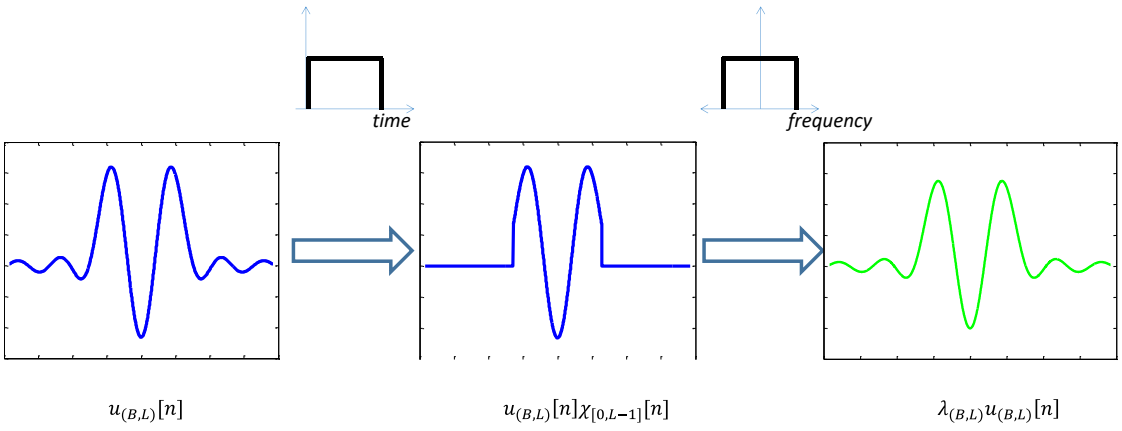

Figure 17: DPS sequence truncated in time followed by low-pass filtering which restores a scaled version of the original

Equation (3.1) can be interpreted to be, as illustrated in Fig. 16, a time truncation operation followed by low pass filtering.

The conventional wisdom expression for dimensionality of a signal is given by $D = BT$. This means that D BEM coefficients are sufficient to exactly describe the signal. However, this value is only a lower bound that is never exactly attained without residual modeling error in the approximation. The degree to which the modeling error can be reduced is dependent on the choice of the basis set. Figure 17 shows a log scale comparison between the Complex Exponential (CE)-BEM component analysis on the left and a DPS component analysis on the right of a channel realization having the same parameters as those in Fig. 15.

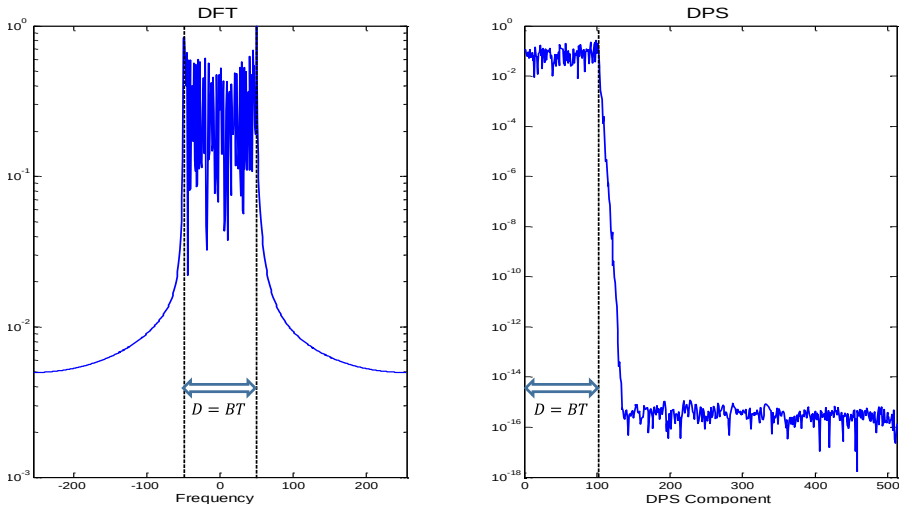

Figure 18: Component analysis of a TV signal with $BT = 100$: DFT Basis (Left) and DPS Basis (Right).

The DPS component analysis shows the region of components of significant magnitude to be well contained within the interval $[0, D]$ unlike the case for the DFT component analysis. However, a transition band of components exists that partially contains non-negligible components.

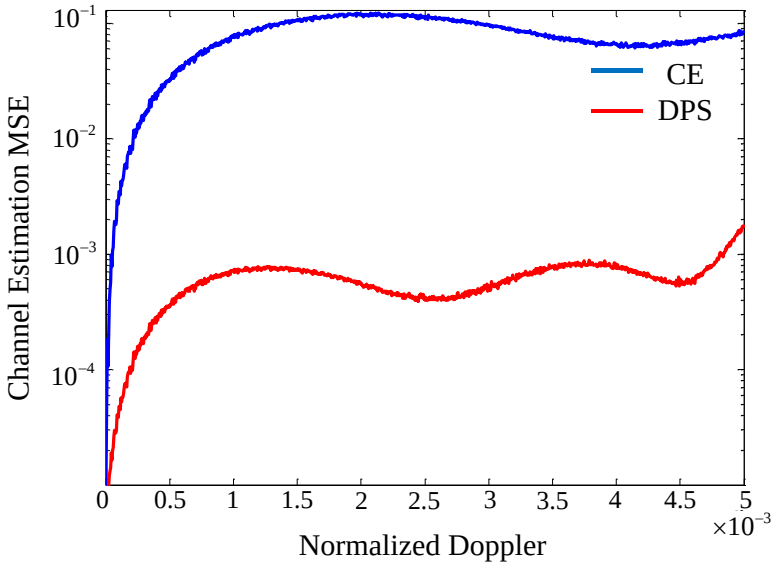

Figure 19: Channel Estimation MSE Comparison between CE and DPS BEMs over a Range of Velocities.

Figure 18 shows a channel estimation MSE performance comparison between CE and DPS over a range of velocities having a corresponding range of Doppler frequencies in the range $[0,5\times10^{-3}]$. This plot was originally shown in [15] and reproduced here. A time-selective frequency flat (single delay tap) channel scenario consisting of 2000 independent realizations was considered and a time-based pilot scheme consisting of 10 uniformly spaced time samples to estimate 5 BEM components. Considering the maximum Doppler frequency in the range, the nominal dimension size is $D = 2\upsilon_{max}L = 3.$

3.2 DPS-based Channel Estimation for OFDM signal in Frequency Invariant Channels

In this section, the simple case of a single tap frequency invariant channel acting on an OFDM signal is considered and the channel estimation is done using pilot tones, i.e. frequency domain pilots. The zero-guarded pilot cluster scheme is used for the pilot placement. For the single tap case only one pilot cluster is required. This pilot scheme was shown to be optimal if the channel can be modeled perfectly by a basis subset of the CE-BEM [13]. However, since the DPS representation is the optimal channel representation, the truly optimal pilot placement is unknown. Nevertheless, knowing that the ICI effect is

the main source of error makes the zero-guarded pilot cluster scheme an intuitively viable option.

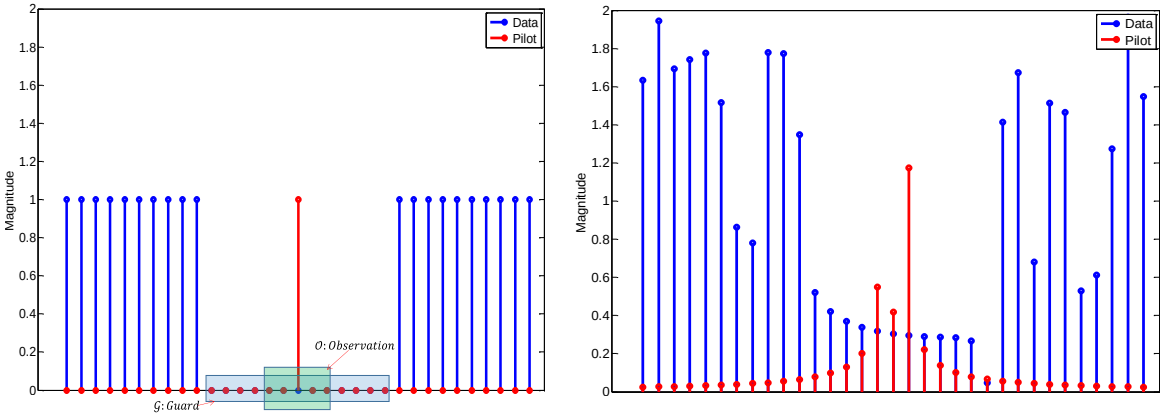

Figure 20: (Left) Symbol consisting of Data and Pilot Cluster. (Right) ICI between Pilot Cluster and Data.

The input frequency domain vector can be expressed as the orthogonal (direct) sum of pilot and data vectors:

$$\mathbf{x}_{\mathrm{f}} = \mathbf{e}_p + \mathbf{d} \tag{0.70}$$

where $\mathbf{e}_p$ is the p^{th} column of the identity matrix.

The recovered symbol vector – after FFT processing at the receiver is given by:

$$\begin{aligned} \mathbf{z} &= \mathbf{FD}(\mathbf{h})\mathbf{F}^H\mathbf{x}_{\mathrm{f}} + \mathbf{Fn} \\ &= \mathbf{FD}(\mathbf{h})\mathbf{F}^H\mathbf{e}_p + \mathbf{FD}(\mathbf{h})\mathbf{F}^H\mathbf{d} + \mathbf{Fn} \\ &= \mathbf{FD}(\mathbf{f}_p^*)\mathbf{F}^H\mathbf{e}_p + \mathbf{FD}(\mathbf{h})\mathbf{F}^H\mathbf{d} + \mathbf{Fn} \\ &= \frac{1}{\sqrt{N}}\mathbf{P}^p\mathbf{Fh} + \mathbf{FD}(\mathbf{h})\mathbf{F}^H\mathbf{d} + \mathbf{Fn} \end{aligned} \tag{0.71}$$

where $\mathbf{h}$ is a vector of the single tap time varying channel, $\mathbf{P}$ is the circularly downshifted identity matrix, $\mathbf{f}_p$ is the p^{th} column of the DFT matrix $\mathbf{F}$ and $\mathbf{n}$ is the noise vector. Substituting using the DPS BEM representation for the channel vector:

$$\mathbf{z} = \frac{1}{\sqrt{N}}\mathbf{P}^{p}\mathbf{F}\mathbf{S}_{\mathbf{p}}\boldsymbol{\alpha} + \mathbf{F}\mathbf{D}\left(\mathbf{S}_{\mathbf{p}}\boldsymbol{\alpha}\right)\mathbf{F}^{H}\mathbf{d} + \mathbf{F}\mathbf{n} \tag{0.72}$$

where $\mathbf{S}_{\mathbf{p}}$ is a $N \times D$ matrix with the first D DPS basis components as its columns and $\boldsymbol{\alpha}$ a $D \times 1$ column consisting of the linear combination coefficients.

As shown in Fig. 19 on the left, a subinterval $\mathcal{O}$ of the pilot cluster $\mathcal{G}$, is used as observation samples for LS estimation:

$$\mathbf{z}^{(\mathcal{O})} = \frac{1}{\sqrt{N}}\mathbf{P}^{p(\mathcal{O})}\mathbf{F}\mathbf{S}_{\mathbf{p}}\boldsymbol{\alpha} + \mathbf{F}^{(\mathcal{O})}\mathbf{D}\left(\mathbf{S}_{\mathbf{p}}\boldsymbol{\alpha}\right)\mathbf{F}^{H}\mathbf{d} + \mathbf{F}^{(\mathcal{O})}\mathbf{n} \tag{0.73}$$

The LS estimate is given by:

$$\tilde{\boldsymbol{\alpha}} = \sqrt{N}\left(\mathbf{P}^{p(\mathcal{O})}\mathbf{F}\mathbf{S}_{\mathbf{p}}\right)^{\dagger}\mathbf{z}^{(\mathcal{O})} \tag{0.74}$$

There are three sources that contribute to the error in the channel estimate:

1) The modeling error which depends on D, the subset of the basis.
2) ICI due to data subcarriers, which is represented by the second term in the r.h.s of (3.5) and illustrated in Fig. 19.
3) AWGN noise.

Ignoring the effect of noise, Fig. 21 shows the effect of ICI on LS estimation MSE by comparing the cases with and without data. The MSE is plotted against observation set sizes in the range $|\mathcal{O}| \in \left[3, |\mathcal{G}|\right]$, with the dimension size being a variable parameter and the size of the guard interval fixed to $|\mathcal{G}| = 21$.

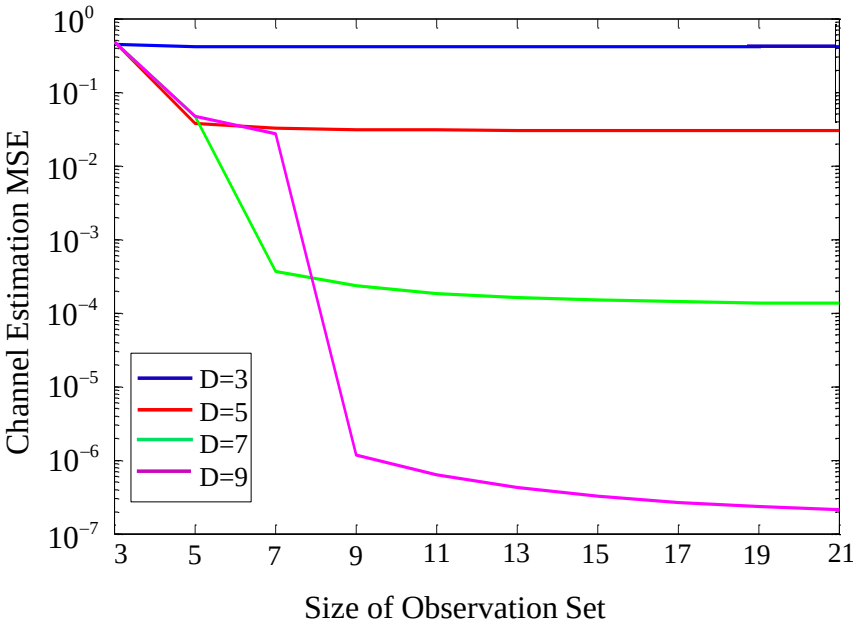

Figure 21: LS channel estimation MSE without Data.

Figure 21 shows channel estimation MSE when no data is present. For each parameter trace, the channel estimation MSE drops monotonically saturating at the maximum when the size of the observation set is equal to the number of dimensions D . This drop is a result of the reduction of the modelling error component which is fully attained when $|\mathcal{O}| \geq D$, i.e. when the matrix $\mathbf{P}^{p(\mathcal{O})}\mathbf{FD}$ is no longer fat. Thus, the most efficient choice for the size of the observation set is to be equal to the number of dimensions.

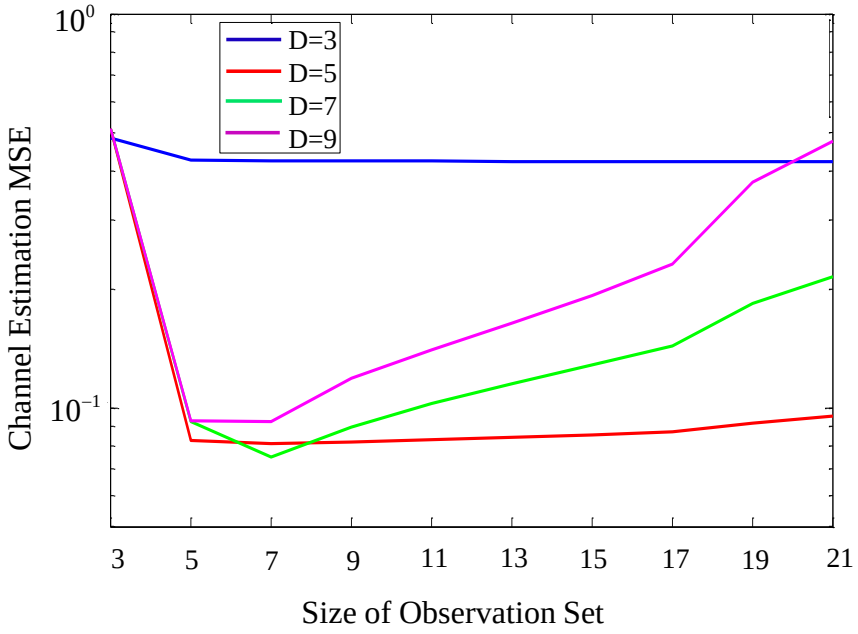

Figure 22: LS channel estimation MSE with Data.

Figure 22 shows channel estimation MSE when data is present for the same realizations used in Fig. 21. The traces exhibit a drop in MSE up till a certain point after which the MSE starts rising. This can be explained by the interplay of the two opposing effects of reduction in modeling error and increase in the number of ICI corrupted observation samples. This behavior places a lower bound on the attainable LS estimation MSE for a guard interval of fixed size, which for the given example is $D = 7$. More quantitatively this can be described by the following proposition.

Proposition 2.1:

For a particular value of $|\mathcal{G}|$*, there exists a dimension size, defined as the effective dimensionality,* $D_{eff} = f\left(|\mathcal{G}|\right)$, $D_{eff} \leq |\mathcal{G}|$ *for the DPS BEM representation describing the time variation of the channel at which the LS estimation MSE error is minimized.*

Thus the parameter D_{eff} defines the number of useful dimensions, a parameter that can be estimated. Hence an important figure of merit can be defined for which we coin the term "Guard pilot chunk estimation efficiency":

$$\epsilon_g = \frac{D_{eff}}{|\mathcal{G}|} \tag{0.75}$$

For the given example, LS estimation yields $\epsilon_g = \frac{7}{21} = 0.33$ which is not very efficient. This motivates the search for a more efficient channel estimation method that does not rely on the full knowledge of channel statistics.

In order to analyze the increase in error behavior shown in the right side of Fig. 20, the relative errors of each of the individual DPS coefficients are examined. Figure 21 shows the relative error of the individual DPS coefficients for different basis subset sizes where the minimum observation set size is used, i.e. $|\mathcal{O}| = D$. As shown, the relative error increases with the order of the DPS component which can be attributed to the fact that the frequency spectrum of higher order DPS sequences is less concentrated and thus more susceptible to ICI corruption. It is worth noting that the edge coefficients have excessively high relative errors, which in practice can be detected using the knowledge of bounds on the possible values for edge coefficients.

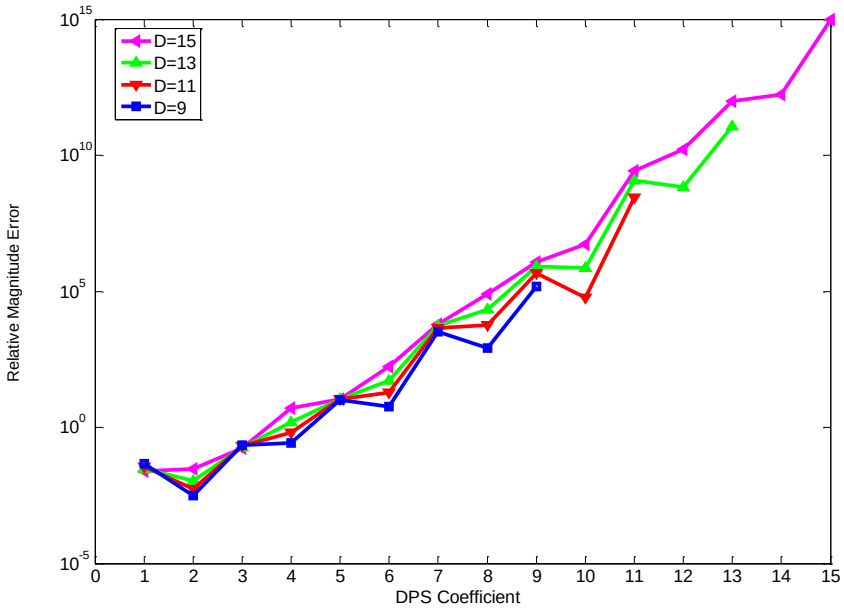

Figure 23: Magnitude of Relative Error of DPS Coefficients

3.2.1 Bounds on the DPS Coefficients

Certain upper bounds exist that apply to edge coefficients which can be used to control the excessive error described in the previous section. The bounds are based on the following theorem.

Theorem 3.1:

Given $f(t) \in \mathcal{L}^2_{\frac{T}{2}}$ *where* $\mathcal{L}^2_{\frac{T}{2}}$ *is the space of functions of finite energy over the interval* $\left[\frac{-T}{2}, \frac{T}{2}\right]$ *but* $f(t)$ *is not necessarily strictly bandlimited, an approximating function* $g(t) \in \mathcal{B}_B$ *can be found, where* $\mathcal{B}_B$ *is the space of functions that are strictly bandlimited to bandwidth* B *and have finite energy given by:*

$$g(t) = \sum_{i=0}^{\infty} b_i \psi^{(i)}_{[B,T]}(t), \quad -\infty < t < \infty \tag{0.76}$$

where $\psi_{[B,T]}^{(i)}(t)$ *is the* i^{th} *out of the countably infinite set (continuous time) of prolate spheroidal wave functions for parameters* (B,T). *There exists a cutoff index* $i = e$ *beyond which the coefficients* b_i *are governed by upper bounds* $\hat{b}_i$ *related by the ratio:*

$$\hat{b}_i = \frac{\sqrt{\lambda_{[B,T]}^{(i)}}}{\sqrt{\lambda_{[B,T]}^{(j)}}} \hat{b}_j \ \text{for } i, j = e, \ldots$$

where $\lambda_{[B,T]}^{(i)}$ *is the eigenvalue corresponding to the prolate spheroidal wave function* $\psi_{[B,T]}^{(i)}(t)$.

Proof:

Since $f(t) \in \mathcal{L}_{\frac{T}{2}}^2$, *by the completeness and orthogonality of the set* $\psi_{[B,T]}^{(i)}(t)$ *over* $\mathcal{L}_{\frac{T}{2}}^2$ *and the known properties of* $\psi_{[B,T]}^{(i)}(t)$, $f(t)$ *is given by:*

$$f(t) = \sum_{i=0}^{\infty} a_i \psi_{[B,T]}^{(i)}(t) \ \text{for} -\frac{T}{2} \le t \le \frac{T}{2} \tag{0.77}$$

where $a_i = \frac{1}{\lambda_{[B,T]}^{(i)}} \int_{-\frac{T}{2}}^{\frac{T}{2}} f(t) \psi_{[B,T]}^{(i)}(t)\, dt$.

However, due to $f(t) \notin \mathcal{B}_B$ the convergence of the power series in (3.10) is only guaranteed within the interval $-T/2 \le t \le T/2$.

The energy of $f(t)$ over the interval $-T/2 \le t \le T/2$, denoted by E_T, is given by:

$$
\begin{aligned}
E_T &= \int_{-\frac{T}{2}}^{\frac{T}{2}} f(t)\, f^*(t)\, dt \\
&= \sum_{i=0}^{\infty}\sum_{j=0}^{\infty} a_i a_j^* \int_a^b \psi_{[B,T]}^{(i)}(t)\psi_{[B,T]}^{(j)}(t)\, dt \\
&= \sum_{i=0}^{\infty}\sum_{j=0}^{\infty} a_i a_j^* \lambda^{(i)} \delta(i-j) \\
&= \sum_{i=0}^{\infty} \lambda^{(i)} |a_i|^2
\end{aligned}
\tag{0.78}
$$

Given that E_T is finite, an upper bound on the coefficients is given as follows:

$$
|a_i| \le \sqrt{\frac{E_T}{\lambda^{(i)}}} \tag{0.79}
$$

Following the procedure described in [16], a strictly bandlimited function, $g(t) \in \mathcal{B}_B$, can be found that minimizes the energy of the difference relative to $f(t)$ over the finite time interval $-T/2 \le t \le T/2$, denoted by $\|g(t) - f(t)\|_T^2$, subject to a constraint on the energy outside the time interval $-T/2 \le t \le T/2$:

$$
\min \|g(t) - f(t)\|_T^2 \text{ such that } \|g(t)\|_\infty^2 - \|g(t)\|_2^2 = \varepsilon \tag{0.80}
$$

The solution is given by the following infinite sum:

$$
g(t) = \sum_{i=0}^{\infty} b_i \psi_{[B,T]}^{(i)}(t) \quad -\infty \le t \le \infty \tag{0.81}
$$

However, now the convergence is attained over all time and due to the strict bandlimitedness of $\psi_{[B,T]}^{(i)}(t)$.

Dropping the subscript $[B,T]$ in the notation for the eigenvalues, the expansion coefficients are related to those for the expansion of $f(t)$ by the following relationship:

$$b_i = \frac{a_i \lambda^{(i)}}{\mu\left(1-\lambda^{(i)}\right)+\lambda^{(i)}} \tag{0.82}$$

where μ is a positive constant satisfying:

$$\epsilon = \sum_{i=0}^{\infty} \frac{\left|a_i\right|^2 \left(\lambda^{(i)}\right)^2}{\left[\mu\left(1-\lambda^{(i)}\right)+\lambda^{(i)}\right]^2} \tag{0.83}$$

Using the property that the eigenvalues $\lambda^{(i)} > \lambda^{(i+1)} > \ldots$ decay monotonically and that $\lim_{i\to\infty} \lambda^{(i)} = 0$, for sufficiently large i the value of the denominator in (3.15) approaches μ and we get:

$$b_i \approx \frac{a_i \lambda^{(i)}}{\mu} \tag{0.84}$$

On the other hand, for the first few coefficients λ^i is not negligible with respect to 1 and (3.14) can be written as:

$$b_i \approx \frac{a_i \lambda^{(i)}}{\lambda^{(i)}} \approx a_i \tag{0.85}$$

Thus, there exists a "cutoff point" beyond which the coefficients follow the rapid decay of the eigenvalues.

Substituting (3.11) into (3.17), an upper bound can be obtained on the magnitude of the b_i coefficients, which we denote by $\hat{b}_i$:

$$\left|b_i\right| \le \hat{b}_i = \frac{\sqrt{\lambda^{(i)}}\sqrt{E_T}}{\mu} \tag{0.86}$$

Dividing the upper bounds for two indices $i, j \ge e$ completes the proof.

Corollary 3.1:

For a function $f(t)$ *that is obtained by time windowing a strictly bandlimited infinite energy (power)* $\tilde{f}(t)$ *of bandwidth* B*, the discrete sequences* $f[n]$ *and* $g[n]$ *obtained by sampling* $f(t)$ *and the corresponding* $g(t)$ *at a rate* $f_s = 2B$ *preserves the results of the theorem.*

Proof:

$$f(t) = \begin{cases} \tilde{f}(t) & for -\frac{T}{2} \le t \le \frac{T}{2} \\ 0 & otherwise \end{cases} \tag{0.87}$$

The continuous function $f(t)$ is no longer strictly bandlimited but of finite energy and thus is governed by the above theorem.

Since $f(t)$ is obtained from a strictly bandlimited function with bandwidth B and $g(t)$ is strictly bandlimited to the same bandwidth, sampling at a rate $f_s = 2B$ preserves the results of the continuous case to the discrete case.

The direct utility of Theorem 3.1 is limited due to the fact that it gives a ratio between 2 upper bounds that are initially not known. Assuming that all channel realizations are of a known fixed energy E_f we have the following bound on the coefficients:

$$|b_i| \le \sqrt{E_f} \tag{0.88}$$

Initially, it is tempting to substitute using this bound for the cutoff coefficient in the upper bound ratio given by Theorem 3.1 and get a tight absolute bound on all coefficients as follows:

$$\hat{b}_i = \frac{\sqrt{\lambda_{[B,T]}^{(i)}}}{\sqrt{\lambda_{[B,T]}^{(e)}}} \sqrt{E_f} \quad for\, i = e, \ldots \tag{0.89}$$

However, given the fact that the result of Theorem 3.1 can be true for a different bound while (3.21) is only a *bound*, the result from the above substitution should not be expected to be completely valid. As a check for the validity of the hypothesized upper bound, 10000 realizations of a TV channel with parameters $\left(B = 0.0078, N = 256\right)$ are generated and the magnitudes of DPS expansion coefficients are compared to suggested approximate the bound as shown in Fig. 22.

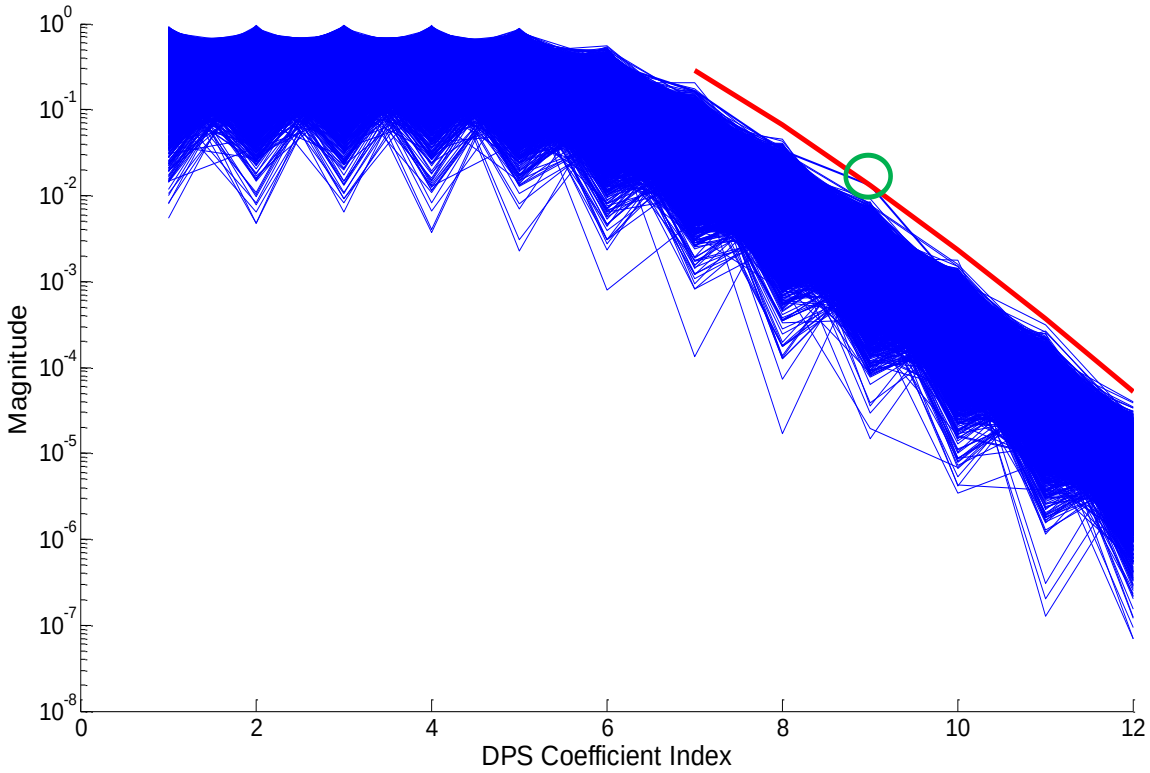

Figure 24: Magnitude of DPS Coefficients compared to Upper Bound

As illustrated in Fig. 24, the magnitudes of the realization coefficients generally fall below the bound except for a single realization indicated by the green circle, which could be explained by the guessed substitution of (3.11) in (3.17). The cutoff coefficient index was chosen to be 6.

3.2.2 Channel Estimation using Pilot Restoration for Frequency Invariant Channels

For the frequency invariant channel, as given by (3.3), the received vector in the time domain before receiver processing is given by:

$$\mathbf{r} = \mathbf{D}(\mathbf{h})\mathbf{F}^{H}\mathbf{x}_{\mathbf{f}} + \mathbf{F}\mathbf{n} \tag{0.90}$$

Due to the diagonal structure of the time domain channel, the zero forcing equalizing matrix is also diagonal corresponding to a time domain window vector $\mathbf{W}$. Ignoring the contribution of the noise, when the correct window $\mathbf{D}(\mathbf{w}^{*}) = \mathbf{D}(\mathbf{h})^{-1}$ is applied to the received vector and then processed by the FFT, ICI is completely eliminated and the pilot tones are restored satisfying the following relationship:

$$\mathbf{z}_{\mathbf{w}}^{(\mathcal{G})} = \mathbf{F}^{(\mathcal{G})}\mathbf{D}(\mathbf{w})\mathbf{r} = \mathbf{e}_{p}^{(\mathcal{G})} \tag{0.91}$$

Rearranging variables gives a system of equations in $\mathbf{W}$:

$$\mathbf{F}^{(\mathcal{G})}\mathbf{D}(\mathbf{r})\mathbf{w} = \mathbf{e}_{p}^{(\mathcal{G})} \tag{0.92}$$

However, this system of equations is underdetermined, $|\mathcal{G}| < N$, with the desired solution $\mathbf{w}^{*}$, being one amongst many. The correct inverse window that matches the channel has the following DPS representation:

$$\mathbf{w} = \mathbf{D}\left(\left(\mathbf{D}\left(\mathbf{S}_{\mathbf{p}}\boldsymbol{\alpha}\right)\right)^{-1}\right) \tag{0.93}$$

In (3.25) the $\mathbf{D}(.)$ operates on a vector, first converting into a matrix, and then on the inverse matrix extracting its diagonal into a vector.

Substituting (3.25) into (3.24) gives the following system of equations:

$$\mathbf{F}^{(\mathcal{G})}\mathbf{D}(\mathbf{r})\mathbf{D}\left(\left(\mathbf{D}\left(\mathbf{S}_{\mathbf{p}}\boldsymbol{\alpha}\right)\right)^{-1}\right) = \mathbf{e}_{p}^{(\mathcal{G})} \tag{0.94}$$

Although the dimensionality of the solution space has been greatly reduced, as $D \le |\mathcal{G}| \le N$, apart from the difficulty of solving such a system of non-linear equations, unlike in the case of linear systems the given condition is not sufficient for a unique solution.

Therefore, a more tractable approach is to cast the system of equations in (3.26) into a constrained optimization form with the objective of minimizing the square of the error norm between the r.h.s and l.h.s, which yields:

$$\boldsymbol{\alpha}^* = \arg\min_{\boldsymbol{\alpha}} \left\| \mathbf{F}^{(\mathcal{G})} \mathbf{D}(\mathbf{r}) \mathbf{D}\left(\left(\mathbf{D}\left(\mathbf{S}_{\mathbf{p}} \boldsymbol{\alpha} \right) \right)^{-1} \right) - \mathbf{e}_p^{(\mathcal{G})} \right\|_2^2, \boldsymbol{\alpha}^{(0)} = \boldsymbol{\alpha}_{LS} \tag{0.95}$$

subject to the following constraints,

$$\begin{aligned} \|\boldsymbol{\alpha}\|_2^2 &= E \\ |\alpha(e)| &\le \sqrt{E} \\ &\text{for i=1 to } N_e \\ |\alpha(e+i)| &\le \sqrt{\frac{\lambda^{e+i}}{\lambda^e}} \sqrt{E} \end{aligned} \tag{0.96}$$

The LS estimate of the DPS coefficient vector, $\boldsymbol{\alpha}_{LS}$, is used as the initial point for the optimization. The equality constraint is based on the assumption that the energy of a channel realization sequence is accessible in practice and can be obtained from Received Signal Strength (RSS) measurements. The inequality constraints are based on the approximate edge coefficient bounds given by (3.21) where the approximate cutoff coefficient bound is used $|\hat{\alpha}(e)| = \sqrt{E}$. The cutoff coefficient index is chosen to be $N_e = 2NB + 2$.

3.2.2.1 Simulation Results

Using simulations, the performance of the optimal window pilot restoration method and the standard LS method are compared in terms of channel estimation error and symbol error rate (SER) over a range of SNR values, $[0 - 50\text{dB}]$. The simulation is based on an

OFDM signal operating with parameters that are projected to be used in high mobility applications within the short term future, such as $f_c = 60\text{GHz}$ and $v_{\max} = 24m/s$ in vehicle to vehicle communications [17]. At the high frequency, the transmit and receive antennas can achieve highly directional beam patterns which contribute to limiting the number of arriving signal paths, thereby limiting the delay spread. Thus, the single tap non-frequency selective model can be considered a good approximation. A Doppler multiplication parameter *M* accounts for the chain bouncing of the signal off multiple moving objects.

System Parameters

- Modulation: QPSK
- Number of subcarriers $N = 1024$
- Carrier Frequency $f_c = 60\text{GHz}$
- Max Speed $v_{\max} = 24m/s$
- Doppler Multiplication $M = 2$
- Bandwidth $BW = 5MHz$

The maximum number of cycles completed by the channel time variation over a symbol period is given by:

$$Max\ number\ of\ \ cycles\ per\ symbol\ \ = \ \ \frac{f_c v_{\max}}{BWc_0} MN = 1.9661$$

This considerable number of cycles demands ***per-symbol window optimization*** where the optimization problem described by (3.27) & (3.28) is solved on a per-symbol basis.

The size of the DPS coefficient vector used to represent the channel is $D = 9$ and the cutoff coefficient is chosen to be $e = 6$.

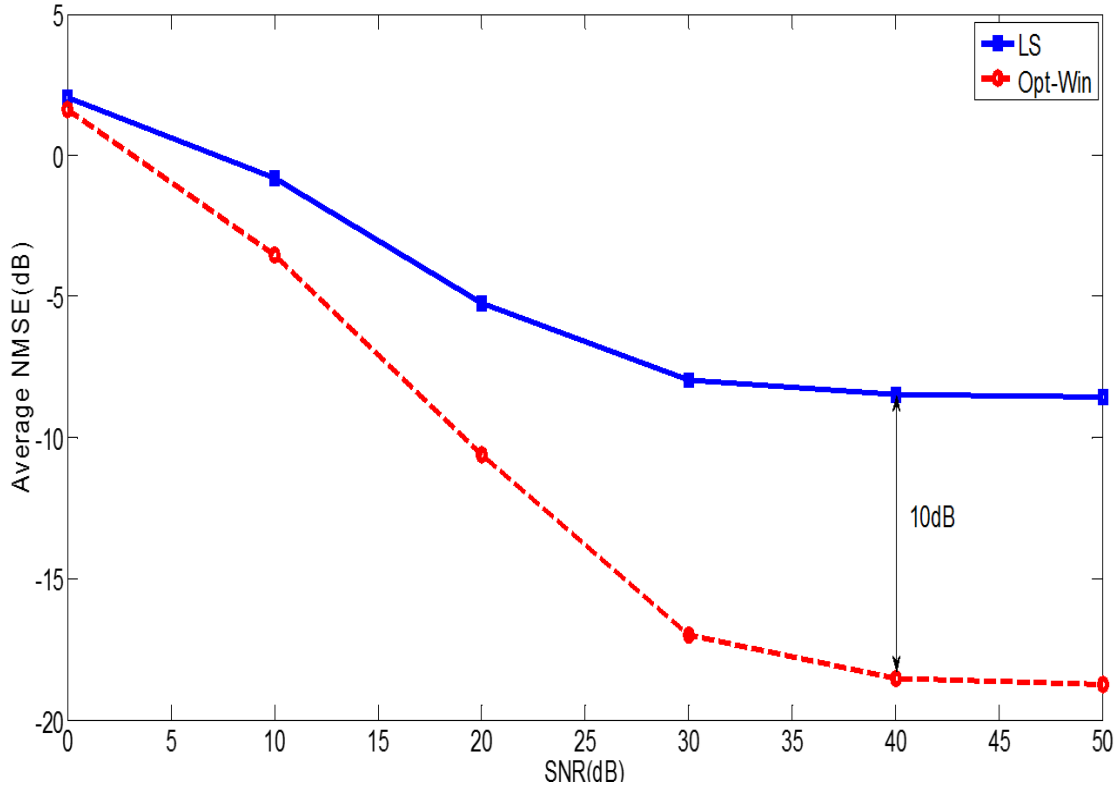

Figure 25: Channel Estimation Error

In Fig. 25 the channel estimation performance shown was generated by averaging over 100 unit-energy channel and symbol realizations, each channel realization acting on a corresponding symbol. At high SNR, the LS channel estimation error exhibits an error floor due to the contamination of the pilots by ICI. The error of the optimized window method is better by $\approx 10\text{dB}$ yet also exhibits an error floor. This error floor is due to isolated cases where the optimization function converges to local minima resulting in a high error which then dominates the majority of low error cases, biasing the overall average. For LS, the error is worse across realizations.

At low SNR the improvement gap narrows. This can be explained by analyzing the effect of noise on the time domain received vector $\mathbf{r}$.

Revisiting (3.22), left-multiplying by $\mathbf{F}^{(\mathcal{G})}\mathbf{D}(\mathbf{w})$, and tracking the effect of noise, yields:

$$\begin{aligned}\mathbf{F}^{(\mathcal{G})}\mathbf{D}(\mathbf{w})\mathbf{r} &= \mathbf{F}^{(\mathcal{G})}\mathbf{D}(\mathbf{w})\mathbf{D}(\mathbf{h})\mathbf{F}^{H}\mathbf{x}_{\mathbf{f}} + \mathbf{F}^{(\mathcal{G})}\mathbf{D}(\mathbf{w})\mathbf{n} \\ &= \mathbf{F}^{(\mathcal{G})}\mathbf{D}(\mathbf{w})\mathbf{D}(\mathbf{h})\mathbf{F}^{H}\mathbf{x}_{\mathbf{f}} + \mathbf{F}^{(\mathcal{G})}\mathbf{D}(\mathbf{w})\mathbf{D}(\mathbf{h})\mathbf{D}(\mathbf{h})^{-1}\mathbf{n} \\ &= \mathbf{F}^{(\mathcal{G})}\mathbf{D}(\mathbf{w})\mathbf{D}(\mathbf{h})\mathbf{F}^{H}\left[\mathbf{x}_{\mathbf{f}} + \mathbf{F}\mathbf{D}(\mathbf{h})^{-1}\mathbf{n}\right]\end{aligned} \tag{0.97}$$

By the orthogonality and completeness of $\mathbf{F}$, $\mathbf{n}$ can be replaced by $\mathbf{F}^{H}\tilde{\mathbf{n}}$, and $\tilde{\mathbf{n}}$ remains circularly complex Gaussian, so that:

$$\mathbf{F}^{(\mathcal{G})}\mathbf{D}(\mathbf{w})\mathbf{r} = \mathbf{F}^{(\mathcal{G})}\mathbf{D}(\mathbf{w})\mathbf{D}(\mathbf{h})\mathbf{F}^{H}\left[\mathbf{x}_{\mathrm{f}} + \mathbf{F}\mathbf{D}(h)^{-1}\mathbf{F}^{H}\tilde{\mathbf{n}}\right] \tag{0.98}$$

Now the correct window should restore the observation tones to the value $\left(\mathbf{x}_{\mathrm{f}} + \mathbf{F}\mathbf{D}(\mathbf{h})^{-1}\mathbf{F}^{H}\tilde{\mathbf{n}}\right)^{(\mathcal{G})}$ and not to $\mathbf{e}_{p}^{(\mathcal{G})}$, thus the optimization solver will be targeting an optimization criterion that is offset from the correct one.

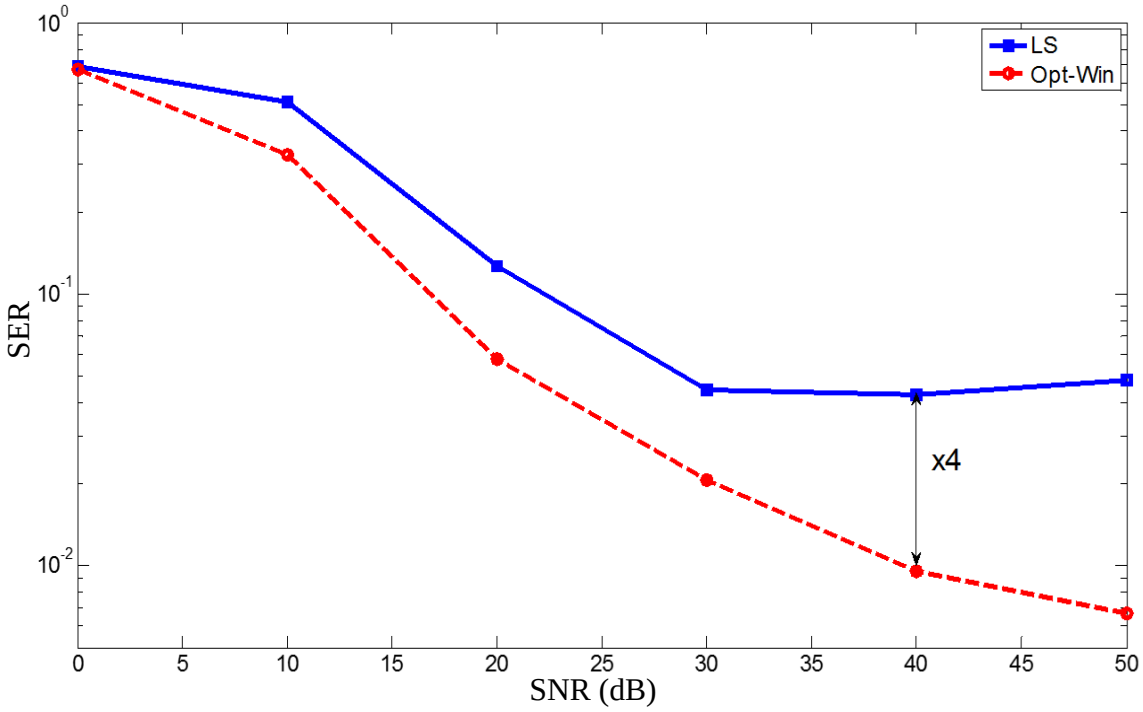

Figure 26: Symbol Error Rate

The second metric of comparison is SER which is illustrated in Fig. 26. The improvement gap between Opt-win and LS is slightly less than that of the channel estimation error with a 4-fold reduction in SER corresponding to the 10dB channel estimation error improvement

at 40dB SNR. This is well known behavior for SER versus ICI which depends on the modulation order. SER becomes more sensitive to ICI for higher order modulation schemes wherein a greater SER performance can be realized by the Opt-win method.

3.3 Channel Model for Doubly Dispersive (Frequency-variant) Channels with Fractional Delay Taps

A common matrix representation for doubly dispersive channels is based on the discrete integer tap model [18],[12]. This model assumes delay taps to be integer multiples of the sampling period, which is not necessarily the case in practice. In the presence of fractional delay taps, the leakage phenomenon comes into play and the time domain channel matrix is no longer strictly banded and instead is diagonally decaying.

To derive the more generalized frequency domain channel matrix based on a ***discrete fractional tap model*** we have to start from the continuous time TV channel impulse response for a specular multipath model:

$$\begin{aligned} h(t,\tau) &= \sum_{l=0}^{L-1} a_l e^{j2\pi f_l t}\delta(\tau-\tau_l) \\ &= \sum_{l=0}^{L-1} \beta_l(t)\delta(\tau-\tau_l) \end{aligned} \tag{0.99}$$

Given a max delay spread $\tau_{L-1}=\tau_{max}$ and an OFDM symbol input consisting of N subcarriers, the output over the duration $0\le t\le T$ and after removing the cyclic prefix is given by:

$$\begin{aligned} y(t) &= \int_0^{\tau_{max}} \sum_{l=0}^{L-1} \beta_l(t)\delta(\tau-\tau_l)\sum_{k=0}^{N-1} X_k e^{j\frac{2\pi k}{T}(t-\tau)}\,d\tau \\ &= \sum_{k=0}^{N-1}\sum_{l=0}^{L-1} \beta_l(t) e^{-j\frac{2\pi k\tau_l}{T}} e^{j\frac{2\pi kt}{T}} X_k \end{aligned} \tag{0.100}$$

Sampling the output in time, at $t=nT_s$ where $T=NT_s$:

$$y(nT_s) = \sum_{k=0}^{N-1}\sum_{l=0}^{L-1} \beta_l(nT_s) e^{-j\frac{2\pi k\tau_l}{T}} e^{j\frac{2\pi kn}{N}} X_k \tag{0.101}$$

Applying the DFT to the output signal yields:

$$Y_q = \sum_{n=0}^{N-1} e^{-j\frac{2\pi qn}{N}} \sum_{k=0}^{N-1}\sum_{l=0}^{L-1} \beta_l(nT_s) e^{-j\frac{2\pi k\tau_l}{T}} e^{j\frac{2\pi kn}{N}} X_k \ \ for\, q \in [0, N-1] \tag{0.102}$$

Rewriting in matrix form gives:

$$\mathbf{y_f} = \mathbf{F}\left(\bar{\mathbf{H}} \circ \mathbf{F}^H\right)\mathbf{x_f} \tag{0.103}$$

where $\left[\bar{\mathbf{H}}\right]_{nk} = \sum_{l=0}^{L-1} \beta_l(nT_s) e^{-j\frac{2\pi k\tau_l}{T}}$, $\left[\mathbf{x_f}\right]_k = X_k$, $\left[\mathbf{y_f}\right]_q = Y_q$ and $\circ$ is the Hadamard product operation.

Hence the frequency domain channel matrix is given by:

$$\mathbf{H_f} = \mathbf{F}\left(\bar{\mathbf{H}} \circ \mathbf{F}^H\right) \tag{0.104}$$

Following the same procedure as in Section 3.2 to get the LS estimation equations, the time varying transfer function can be expressed as:

$$\bar{\mathbf{H}} = \mathbf{B}\boldsymbol{\Lambda}^H \tag{0.105}$$

where $\left[\mathbf{B}\right]_{nl} = \beta_l[n]$ and $\left[\boldsymbol{\Lambda}\right]_{kl} = e^{j\frac{2\pi k\tau_l}{T}}$ are $N \times L$ matrices.

The time varying factor $\beta_l[n]$ for each delay tap will be expressed in terms of its DPS expansion with dimension D:

$$\boldsymbol{\beta}_\mathbf{l} = \mathbf{S_p}\boldsymbol{\alpha}_\mathbf{l} \tag{0.106}$$

where $\left[\boldsymbol{\beta}_\mathbf{l}\right]_n = \beta_l[n]$, $\boldsymbol{\alpha}_l = \left[\alpha_l(0), ..., \alpha_l(D-1)\right]^T$ and $\mathbf{S_p} = \left[\mathbf{s}_0, ..., \mathbf{s}_{D-1}\right]$. Combining all $\boldsymbol{\alpha}_l$ vectors (as columns) in a single matrix and substituting in (3.37) :

$$\bar{\mathbf{H}} = \mathbf{S_p} \mathbf{A} \boldsymbol{\Lambda}^H \tag{0.107}$$

where $\mathbf{A} = \left[\boldsymbol{\alpha}_0, ..., \boldsymbol{\alpha}_{L-1}\right]$. The frequency domain channel matrix becomes:

$$\mathbf{H_f} = \mathbf{F}\left(\mathbf{S_p} \mathbf{A} \boldsymbol{\Lambda}^H \circ \mathbf{F}^H\right) \tag{0.108}$$

The matrix $\mathbf{A}$ consists of the unknown coefficients that need to be estimated. Equation (3.35) becomes:

$$\begin{aligned} \mathbf{y_f} &= \boldsymbol{\Gamma}\left(\bar{\boldsymbol{\alpha}} \otimes \mathbf{I}_N\right)\mathbf{x_f} + \mathbf{n} \\ &= \boldsymbol{\Gamma}\left(\mathbf{I}_{DL} \otimes \mathbf{x_f}\right)\bar{\boldsymbol{\alpha}} + \mathbf{n} \end{aligned} \tag{0.109}$$

where $\bar{\boldsymbol{\alpha}} = \left[\boldsymbol{\alpha}_0^T, \ldots, \boldsymbol{\alpha}_{L-1}^T\right]^T$, $\boldsymbol{\Gamma} = \left[\boldsymbol{\Gamma}_{0,0}, \ldots, \boldsymbol{\Gamma}_{0,D-1}, \ldots, \ldots, \boldsymbol{\Gamma}_{L-1,0}, \ldots, \boldsymbol{\Gamma}_{L-1,D-1}\right]$, $\boldsymbol{\Gamma}_{d,l} = \mathbf{F}\left(\mathbf{s_d} \boldsymbol{\lambda}_\mathbf{l}^H \circ \mathbf{F}^H\right)$ and $\boldsymbol{\lambda}_\mathbf{l}$ is the l-th column of $\boldsymbol{\Lambda}$.

Substituting for $\mathbf{x_f}$ using the orthogonal data and pilot vector components and taking the output observation samples corresponding to the pilot locations defined in the observation set $\mathcal{O}$ yields

$$\mathbf{y}_\mathbf{f}^{(\mathcal{O})} = \boldsymbol{\psi}_\mathbf{p}^{(\mathcal{O})} \bar{\boldsymbol{\alpha}} + \boldsymbol{\psi}_\mathbf{d}^{(\mathcal{O})} \bar{\boldsymbol{\alpha}} + \mathbf{n}^{(\mathcal{O})} \tag{0.110}$$

The LS estimate is given by:

$$\hat{\bar{\boldsymbol{\theta}}} = \left(\boldsymbol{\psi}_\mathbf{p}^{(\mathcal{O})}\right)^\dagger \mathbf{y}_\mathbf{f}{}^{(\mathcal{O})} \tag{0.111}$$

3.3.1 Channel Estimation using Pilot Restoration for DD Channels

Unlike the single tap frequency-invariant case a time domain window cannot be used for equalizing the channel effects. Thus, there is no advantage gained from doing the equalization in the time domain. Instead a frequency domain equalization matrix that attempts to restore the pilot will be used.

Starting from the frequency domain input-output relationship without the noise component:

$$\mathbf{y_f} = \mathbf{H_f x_f} \tag{0.112}$$

The equalization matrix $\mathbf{B}^*$ exists in the space of matrices $\mathbf{B}$ which have inverses of the following form:

$$\mathbf{B}^{-1} = \mathbf{F}\left(\mathbf{S_p A \Lambda}^H \circ \mathbf{F}^H\right) \tag{0.113}$$

and satisfy the pilot restoration condition:

$$\left(\mathbf{B y_f}\right)^{(\mathcal{P})} = \mathbf{p}^{(\mathcal{P})} \tag{0.114}$$

where $\mathcal{P}$ is the set of indices of pilot clusters.

3.3.1.1 Per-tap equality and inequality constraints

Given that there are multiple paths/taps, a per tap energy constraint can be obtained using the assumption that the tap energies follow an exponential decay where the energy of the l^{th} path is given by:

$$E_l = \frac{exp\left(-\frac{T_l}{\tau_{rms}}\right)}{\sum_{k=0}^{L-1} exp\left(-\frac{T_k}{\tau_{rms}}\right)} E \tag{0.115}$$

where τ_{rms} is the rms delay spread and T_l is the delay of the l-th path in units of seconds respectively. Also $\sum_l E_l = \left\|\mathbf{H}_f\right\|_F^2 = E$, where $\left\|(.)\right\|_F$ is the Frobenius norm.

Similarly the exponential decay profile can be incorporated to obtain per tap upper bound inequality constraints on the magnitude of the DPS coefficients:

$$\left|\alpha_l\left(e+i\right)\right| \le \sqrt{\frac{\lambda^{(e+i)}}{\lambda^{(e)}}}\sqrt{E_l} \quad for\, i \ge 0,1,..\ and\ \ l \ge 0,1,\ldots,L-1 \tag{0.116}$$

The cut-off index e is the same for all taps since they all have the same dimensionality of time variation.

Finally the pilot restoration optimization problem is formulated as follows:

$$\bar{\boldsymbol{\alpha}}^{*} = \arg\min_{\bar{\boldsymbol{\alpha}}} \left\| (\mathbf{B}^{-1}(\bar{\boldsymbol{\alpha}})\mathbf{y}_{\mathrm{f}})^{(\mathcal{P})} - \mathbf{p}^{(\mathcal{P})} \right\|_2^2, \bar{\boldsymbol{\alpha}}^{(0)} = \bar{\boldsymbol{\alpha}}_{LS} \tag{0.117}$$

subject to the following constraints, for $l = 0,\ldots,L-1$:

$$\begin{aligned} \left\|\boldsymbol{\alpha}_l\right\|_2^2 &= E_l \\ \left|\alpha_l(e)\right| &\le \sqrt{E_l} \\ \left|\alpha_l(e+i)\right| &\le \sqrt{\frac{\lambda^{e+i}}{\lambda^{e}}}\sqrt{E_l}, \text{ for } i\text{=1 to } N_e \end{aligned} \tag{0.118}$$

3.3.1.2 Simulation Results

Performance is evaluated for the LS and Pilot Restoration (PR) methods, in terms of channel estimation error and symbol error rate, with each method operating on the same set of symbols. The parameters used for the simulations (normalized with respect to sample rate) are:

- Normalized Doppler $f_d = 0.0019$
- Samples per symbol $N = 1024$
- DPS coefficients per path $D = 9$
- RMS delay spread $\tau_{rms} = 4.4\mu s$
- Number of paths $L = 2$
- Size of pilot cluster zero guard $g = 6$
- Modulation : QPSK
- Index of edge coefficient $e = 6$

The two paths are modeled as two independent processes with power determined according to an exponential power delay profile (PDP) and time variation generated based on the Rayleigh fading model given in [19]. In Fig. 27, the channel estimation error is plotted for

100 OFDM symbols arranged along the x-axis in ascending order of Channel Estimation Error (CEE) showing a progression from low CEE symbols on the left to high CEE symbols on the right.

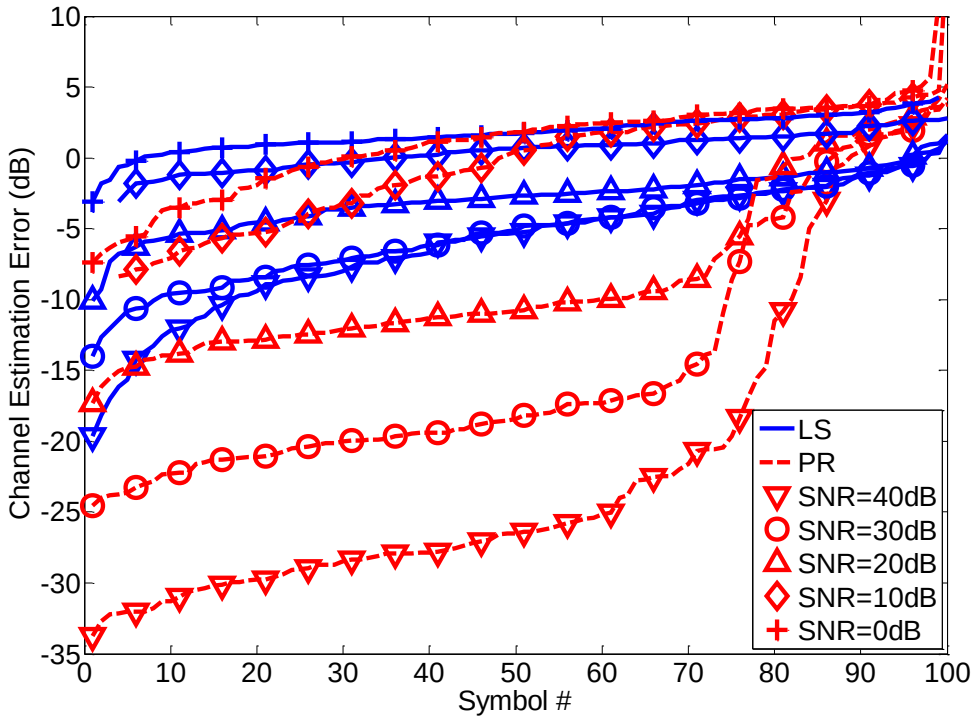

Figure 27: Channel Estimation Error Performance

A significantly larger percentage of symbols has a much lower CEE for the PR method than for the LS method at a given SNR. However, for a small number of symbols on the extreme right, the PR method has a higher CEE than in the LS case. Due to this peculiar distribution, the average CEE over all 100 symbols would be a misleading performance indicator, as such an evaluation shows a factor of 2.5 in CEE reduction at 40dB (for PR relative to LS). For low SNR values, 0 and 10dB, the performance improvement is diminished for the same reason as in the frequency invariant channel case, which is the misalignment between the optimization criterion of pilot restoration and the true criterion of equalization.

Figure 28 shows a similar ascending order arrangement as was used in Fig. 27, but this time with SER for each symbol as the metric for performance comparison.

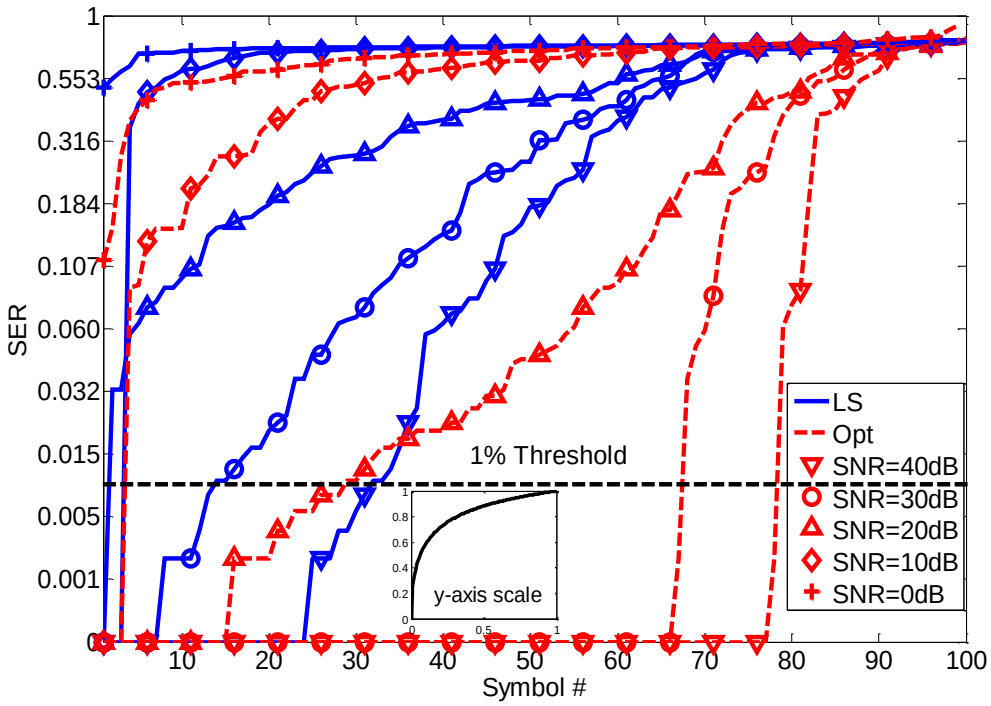

Figure 28: Symbol Error Rate Performance

A similar performance pattern is observed where the PR method yields a significantly larger percentage of symbols with SER less than 10^{-2} than LS and a smaller percentage of symbols where the situation is the opposite. In practice, a threshold effect comes into play where symbols with SER above a certain limit are not very useful, as such symbols no longer benefit from symbol coding. A typical threshold is 1% as represented by the dashed line in Fig. 28. To emphasize this region of most interest (below the threshold) more, a nonlinear transformation was applied to SER.

For 40 dB SNR there are 78 out of 100 symbols without error for PR, while for LS that number is 33 out of 100. The biggest improvement occurs for 20 dB SNR, where the number increased from 3 to 30 out of 100. A marked improvement (by a factor of 2 to 10) in the number of symbols recovered with SER < 10^{-2} is observed as SNR varies from 40 dB down to 20 dB. For the below SER threshold symbols, modest coding can reduce SER by several orders of magnitude.

3.4 2-D DPS BEM Decomposition of Time-Varying Transfer Function

For Doppler and delay spread components within the range $[-\upsilon_{\max},\upsilon_{\max}]\times[0,\tau_{\max}]$, the right and left DFT bases used in the time-varying transfer function form given by (2.58), Chapter 2 can be replaced by DPS bases parameterized by $\upsilon_{\max}$ and $\tau_{\max}$ respectively.

$$\boldsymbol{H} = \mathbf{S}_{\upsilon}\boldsymbol{\Gamma}\mathbf{S}_{\tau} \tag{0.119}$$

where

$\boldsymbol{H}$ is the time-varying transfer function form of the channel

$\mathbf{S}_{\upsilon} = [\mathbf{s}_{\upsilon 1},...,\mathbf{s}_{\upsilon q}]$ is the left DPS basis with dimension $q = f\left(2\upsilon_{\max}N\right)$

$\mathbf{S}_{\tau} = [\mathbf{s}_{\tau 1},...,\mathbf{s}_{\tau p}]$ is the right DPS basis with dimension $p = f\left(\tau_{\max}N\right)$

$\boldsymbol{\Gamma}$ is the coefficient matrix of size $q \times p$

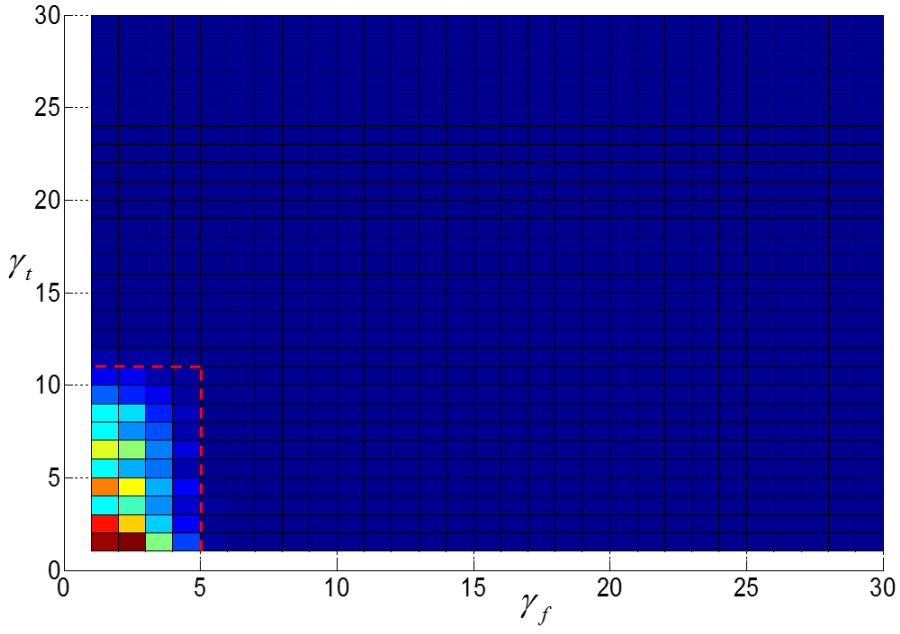

Figure 29: Elements of Coefficient Matrix $\boldsymbol{\Gamma}$ for 2-D DPS BEM Concentrated Within a Rectangular Region Outlined by the Red Dashed Line

For a time-varying channel with parameters $\tau_{\max} = 1$ and $f_{\max} = 4$ the elements of the coefficient matrix are shown in Fig. 29. The significant coefficients are concentrated in a small region bounded by the red rectangle.

To exploit the compact support of the channel, the transmit information should be encoded in frequency, e.g. OFDM, and equalization processing should be done in the time domain. As a result, the input-output relationship is given by:

$$\begin{aligned} \mathbf{y} &= \mathbf{H}_{\mathbf{tf}}\mathbf{x} \\ &= \left(\boldsymbol{H} \circ \mathbf{F}^{H}\right)\mathbf{x} \end{aligned} \tag{3.53}$$

The Hadamard product, denoted by $\circ$ between $\mathbf{F}$ and the time varying transfer function $\boldsymbol{H}$ in (3.53) are necessary in order to obtain a form that can operate on an input vector $\mathbf{x}$ in time or in frequency. However, the Hadamard operator represents an obstacle that prevents the use of subspace methods since it violates the rank boundedness property of matrix products where:

$$\begin{aligned} &\mathbf{rank}\left(\mathbf{AB}\right) < \min\left(\mathbf{rank}\left(\mathbf{A}\right), \mathbf{rank}\left(\mathbf{B}\right)\right) \\ &\mathbf{rank}\left(\mathbf{A} \circ \mathbf{B}\right) \not< \min\left(\mathbf{rank}\left(\mathbf{A}\right), \mathbf{rank}\left(\mathbf{B}\right)\right) \end{aligned} \tag{3.54}$$

Algebraically manipulating (3.53) gives the following form that is free from the Hadamard product:

$$\begin{aligned} \mathbf{y} &= \mathbf{H}_{\mathbf{tf}}\mathbf{x} \\ &= \left(\mathbf{S}_{\upsilon}\boldsymbol{\Gamma}\mathbf{S}_{\tau} \circ \mathbf{F}^{H}\right)\mathbf{x} \\ &= \sum_{i=1,\, j=1}^{q,p} \gamma_{ij}\left(\mathbf{s}_{\upsilon i}\mathbf{s}_{\tau i}^{H} \circ \mathbf{F}^{H}\right)\mathbf{x} \\ &= \sum_{i=1,\, j=1}^{q,p} \gamma_{ij}\mathbf{D}\left(\mathbf{s}_{\upsilon i}\right)\mathbf{F}^{H}\mathbf{D}\left(\mathbf{s}_{\tau i}^{H}\right)\mathbf{x} \end{aligned} \tag{3.55}$$

where $\mathbf{D}(.)$ converts a vector into a diagonal matrix.

Thus, $\mathbf{H}_{\mathbf{tf}}$ can be written in factored form as:

$$\mathbf{H_{tf}} = \hat{\mathbf{S}}_{\upsilon}\left(\mathbf{\Gamma} \otimes \mathbf{F}\right)\hat{\mathbf{S}}_{\tau}^{H} \tag{3.56}$$

with Kronecker product $\otimes$, $\hat{\mathbf{S}}_{\upsilon} = \left[\mathbf{D}(\mathbf{s}_{\upsilon i}),...,\mathbf{D}\left(\mathbf{s}_{\upsilon q}\right)\right]$, and $\hat{\mathbf{S}}_{\tau} = \left[\mathbf{D}(\mathbf{s}_{\tau i}),...,\mathbf{D}\left(\mathbf{s}_{\tau p}\right)\right]$.

3.4.1 Block repetition Semi-blind channel Estimation

Blind channel estimation techniques exploit the static structure, if any, in the channel across multiple observations to infer the noise subspace, which is then used to solve for the channel coefficients.

Given an input-output system relation $\mathbf{y} = \mathbf{Hx}$, if the channel $\mathbf{H}$ is constant for K consecutive observations, the channel matrix $\mathbf{H}$ can be obtained by solving the concatenated set of equations:

$$\mathbf{Y} = \mathbf{HX} \tag{3.57}$$

where $\mathbf{X} = [\mathbf{x}_1,...,\mathbf{x}_K]$, and $\mathbf{Y} = [\mathbf{y}_1,...,\mathbf{y}_K]$.

Examining the factored structure of (3.56) shows that the subspace techniques could be applied, as in [20], were it not for the left factor $\hat{\mathbf{S}}_{\upsilon}$. Due to the static portion of the channel (the channel coefficient matrix $\mathbf{\Gamma}$) being surrounded by both left and right matrix factors the situation becomes more complicated than that in [20].

In order to eliminate the factor $\hat{\mathbf{S}}_{\upsilon}$, the transmitted symbol vector is consecutively repeated q times as shown in Fig. 29.

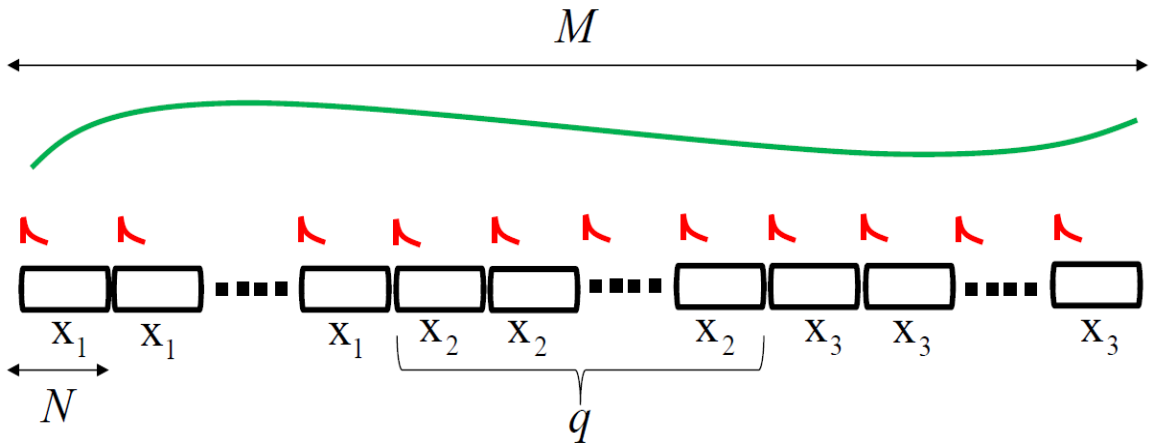

Figure 30: Block Repetition by q (the dimensionality of time variation). Time Variation over Frame (shown in green) and Delay Spread (shown in red) have constant BEM Coefficients across the Frame Length.

As a result the input-output relationship in (3.53) takes the following form:

$$\bar{\mathbf{y}} = \bar{\mathbf{H}}_{\mathbf{tf}}\mathbf{x} \tag{3.58}$$

where $\bar{\mathbf{y}} = \left[\mathbf{y}^{(1)T},...,\mathbf{y}^{(q)T}\right]^T$ and the superscripts denote the symbol index. Assuming the DPS basis $\hat{\mathbf{S}}_\upsilon$ is parameterized the duration of the entire frame of length $M = ON$, where a frame consists of O consecutive blocks and N is the number of samples per block, $\bar{\mathbf{H}}_{\mathbf{tf}}$ is given by:

$$\bar{\mathbf{H}}_{\mathbf{tf}} = \hat{\mathbf{S}}_\upsilon^{(R)}\left(\mathbf{\Gamma}\otimes\mathbf{F}\right)\hat{\mathbf{S}}_\tau^H \tag{3.59}$$

where $\hat{\mathbf{S}}_\upsilon^{(R)} = \left[\hat{\mathbf{S}}_\upsilon^{(r1)H},...,\hat{\mathbf{S}}_\upsilon^{(rq)H}\right]^H$ for $r_i \in R$, where R is the set of locations across which the blocks are repeated.

The matrix $\hat{\mathbf{S}}_\upsilon^{(R)}$ is square and can be inverted when the right rank conditions are satisfied which are determined by the choice of the locations in the set R.

Substituting (3.59) into (2.58) yields:

$$\bar{\mathbf{y}} = \hat{\mathbf{S}}_\upsilon^{(R)}\left(\mathbf{\Gamma}\otimes\mathbf{F}\right)\hat{\mathbf{S}}_\tau^H\mathbf{x} \tag{3.60}$$

Assuming $\hat{\mathbf{S}}_{\upsilon}^{(R)-1}$ exists:

$$\hat{\mathbf{S}}_{\upsilon}^{(R)-1}\overline{\mathbf{y}} = \left(\boldsymbol{\Gamma}\otimes\mathbf{F}\right)\tilde{\mathbf{x}} \tag{3.61}$$

where $\tilde{\mathbf{x}} = \hat{\mathbf{S}}_{\tau}^{H}\mathbf{x}$, which is a modulated version of the input vector.

Applying a block IDFT operation gives:

$$\underbrace{\left(\mathbf{I}_q\otimes\mathbf{F}^H\right)\hat{\mathbf{S}}_{\upsilon}^{(R)-1}\overline{\mathbf{y}}}_{\mathbf{v}} = \left(\boldsymbol{\Gamma}\otimes\mathbf{I}_N\right)\tilde{\mathbf{x}} \tag{3.62}$$

For simplification the left hand side vector will henceforth be denoted by the symbol $\mathbf{v}$.

Uniformly sampling $\mathbf{v}$ to split it into *N* phases which are placed as columns in the matrix $\underline{\mathbf{V}}$ such that $\underline{\mathbf{V}} = \left[\mathbf{v}_1,...,\mathbf{v}_N\right]$ and $\left\{\mathbf{v}_i\right\}_j = \mathbf{v}\left(jN+i\right)$ for $i = 0,...,N-1,\ j = 1,...,q$. Equation (3.62) can be written as:

$$\underset{q\times N}{\underline{\mathbf{V}}} = \underset{q\times p}{\boldsymbol{\Gamma}}\ \underset{p\times N}{\hat{\mathbf{S}}_{\tau}^{H}}\ \underset{N\times N}{\mathbf{D}\left(\mathbf{x}\right)} \tag{3.63}$$

Now (3.63) is in a form that is amenable to finding the noise subspace. In order for a noise subspace to exist, the matrix must be tall, i.e. $q > p$, so that the frequency dispersion in the channel is higher than the time dispersion.

Applying a SVD decomposition to $\underline{\mathbf{V}}$:

$$\underline{\mathbf{V}} = \left[\mathbf{U}_s\ \mathbf{U}_n\right]\begin{bmatrix}\Sigma & \mathbf{0}\\ \mathbf{0} & \mathbf{0}\end{bmatrix}\begin{bmatrix}\mathbf{V}_s^H\\ \mathbf{V}_n^H\end{bmatrix} \tag{3.64}$$

where $\mathbf{U}_s$ and $\mathbf{U}_n$ are the range and noise subspace bases respectively. Since $\boldsymbol{\Gamma}$ is in the range space we have the equality:

$$\boldsymbol{\Gamma} = \mathbf{U}_s\mathbf{T} \tag{3.65}$$

where $\mathbf{T}$ is a $p \times p$ invertible matrix.

Multiplying both sides of (3.63) by $\mathbf{U}_s^H$:

$$\underset{\mathbf{\Lambda}}{\mathbf{U}_s^H \underline{\mathbf{V}}} = \mathbf{T}\hat{\mathbf{S}}_\tau^H \mathbf{D}(\mathbf{x}) \tag{3.66}$$

To find $\underset{p\times p}{\mathbf{G}} = \mathbf{T}^{-1}$, we have the following set of equations:

$$\mathbf{G}\boldsymbol{\lambda}_n = \begin{bmatrix} \mathbf{g}_1^H \\ \vdots \\ \mathbf{g}_p^H \end{bmatrix} \boldsymbol{\lambda}_n = \begin{bmatrix} x(n)\mathbf{S}_\tau(1,n) \\ \vdots \\ x(n)\mathbf{S}_\tau(p,n) \end{bmatrix} \quad for\ n = 1,...,N \tag{3.67}$$

where $\mathbf{G}^H = \left[\mathbf{g}_1,...,\mathbf{g}_p\right]$, $\mathbf{\Lambda} = \left[\boldsymbol{\lambda}_1,...,\boldsymbol{\lambda}_N\right]$

Rearranging, an overdetermined system of homogeneous equations can be obtained:

$$\frac{\mathbf{g}_j^H \boldsymbol{\lambda}_n}{\mathbf{S}_\tau(j,n)} - \frac{\mathbf{g}_k^H \boldsymbol{\lambda}_n}{\mathbf{S}_\tau(k,n)} = 0 \qquad for\ n = 1,...,N \quad j,k = 1,...,p\ \ j \neq k \tag{3.68}$$

Rearranging all (j,k) pairs for all values of n in a matrix $\mathbf{\Omega}$ gives:

$$\mathbf{\Omega}\bar{\mathbf{g}} = \mathbf{0} \tag{3.69}$$

where $\bar{\mathbf{g}} = \left[\mathbf{g}_1^H,...,\mathbf{g}_p^H\right]^H$, and

$$\mathbf{\Omega} = \begin{bmatrix} \mathbf{\Omega}_1 \\ \vdots \\ \mathbf{\Omega}_N \end{bmatrix} \quad , \quad \mathbf{\Omega}_n = \begin{bmatrix} \frac{\boldsymbol{\lambda}_n^H}{\mathbf{S}_\tau(1,n)} & \frac{\boldsymbol{\lambda}_n^H}{\mathbf{S}_\tau(2,n)} & \mathbf{0} & \cdots & \cdots \\ \frac{\boldsymbol{\lambda}_n^H}{\mathbf{S}_\tau(1,n)} & \mathbf{0} & \frac{\boldsymbol{\lambda}_n^H}{\mathbf{S}_\tau(3,n)} & \mathbf{0} & \cdots \\ \mathbf{0} & \frac{\boldsymbol{\lambda}_n^H}{\mathbf{S}_\tau(2,n)} & \frac{\boldsymbol{\lambda}_n^H}{\mathbf{S}_\tau(3,n)} & \mathbf{0} & \cdots \\ \vdots & \vdots & \vdots & \cdots & \vdots \end{bmatrix} \tag{3.70}$$

where $\mathbf{\Omega}$ has size $N\binom{p}{2}\times p^2$.

Since $N >> p$ the system of equation in (3.69) is overdetermined can be solved for $\bar{\mathbf{g}}$ from which $\mathbf{G}$ can be found. Using the knowledge of $\mathbf{U}_s^H$ and $\mathbf{G}\left(\mathbf{T}^{-1}\right)$, the coefficients matrix $\mathbf{\Gamma}$ can be found.

CHAPTER 4 SIGNALING WAVEFORM FRAMEWORKS: GABOR BASES, ONBs, AND CHANNEL ADAPTED SIGNALING

The challenge of communication lies in the ability to reliably transfer information across a medium that exhibits two forms of hostile behavior: additive noise and channel distortion. The effect of noise on communication capacity is quantified using Shannon's well known work [21] in coding theory which informs the design of protective measures against the effect of noise. Alternatively, the effect of noise can be proactively overcome by increasing the overall energy in the signal regardless of the waveform shape used.

On the other hand, waveform shape plays an important role in enhancing resilience to the channel distortion (delay spread and Doppler spread) and preserving the ***structure of encoded information***. Although receiver processing (equalization) is essential for reversing the distortion caused by the channel and recovering the signal, the cost of receiver processing as well as its efficacy is highly dependent on the degree to which the channel distortion destroys the structure of information encoded in the waveform. Thus, one criterion for selecting the waveform shape is to minimize the disruption of the structure of encoded information.

Waveform shapes used in communications belong to the category of functions that are members of $L^2(\mathbb{R})$, i.e. finite energy but not necessarily finite extent. Discrete units of information commonly referred to as symbols are mapped to a set of distinct signals having certain waveform shapes.

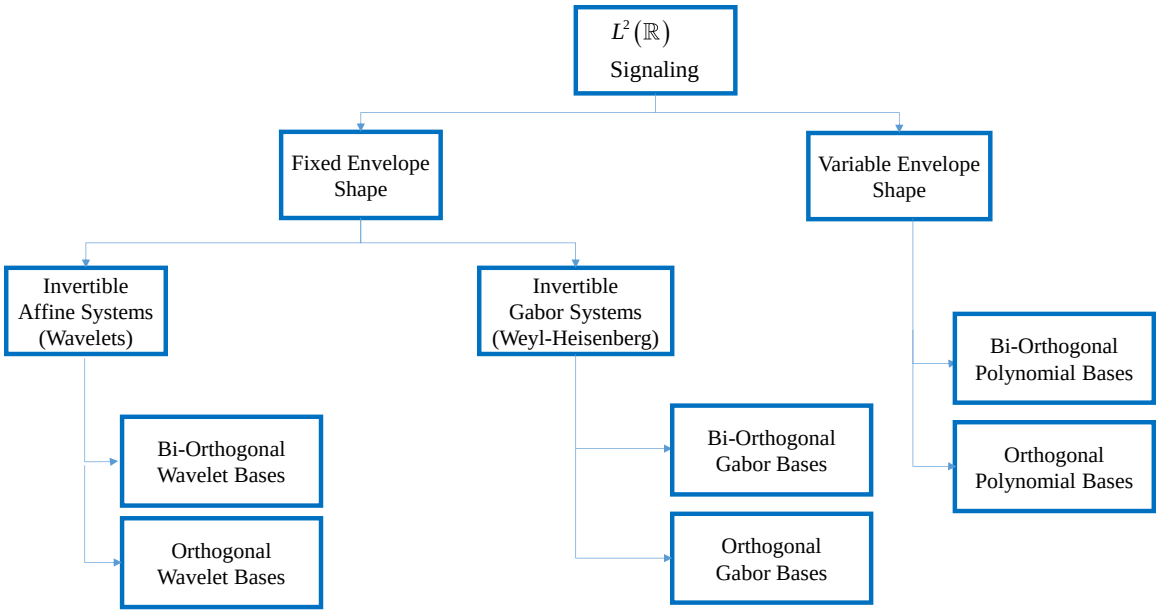

Figure 31: Classification of Signaling Waveforms used in Communications

The waveform shape determines: 1) the degree of distinction between signals, which is essential for the inverse mapping from signals to symbols, and 2) resilience to channel effects.

Existing signaling schemes can be divided into two categories:

1) Family of waveforms with fixed envelope shape:

This category consists of a set of waveforms that share the same complex envelope (waveforms can be complex functions) shape yet remain distinct. Sub-categories include:

Invertible Affine Systems (Wavelets):

The family $\{H_{mn}, a, b\}$ generated by affine transformations, time scale and time shift, of a prototype pulse shape $H(t)$ constitute a separable set of signaling waveforms for the appropriate choice of parameters a and b [22]:

$$H_{mn}(t) = a^{m/2} H\left(a^m t - nb\right) \tag{0.120}$$

Bi-orthogonal wavelets and Orthogonal wavelets constitute the class of Invertible Affine Systems.

Gabor Systems (Weyl-Heisenberg):

The majority of signaling waveforms used in modern communications consist of time-frequency shifted versions of a prototype pulse shape $G(t)$ which places them in the category of Gabor Systems $\{G_{mn}, a, b\}$ where:

$$G_{mn}(t) = e^{2\pi i m/b} G(t - nb) \tag{0.121}$$

Invertible Gabor systems are generated when parameters a, b satisfy $ab \leq 1$.

2) Signals using waveforms with variable envelope shapes:

Unlike the left branch of the tree given in Fig. 31, waveforms with no common envelope shape that are orthogonal are separable and thus suitable for use in signaling. Orthogonal polynomials are examples of such families of waveform.

Operations on the receiver side must act on a discretized version of the received signal. These operations include projection onto the signaling waveforms or their bi-orthogonal duals to extract the information symbols. However, waveform properties such as orthogonality and resilience to channel effects that the continuous versions possess might not readily transfer to their discrete counterparts [23, 24]. Gabor waveforms in their discrete representation inherit most of the properties of their continuous counterparts. However, the same is not true for the category of wavelet and polynomial bases.

In this chapter we study the properties of the DPS Orthonormal Basis (ONB) as an example of a Non-Gabor (Variable Envelope Shape) signaling basis. In addition to satisfying orthogonality, the DPSS ONB exhibits higher confinement behavior compared to Gabor bases which results in superior resilience to channel distortion effects. In addition, we propose an optimization framework to find ONBs with optimal confinement.

4.1 TV Channel Discrete Matrix Form with Fractional Delay and Doppler

A commonly used representation for the input-output relationship of a TV channel, $\mathbf{H}_t$, acting on a cyclic-prefixed block of samples in time, $\mathbf{x}$, is given by the matrix-vector equation [8, 25, 26]

$$\mathbf{y} = \mathbf{H}_t\mathbf{x} \tag{0.122}$$

where $\mathbf{H}_t$ is the time domain channel matrix given by (2.61) in Chapter 2.

This model relies on the approximation that given a max delay spread $\tau_{\max}$ in continuous time and an input signal having bandwidth B, the channel can be adequately represented by exactly $\lceil \tau_{\max} / B \rceil$ taps at integer multiples of $1/B$. However, in the presence of fractional delays that are not multiples of $1/B$, due to the phenomenon of leakage, fictitious taps arise in locations beyond the nominal dimension $\lceil \tau_{\max} / B \rceil$ and these are ignored in the integer tap model. In the frequency domain on the other hand, fractional frequency components that are not multiples of $1/N$, N being the block size, are known to be a major source of modeling error in the CE-BEM model, thus prompting the use of better models such as OCE-BEM [27].

Specular components with integer delay and Doppler are mapped to sub and super (only for Doppler) diagonals in the time-varying impulse response matrix, $\mathbf{H}_t$, and frequency coupling matrix, $\mathbf{H}_f$, respectively. Fractional components on the other hand do not have such a direct mapping. The channel matrix representation that can accommodate both fractional and integer components is given by the *specular time-varying transfer function*:

$$\boldsymbol{H} = \sum_{i,j} \gamma_{i,j} \boldsymbol{\upsilon}_i \boldsymbol{\tau}_j \tag{0.123}$$

where $\boldsymbol{\upsilon}_i = \left[1, ..., e^{j2\pi\upsilon_i N_t}\right]^H$, $\boldsymbol{\tau}_j = \left[1, ..., e^{j2\pi\tau_i N_f}\right]^H$, and $\gamma_{i,j}$ is the gain of the specular component having delay τ_i and Doppler υ_j. In matrix form, this can be written as:

$$\boldsymbol{H} = \mathbf{N}\boldsymbol{\Gamma}\mathbf{T}^H \tag{0.124}$$

where $\mathbf{N}, \mathbf{T}$ are matrices of sizes $N_t \times N_\upsilon$ and $N_\tau \times N_f$ respectively, where N_t, N_f denote the dimensions of the time-frequency grid and N_υ, N_τ are the dimensions of $\boldsymbol{\Gamma}$ which can be thought of as the discrete equivalent of the spreading function.

The time-varying transfer function given in (4.5) is not in the operator form that can be used for a block input-output relation as in (4.3) hence the distinction by using the italicized symbol. For a block of N samples in the time domain, the operator in the time domain, $\mathbf{H_t}$ in (4.3), is given by:

$$\mathbf{H_t} = \left(\boldsymbol{H} \circ \mathbf{F}^H\right)\mathbf{F} \tag{0.125}$$

where the time-frequency grid of the time-varying transfer function $\boldsymbol{H}$ has dimensions $N_t = N_f = N$ and $\mathbf{F}$ is a (square) DFT matrix of size N.

Substituting (4.5) into (4.6) gives the time domain operator form:

$$\mathbf{H_t} = \left(\mathbf{N}\boldsymbol{\Gamma}\mathbf{T}^H \circ \mathbf{F}^H\right)\mathbf{F} \tag{0.126}$$

The operator form in (4.7) gives insight into the structural characteristics that are shared by all channel realizations for a prescribed set of channel parameters. The only factor that varies across realizations is $\boldsymbol{\Gamma}$. Thus, $\mathbf{N}$, $\mathbf{T}$ and $\mathbf{F}$ can be considered as ***static factors*** across realizations. Knowledge of $\mathbf{N}$ and $\mathbf{T}$ requires the knowledge of the parameters υ_l and τ_l for all specular components, which can be infeasible. Instead, with the knowledge of only two parameters: $\upsilon_{\max}$ and $\tau_{\max}$, a 2D DPS-BEM approximation can serve as a proxy

for the exact representation in (4.7) where the matrices $\mathbf{N}$, $\mathbf{T}$ are replaced by $\mathbf{B}_{\upsilon}$, $\mathbf{B}_{\tau}^{H}$ respectively:

$$\mathbf{H}_{\mathbf{t}} \approx \left(\mathbf{B}_{\upsilon}\mathbf{\Gamma}\mathbf{B}_{\tau}^{H} \circ \mathbf{F}^{H}\right)\mathbf{F} \tag{0.127}$$

where $\mathbf{\Gamma}$ is a matrix consisting of $N_t\upsilon_{\max} \times N_f\tau_{\max}$ coefficients.

In [28] a 2-D DPS-BEM is given that can capture both fractional delay and Doppler components which, unlike the form in (4.8), is limited to the specific case of a channel that is quasi-static over a block. A more general 2-D DPS-BEM was given in [29] but it was not clear how the authors obtained the operator form $\mathbf{H}_t$ without the transition through the time-varying transfer function form.

4.2 Signal Design Considerations in the absence of Channel Effects: Gabor Basis Signaling

Multicarrier signals used in communications fall in the subcategory of Gabor systems, as shown in Fig. 31, which consist of the set of time-shifted (translated) and frequency-shifted (modulated) versions of a base function $g(t) \in L^2\left(\mathbb{R}\right)$ where the time and frequency shifts are integer multiples of $a > 0$ and $b > 0$ respectively:

$$G\left(g,b,a\right) := \left\{g_{m,n}\left(t\right)\right\}_{m,n\in\mathbb{Z}} \text{ , } g_{m,n}\left(t\right) = E_{mb}T_{na}g\left(t\right) \tag{0.128}$$

where $E_b f\left(t\right) = e^{i2\pi bt} f\left(t\right)$ and $T_a f\left(t\right) = f\left(t-a\right)$.

Equation (4.9) can be visualized by a 2-D grid where the step size along the x-axis is a and the step size along the y-axis is b. The bandwidth efficiency of the signaling is equal to the lattice density:

$$\eta_{BW} = \frac{1}{ab} \tag{0.129}$$

In the absence of channel effects, the main consideration in signal design is to ensure the separability of data modulated on the different signaling components, which implies the need for perfectly separable signaling components. This is only satisfied when the Gabor system is minimal, i.e. $g_{m_0,n_0}(t) \notin \text{span}\left\{g_{m,n}(t)\right\}_{m\neq m_0, n\neq n_0}$ that can only be satisfied when $1/ab \leq 1$. For $ab=1$, a minimal *Gabor Frame* is obtained, i.e. the set $\left\{g_{m,n}(t)\right\}$ is a basis which could be either orthogonal or bi-orthogonal with a dual set $\left\{\tilde{g}_{m,n}(t)\right\}$.

4.3 Resilience to Time-Frequency Dispersion Channel Effects

State of the art communications is based on Gabor basis signaling schemes which include the widely successful OFDM and its other variants that incorporate non-rectangular pulse shapes. Some of the advantages of Gabor bases that make them suitable for signaling purposes are the following properties:

1) Analytical Tractability

All components in the Gabor basis set are described using a common analytical expression with only two parameters that vary across members of the set. This facilitates obtaining compact expressions describing the different properties of the Gabor set such as the *ambiguity function*, which characterizes the time-frequency spread and is visualized using the phase space graph.

2) Modulation Complexity Rate

The modulation complexity rate is the number of operations required to encode data onto signaling components to generate one symbol. For a Gabor basis, the symbol generation operations consist of frequency shifts by integer multiples of a base frequency, which can be efficiently achieved using a DFT. In the presence of pulse-shaping, a Polyphase Filterbank [30] implementation can be used.

The components of a Gabor basis signal, after passing through a dispersive channel, can no longer be separated by projection at the receiver and as a result Inter-Component

Interference (ICI) ensues. The only exception is CP-OFDM which is perfectly immune to Inter-Component Interference (ICI), given the proper choice of a cyclic prefix. However, this is only true given the status quo of typical operating scenarios which result in channel behavior that can be considered *quasi-static over a symbol period*. On the other hand, prospective modes of operation for the near future involve channel behavior that is highly time-varying and thus will compromise OFDM's ICI immunity.

Due to ICI, a single Gabor basis component experiences the summed interference from its neighboring components while more distant neighbors produce lesser contributions. The extent of a single component's contribution is dependent on the spread caused by the channel in addition to *inherent time-frequency spread of the chosen Gabor basis* which is determined by the prototype pulse shape $g[n]$. Thus, the choice of a pulse shape with high time-frequency confinement is critical to reducing the ICI effect.

4.4 Limits on Time-Frequency Confinement of a Pulse

Without loss of generality, continuous time notation is used to represent measures of time and frequency confinement. Spread can be specified using different measures depending on the utility of the measure. The widely used measure of rms spread that is amenable to normed vector space operations is given by:

$$\left\| xf(x) \right\|_2 \tag{0.130}$$

where $\left\| . \right\|_2$ denotes $L^2(\mathbb{R})$ norm.

For a pulse shape, $g(t)$, the time and frequency rms spreads are given respectively as:

$$\left\| tg(t) \right\|_2 \ , \ \left\| \omega \hat{f}(\omega) \right\|_2 \tag{0.131}$$

where $\hat{f}$ denotes the Fourier transform.

According to the classical uncertainty principle, the product of time and frequency rms spreads cannot go below a certain limit, which is defined formally as follows:

Condition 1: *If* $f \in L^2(\mathbb{R})$ *then*

$$\frac{1}{4\pi}\|f\|_2^2 \le \|tf(t)\|_2 \left\|\omega \hat{f}(\omega)\right\|_2 \tag{0.132}$$

A second limiting condition that governs pulse shapes whose time-frequency versions form a Gabor basis is due to the Balian-Low Theorem [23]:

Condition 2: If $g(t) \in L^2(\mathbb{R})$ *can be used as a pulse shape to generate a Gabor basis set* $\{g_{mn}(t)\}$ *then:*

$$\|tg(t)\|_2 \|\omega \hat{g}(\omega)\|_2 = +\infty \tag{0.133}$$

Thus, no pulse shape can satisfy simultaneous time and frequency confinement in the rms sense and generate a Gabor basis from its time-frequency shifted versions.

The Gaussian pulse shape is known to have optimal time-frequency confinement by satisfying equality in (4.13), i.e. condition 1. However, time-frequency shifted versions of a Gaussian pulse shape will not be orthogonal. On the other hand, a Nyquist pulse [31] shape with excess bandwidth parameter $\alpha \in [0,1]$ has finite rms spread in both time and frequency in addition to satisfying orthogonality between its time-frequency shifted versions. However, this orthogonality is only possible with a time-frequency shift step $(T,(1+\alpha)/T)$ in time and frequency respectively causing the Gabor basis to be incomplete thus reducing the bandwidth efficiency by a factor of $(1+\alpha)$. The Nyquist pulse shaping approach can be thought of as the dual pair of CP-OFDM which uses a guard band in frequency in contrast to the cyclic prefix guard interval in time. Thus, it can be said that the bandwidth efficiency loss due to the excess bandwidth of a Nyquist pulse is similar to that caused by the cyclic prefix in OFDM. However, the efficient DFT-based implementation of multicarrier modulation is only possible when the frequency spacing between subcarriers is an integer multiple of the reciprocal of the symbol period, i.e. n/T

. Thus, for Nyquist pulse shaping with an excess bandwidth factor $0 < \alpha \leq 1$, the minimum frequency spacing must be $2/T$, thereby causing the bandwidth efficiency to be less than that of CP-OFDM.

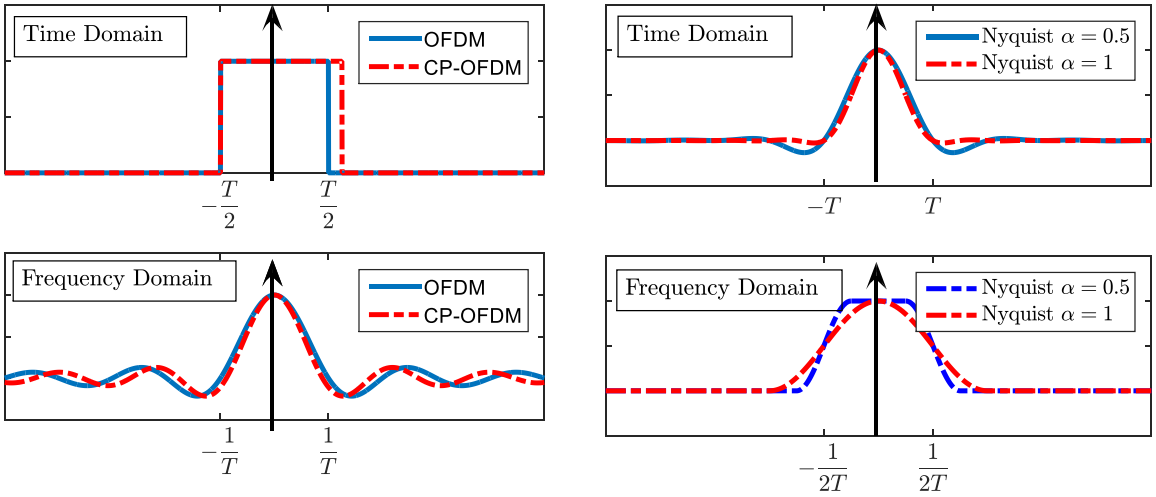

(a) (b)

Figure 32(a) (CP)-OFDM: Rectangular pulse shape. (b) Nyquist pulse shape. (Top) Time Domain, (Bottom) Frequency Domain.

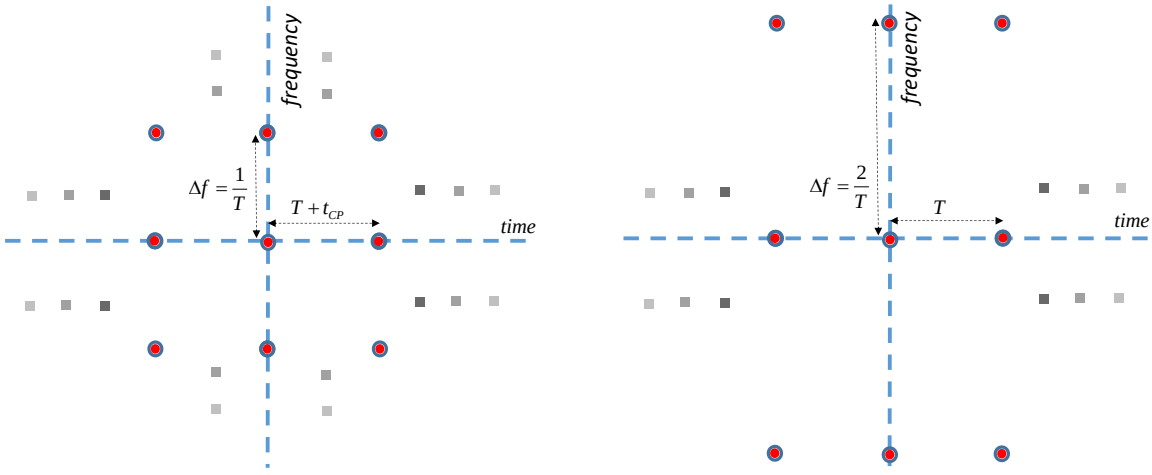

$$\eta_{BW} = \frac{1}{(T + t_{CP})\Delta f} = \frac{T}{(T + t_{CP})}, \quad 0 \leq \eta_{BW} \leq 1$$

$$\eta_{BW} = \frac{1}{T\Delta f} = \frac{T}{T(1+\alpha)}, \quad 0 \leq \eta_{BW} \leq 0.5$$

Figure 33: Symbol Lattice and Bandwidth Efficiency: (Left) CP-OFDM; (Right) Nyquist Pulse.

4.6 Even Pulse Shape and Real Orthogonality

By relaxing the orthogonality condition to the *real inner product* and restricting the pulse shape to being real and even (otherwise arbitrary) as given by (4.15), it is possible to obtain a tighter packing of orthogonal symbols yielding a bandwidth efficiency that exceeds the limit set by the Balian-Low Theorem [32] $\left(\eta \le 0.5\right)$.

$$\begin{aligned} &\mathrm{Re}\left\{\left\langle a_0 g\left(t\right), a_{mn} E_m T_n g\left(t\right)\right\rangle\right\} \text{ for } \left(m,n\right) \ne \left(0,0\right) \\ &g\left(t\right) = g\left(-t\right), \ \mathrm{Im}\left\{g(t)\right\} = 0 \end{aligned} \tag{0.134}$$

The set of $\left(m,n\right)$ values that satisfy (3.14) can be broken down into two categories:

<u>Category 1:</u> $\mathrm{Im}\left\{a_0\right\} + \mathrm{Re}\left\{a_{mn}\right\} = 0$ or $\mathrm{Re}\left\{a_0\right\} + \mathrm{Im}\left\{a_{mn}\right\} = 0$

1- $n = 2k,\ m = 2l+1,\ k,l \in \mathbb{Z}$:

$$\mathrm{Re}\left\{\left\langle a_0 g\left(t\right), a_{mn} e^{jm\pi t/T} g\left(t - nT\right)\right\rangle\right\} = \int g\left(t\right) g\left(t - 2kT\right) \sin\left(\frac{\pi(2l+1)t}{T}\right) dt = 0$$

2- $n = 2k+1, m = 2l,\ k,l \in \mathbb{Z}$:

$$\mathrm{Re}\left\{\left\langle a_0 g\left(t\right), a_{mn} e^{jm\pi t/T} g\left(t - nT\right)\right\rangle\right\} = \int g\left(t\right) g\left(t - (2k+1)T\right) \sin\left(\frac{\pi(2l)t}{T}\right) dt = 0$$

The term $g\left(t\right) g\left(t-(2k+1)T\right)$ being symmetric about its midpoint, its product with an odd function about its midpoint gives an anti-symmetric function for the integrand which sums to 0. The above condition ensures the anti-symmetry of the sine function about its midpoint by completing an even number of half cycles $\left(2l+1\right)\left(2k\right)$ in the time shift duration $\left(2l+1\right)T$.

Category 2: $\mathrm{Im}\{a_0\}+\mathrm{Im}\{a_{mn}\}=0$ or $\mathrm{Re}\{a_0\}+\mathrm{Re}\{a_{mn}\}=0$

1- $n=2l+1,\ m=2k+1,\ k,l\in\mathbb{Z}$:

$$\mathrm{Re}\left\{\left\langle a_0 g(t), a_{mn} e^{jm\pi t/T} g(t-nT)\right\rangle\right\}=\int g(t)\,g(t-(2l+1)T)\cos\left(\frac{\pi(2k+1)t}{T}\right)dt=0$$

In contrast to category 1, the integrand becomes an odd function when the cosine function completes an odd number of half cycles in the time shift duration $(2l+1)T$.

Figure 33 shows on the left the set of locations that fall in category 1, which are locations in the imaginary domain (red circles) immune to interference from a purely real symbol transmitted at the relative location $(m,n)=(0,0)$ (blue square). On the right, the set of locations that fall in category 2 are shown, which are locations in the real domain that are immune to interference from a real symbol at $(m,n)=(0,0)$.

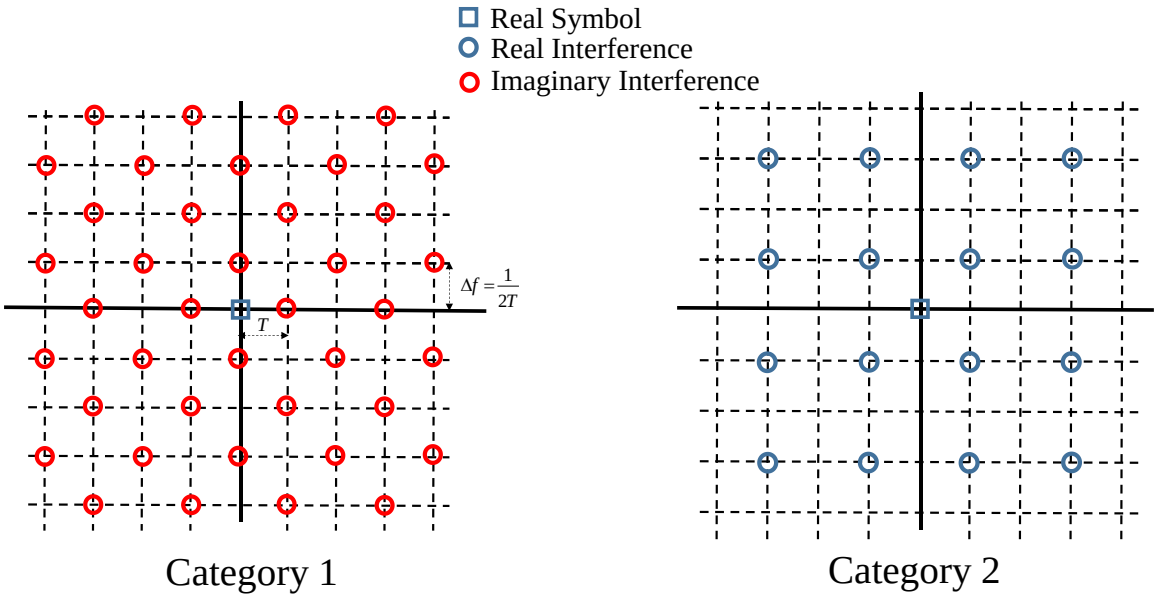

Figure 34: (Left) Category 1 Grid Locations; (Right) Category 2 Grid Locations.

In order for a simple uniform placement of multiple symbols to be possible, similar to CP-OFDM and Nyquist pulse shaping, the grid representing interference of one symbol to all other locations must also be uniform.

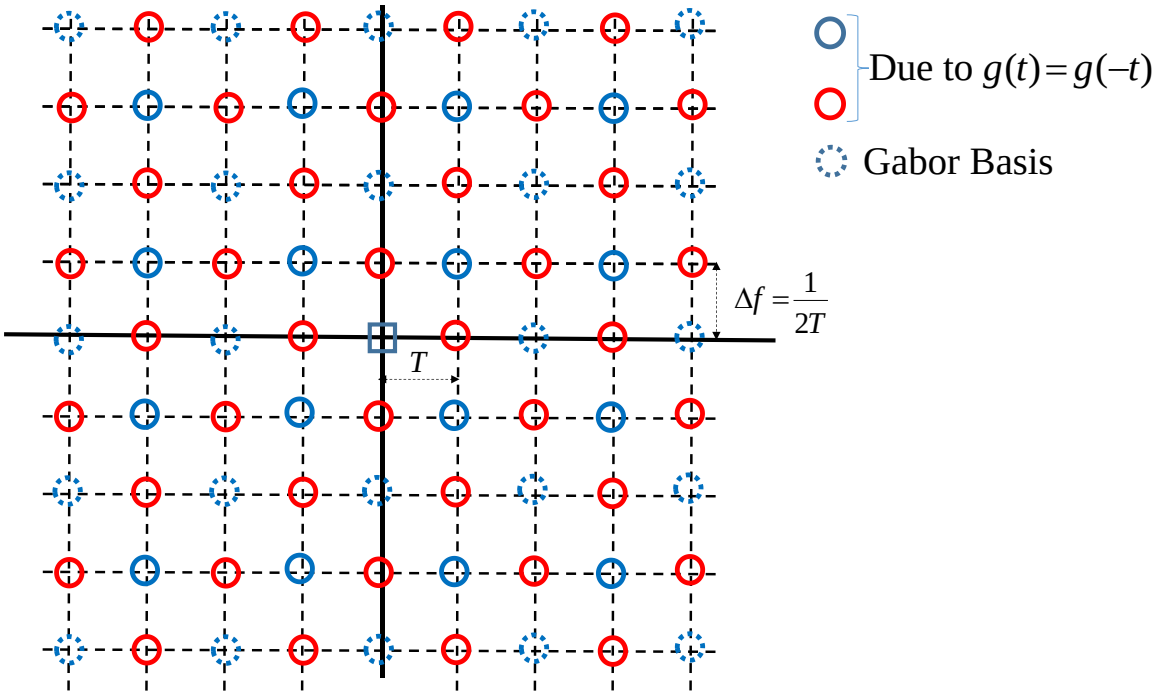

Figure 35: (Solid red) locations in category 1. (Solid blue) locations in category 2. (Dotted Blue) Locations that Need to be Filled with Solid Blue Circles (real interference) to make the Entire Grid Uniform.

By combining both category 1 and category 2 interference locations in Fig. 35, it is revealed that uniformity will be satisfied if the set of locations $n = 2l,\ m = 2k,\ k,l \in \mathbb{Z}$ correspond to zero interference in the real domain, i.e. blue circles.

Except for the symmetry constraint, the filter shape remains a free variable that can be optimized to fill the vacant locations by satisfying the following constraint:

$$\text{For } \mathrm{Im}\{a_0\} + \mathrm{Im}\{a_{mn}\} = 0,\ k,l \in \mathbb{Z},\ \int g(t)\, g(t - 2lT) \cos\left(\frac{\pi 2kt}{T}\right) dt = 0 \quad (0.135)$$

Since the real orthogonality constraint is subsumed by general orthogonality, satisfying the following constraint is sufficient:

$$\left\langle a_0 g(t), a_{mn} e^{j2k\pi t/T} g(t - 2lT) \right\rangle = 0 \quad (0.136)$$

Thus, now the requirement is reduced to designing a Gabor basis with density $1/(2T \times 1/T) = 0.5$ that is within the Balian-Low limit which allows the use of non-rectangular pulse shapes.

Now that the interference pattern is periodic and uniform, it is possible to define a simple tiling rule for populating the time-frequency grid with symbols:

Table 3: Locations of Real and Imaginary Symbols

Real	*Imaginary*
$(k+l) = even$	$(k+l) = odd$

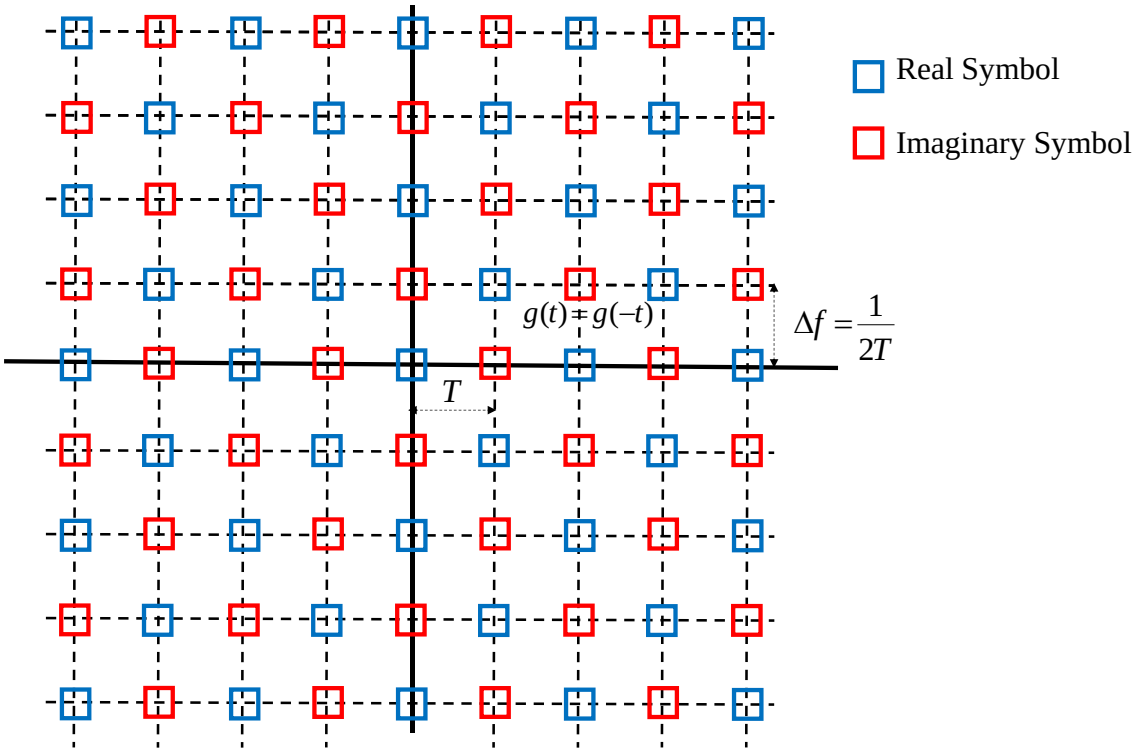

Figure 36: Staggered Symbol Arrangement in Time-Frequency Plane

4.7 OFDM/OQAM Orthonormal Gabor Bases: Finite length and Discretization Constraints

The modulation scheme following the symbol arrangement in the time-frequency plane shown in Fig. 36 was invented by Chang [33] and developed by others [34, 35] to its present form, which is known as OFDM/OQAM.

The continuous time treatment for the baseband transmit signal appears in the following form:

$$s(t)=\sum_{k=0}^{M-1}\sum_{l=-\infty}^{\infty} j^k c_{k,l}^R g\left(t-lT_s\right)e^{j(\pi/T_s)kt}+\sum_{l=-\infty}^{\infty} j^{k+1} c_{k,l}^I g\left(t-lT_s-T_s/2\right)e^{j(\pi/T_s)kt} \quad (0.137)$$

where a complex symbol stream $c_{k,l}$ is split into 2 streams, each formed exclusively from the real and imaginary components: $c_{k,l}^R$ and $c_{k,l}^I$ respectively, where k,l represent the frequency subcarrier and symbol indices respectively. The symbol period of each of the streams is twice the time step of the grid shown in Fig. 36, i.e. $T_s=2T$ and hence are offset by half a symbol period $T_s/2=T$.

For the sake of practical realization, the treatment must be discretized [36, 37] and the pulse shape must be of finite support and causal. Limiting the support of the pulse shape $g(t)$ to the duration $\left[-LT_s/2, LT_s/2\right]$, shifting the continuous time signal in (4.18) by $(L-1)T_s/2$ to ensure causality, and defining the discrete pulse shape sequence $g[n]=g\left(\left(k-\frac{L-1}{2}\right)T_s\right)$, the discretized form of (4.18) is given by:

$$x[n]=\sum_{k=0}^{M-1}\sum_{l=-\infty}^{\infty} j^k c_{k,l}^R g[n-lM]e^{j\frac{2\pi}{M}k\left(n-\frac{L-1}{2}\right)}+\sum_{l=-\infty}^{\infty} j^{k+1} c_{k,l}^I g[n-lM-M/2]e^{j\frac{2\pi}{M}k\left(n-\frac{L-1}{2}\right)}$$

(0.138)

where a complex symbol stream $c_{k,l}$ is split into 2 streams, each formed exclusively from the real and imaginary components: $c_{k,l}^{R}$ and $c_{k,l}^{I}$ respectively, where k, l represent the frequency subcarrier and symbol indices respectively. The symbol period of each of the streams is twice the time step of the grid shown in Fig. 36, i.e. $T_s = 2T$ and hence the offset is half a symbol period $T_s / 2 = T$.

Expressing the $L-1$ term in the exponent of (4.19) as the sum of two components,

$$L-1=(2r+1)M/2+\alpha \tag{0.139}$$

where the first term is an offset multiple of the symbol period and the second term a remainder $\alpha \in [0, M-1]$, substitution in (4.19) enables the following decomposition of the exponential term:

$$e^{j(2\pi/M)k\left(n-\frac{\alpha}{2}\right)}e^{-j\frac{\pi}{2}k(2r+1)} = e^{j(2\pi/M)k\left(n-\frac{\alpha}{2}\right)}((-1)^{r+1}j)^{k} \tag{0.140}$$

Equation (4.19) now becomes:

$$\begin{aligned} x[n] &= (-1)^{r+1}\sum_{k=0}^{M-1}\sum_{l=-\infty}^{\infty} j^{2k}c_{k,l}^{R}g[n-lM]\phi_{k,n} + \sum_{l=-\infty}^{\infty} j^{2k}c_{k,l}^{I}g[n-lM-M/2]\phi_{k,n} \\ &= (-1)^{r+1}\sum_{k=0}^{M-1}(-1)^{k+1}\sum_{l=-\infty}^{\infty} c_{k,l}^{R}g[n-lM]\phi_{k,n} + j\sum_{l=-\infty}^{\infty} g[n-lM-M/2]\phi_{k,n} \end{aligned} \tag{0.141}$$

where $\phi_{k,n} = e^{j(2\pi/M)k\left(n-\frac{\alpha}{2}\right)}$.

Now the form in (4.22) no longer has the 90^{o} phase alternation across subcarriers and the I and Q data streams are distinctly defined.

As explained in the previous section, the property of the filter function being even satisfies condition (1)-(3) in the following list:

1) $\sum_{n=-\infty}^{\infty} g[n-lM]g[n]\cos\left(\frac{2\pi}{M}m(n-\alpha/2)\right)=\delta[l]\delta[m]$

2) $\sum_{n=-\infty}^{\infty} g[n+M/2-lM]g[n]\sin\left(\frac{2\pi}{M}m(n-\alpha/2)\right)=0$

3) $\sum_{n=-\infty}^{\infty} g[n-lM]g[n+M/2]\sin\left(\frac{2\pi}{M}m(n-\alpha/2)\right)=0$

4) $\sum_{n=-\infty}^{\infty} g[n+M/2-lM]g[n+M/2]\cos\left(\frac{2\pi}{M}m(n-\alpha/2)\right)=\delta[l]\delta[m]$

The fourth condition can be rewritten as:

$$\frac{1}{2}\langle g, g_{l,-m}\rangle+\frac{1}{2}\langle g, g_{l,m}\rangle=\delta[l]\delta[m] \tag{0.142}$$

where $\langle a,b\rangle=\sum_{n=-\infty}^{\infty} a[n]b^{*}[n]$.

For $m\neq 0$, (4.21) becomes:

$$\frac{1}{2}\langle g, g_{l,-m}\rangle=-\frac{1}{2}\langle g, g_{l,m}\rangle \tag{0.143}$$

which can be expressed in terms of z-transforms:

$$\mathcal{Z}_{y_l}\left(\frac{4\pi}{M}m\right)=-\mathcal{Z}_{y_l}\left(\frac{-4\pi}{M}m\right) \tag{0.144}$$

where $\mathcal{Z}_{y_l}\left(\frac{4\pi}{M}m\right)=\sum_{n=-\infty}^{\infty}\underbrace{g[n]g[n-lM]}_{y_l(n)}e^{-j\left(\frac{m4\pi}{M}\right)n}$.

Equation (4.25) can only be satisfied if $y(l,n)$ is odd in *n*. However this is not the case due to the initial choice of $g[n]$ being even. Therefore, (4.23) can only be satisfied when the following condition is true:

$$\left\langle g_{l,m}, g_{l',m'} \right\rangle = \delta[l-l']\delta[m-m'] \tag{0.145}$$

Equation (4.24) can be written in terms of the Zak transform $L(n,\theta)$ as follows:

$$\left|L(n,\theta)\right|^2 + \left|L(n,\theta-1/2)\right|^2 = \frac{4}{M},\ n = 0,1,...,\frac{M}{2}-1,\ \theta \in [0,1) \tag{0.146}$$

where the Zak transform of $g(n)$ is defined as $L_g(n,\theta) = \sum_{r=-\infty}^{\infty} g\left[n + r\frac{M}{2}\right] e^{-j2\pi r\theta}$.

The problem of finding the desired pulse shape that retains orthogonality is simplified to, in the Zak transform domain, an algebraic problem which has the following form:

$$f(n,\theta)^2 + f(n,\theta-\frac{1}{2})^2 = \frac{4}{M},\ n = 0,1,...,\frac{M}{2}-1,\ \theta \in [0,1) \tag{0.147}$$

Strictly speaking the above form is underdetermined and has an infinite number of solutions. However, not all solutions are admissible. An admissible solution can be obtained by (4.29), which consists of a simple scaling of the Zak transform of an initial pulse shape $g[n]$ having good properties, such as frequency confinement. The resulting pulse $\tilde{g}[n]$ will inherit the good frequency confinement of the initial pulse shape in addition to orthogonality.

$$L_{\tilde{g}}(n,\theta) = \frac{2L_g(n,\theta)}{\sqrt{M\left|L_g(n,\theta)\right|^2 + M\left|L_g(n,\theta-\frac{1}{2})\right|^2}} \tag{0.148}$$

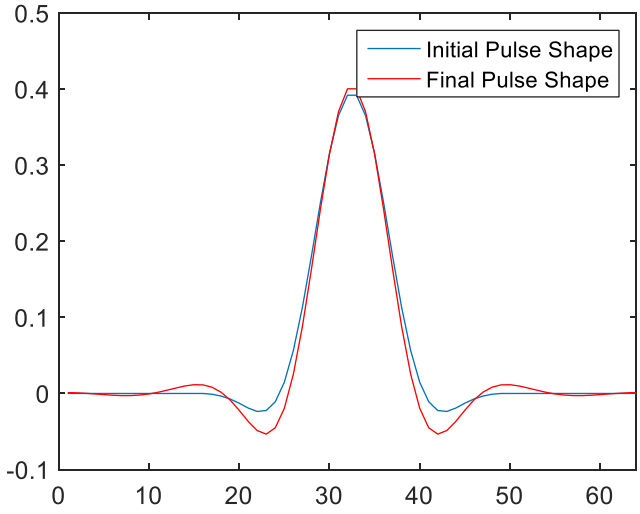

Figure 37: Pulse Shapes Before and After Orthogonalization in the Zak Domain.

Figure (37) shows the initial and final pulse shapes with parameters: $L_g = 64$, $M = 8$.

As a check for orthogonality, the following criterion can be applied:

$$\mathrm{Re}\left\{\sum_{n=0}^{Lg-1} g[n]e^{j(2\pi/M)l(n-\alpha/2)} g[n]e^{-j(2\pi/M)m(n-\alpha/2)}\right\} = \delta[l-m] \qquad (0.149)$$

which takes the matrix form in (4.31) that is visualized in Fig. 37.

$$\mathrm{Re}\left\{\tilde{\mathbf{G}}^H\tilde{\mathbf{G}}\right\} = \mathrm{Re}\left\{\tilde{\mathbf{F}}^H D(g) D(g)\tilde{\mathbf{F}}\right\} = \tilde{\mathbf{I}} \qquad (0.150)$$

where $\left[\tilde{\mathbf{F}}\right]_{l,n} = e^{j(2\pi/L_g)l(n-\alpha/2)}$ and $\left[\tilde{\mathbf{I}}\right]_{l,m} = \delta\left[\frac{(l-m)}{L_g/M}\right]$.

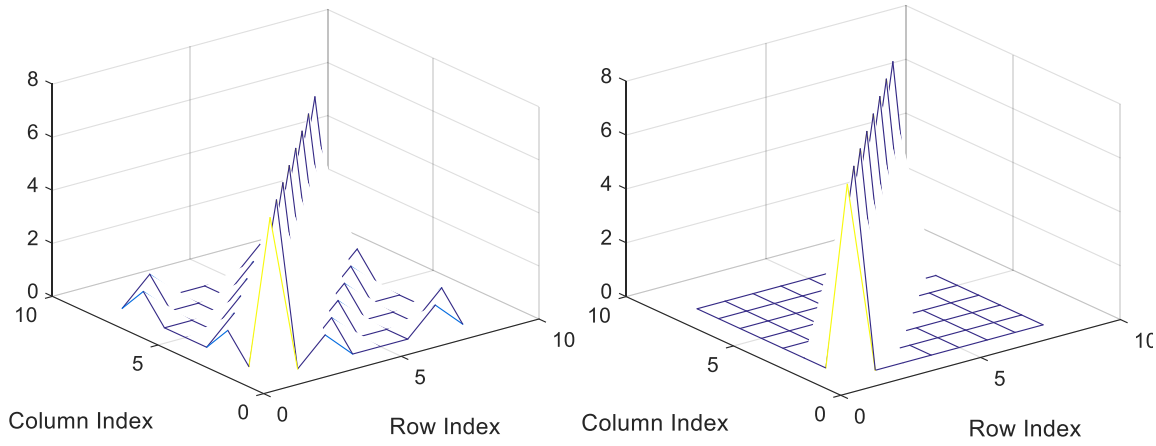

(a) (b)

Figure 38: (Left) Orthogonality Pattern of Initial Pulse Shape. (Right) Orthogonality Pattern of Final Pulse Shape.

4.8 Strictly Time-limited Pulses

The OFDM/OQAM scheme makes it possible to attain maximum bandwidth efficiency while using pulse shapes with good time-frequency confinement. However, to obtain good confinement the pulse shape must span multiple block periods. In spite of overlap, IBI will be eliminated due to the orthogonality endowed by the choice of appropriate pulse shapes as discussed in the previous section. However, in the presence of channel dispersion, orthogonality is destroyed and the only line of defense left against IBI is good confinement in time and frequency. OFDM/OQAM pulse shapes typically are chosen to give good frequency confinement at the expense of longer pulse durations and poor time confinement. Due to the poor time confinement, equalization at the receiver is required to eliminate IBI caused mainly due to time dispersion since frequency dispersive effects are assumed to be curtailed by the good frequency confinement. In [38] however, the authors point out the lack of an analytical justification for the efficacy of single tap equalization for OQAM/FBMC since treating channel dispersion as a circular convolution operation is no longer valid in the absence of a CP.

Overlap between multiple symbols in time prevents the use of a block treatment. This is undesirable in rapidly time-varying channel conditions where per-block operations

including equalization and channel estimation are necessary. Alternatively, applying block operations to a full frame (assuming frames are separated by guard intervals) can be computationally infeasible. Thus, the only option left is to rely on streaming equalization techniques which are inferior in performance to block equalizers [39].

Another undesirable consequence of lengthy pulses is the trailing transmission time due to the pulse tail. In Internet-of-Things (IoT) applications, burst transmissions made of short frames are used more often than long streaming frames. For such frames, the trailing transmission time will incur a high loss in throughput. Fig. 38 shows a frame consisting of 5 blocks where the throughput efficiency is close to 50%.

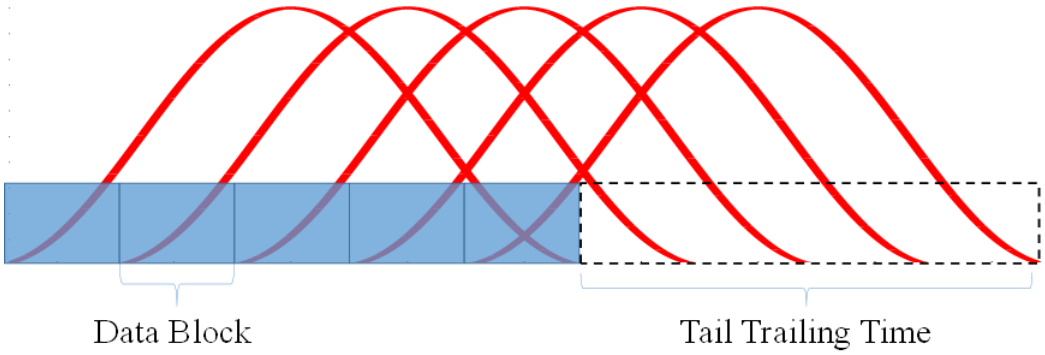

Figure 39: OFDM/OQAM Frame Consisting of 5 Data Blocks using Pulse Shape Overlap Factor of 5

4.8.1 Discrete Prolate Spheroidal Signaling Basis

Gabor Bases having frequency confinement limitations and OFDM/OQAM lacking in the block treatment aspect are reasons that motivate the search for non-Gabor signaling systems which do not have these shortcomings. Additionally, signaling based on non-Gabor Orthonormal Bases (ONB) remains unexplored territory and has not been investigated rigorously.

The per-block discretized input-output relationship for ONB signaling with cyclic prefix extension using basis $\mathbf{O}$ is given by:

$$\mathbf{z} = \mathbf{O}^H \mathbf{H}_t \mathbf{O}\mathbf{x} + \mathbf{O}^H \mathbf{n} \tag{0.151}$$

where $\mathbf{O}$ is a matrix whose columns are the component vectors, $\mathbf{x}$ is a vector of data symbols which modulate the columns of $\mathbf{O}$, $\mathbf{n}$ is the noise vector, and $\mathbf{H}_t$ is the time domain channel matrix. All matrices and columns have dimensions $N \times N$ and $N \times 1$ respectively.

OFDM signaling corresponds to ONB $\mathbf{O} = \mathbf{F}$, where $\mathbf{F}$ is a DFT matrix of size N. The lack of frequency confinement in OFDM manifests as a slow *off-band diagonal decay* in the equivalent channel matrix:

$$\mathbf{H}_{eq} = \mathbf{F}^H \mathbf{H}_t \mathbf{F} \tag{0.152}$$

Off-band diagonals consist of the elements of the matrix that do not fall in the nominal band of spread caused by Doppler $\upsilon_{\max}$, according to the following definitions:

$$\underline{\text{Nominal band:}} \ \left\{ a_{i,j} : |i-j| \le \upsilon_{\max} \right\}$$

$$\underline{\text{Off-band diagonal band:}} \ \left\{ a_{i,j} : |i-j| > \upsilon_{\max} \right\}$$

The rate of decay can be found by analyzing the channel matrix and how the basis interacts with each of its components. The channel matrix can be analyzed into its constituent components as follows:

$$\mathbf{H}^{(tt)} = \left(\boldsymbol{H} \circ \mathbf{F}^H \right) \mathbf{F} \tag{0.153}$$

where $\boldsymbol{H} = \sum_{l,m} \gamma_{l,m} \boldsymbol{\upsilon}_l \boldsymbol{\tau}_m^H$, $\left[\boldsymbol{\upsilon}_l \right]_n = e^{-j2\pi\upsilon_l \frac{n}{N}}$, $\left[\boldsymbol{\tau}_l \right]_k = e^{-j2\pi\tau_l \frac{k}{N}}$ and Hadamard product $\circ$.

Substituting (4.33) into (4.32):

$$\begin{aligned}\mathbf{H}_{eq} &= \mathbf{O}^H \mathbf{H}_t \mathbf{O} \\ &= \sum_{l,m} \gamma_{l,m}\, \mathbf{O}^H \left(\boldsymbol{\upsilon}_l \boldsymbol{\tau}_m^H \circ \mathbf{F}^H \right) \mathbf{F}\mathbf{O} \\ &= \sum_{l,m} \gamma_{l,m} \underbrace{\mathbf{O}^H \mathbf{D}(\boldsymbol{\upsilon}_l) \mathbf{F}^H \mathbf{D}(\boldsymbol{\tau}_m) \mathbf{F}\mathbf{O}}_{\mathbf{M}_{l,m}}\end{aligned} \tag{0.154}$$

In general, the band width of a matrix is defined as the width of the band of diagonals that contain elements of significant magnitude. However, this definition is imprecise and thus we use the following definition to refer to band width:

$$b_\varepsilon(A) := \left\{ b \geq 0 \;\middle|\; \forall i, j \;\; |a_{i,j}| \geq \varepsilon, |i-j| \leq b \right\} \tag{0.155}$$

According to the definition in (4.36), the choice $\varepsilon = 0$ corresponds to strictly banded matrices which form nested vector spaces A_{b_i} that satisfy the following relationship:

$$A_a \subseteq A_b \subseteq \ldots \subseteq A_c \;\; for \;\; a \leq b \leq \ldots \leq c \tag{0.156}$$

where $A_b : \left\{ A \,|\, b_0(A) = b \right\}$.

By definition, the band width of $\mathbf{H}_{eq}$ is determined by the component matrix $\mathbf{M}_{l,m}$ in (4.35) having the largest band width. The band width of a component matrix $\mathbf{M}_{l,m}$ is the sum of the band widths of its multiplicative factors, which are determined according to the choice of basis $\mathbf{O}$.

For $\mathbf{O} = \mathbf{F}$, the component matrix $\mathbf{M}_{l,m}$ in (4.35) satisfies:

$$\begin{aligned}\mathbf{M}_{l,m} &= \mathbf{F}^H \mathbf{D}(\boldsymbol{\upsilon}_l) \mathbf{F}^H \mathbf{D}(\boldsymbol{\tau}_m) \mathbf{F}\mathbf{F}^H \\ &= \underbrace{\mathbf{F}^H \mathbf{D}(\boldsymbol{\upsilon}_l) \mathbf{F}^H}_{\boldsymbol{\psi}_{\mathbf{F}}(\boldsymbol{\upsilon}_l)} \mathbf{D}(\boldsymbol{\tau}_m)\end{aligned} \tag{0.157}$$

where $\left| \left[\boldsymbol{\psi}_{\mathbf{F}}(\boldsymbol{\upsilon}_m) \right]_{i,j} \right| = \dfrac{\sin\left(\left(i - j + \upsilon_m \right) \pi \right)}{\sin\left(\left(i - j + \upsilon_m \right) \pi / N \right)}$.

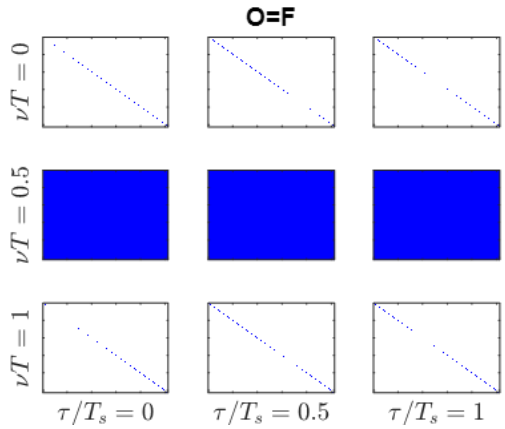

Figure 40: Structure of component matrix $\mathbf{M}_{l,m}$ for $\mathbf{O} = \mathbf{F}^H$.

The bandwidth of the expression in (4.38) is the sum of the band widths of the multiplicative matrix factors: $\boldsymbol{\psi}_{\mathbf{F}}(\upsilon_m)$ and $D(\boldsymbol{\tau}_m)$. The diagonal matrix $D(\boldsymbol{\tau}_m)$ has zero band width and thus the band width is determined by the second factor $\boldsymbol{\psi}_{\mathbf{F}}(\upsilon_m)$, which is a circulant matrix with elements of magnitudes that vary according to the periodic sinc function in the anti-diagonal direction. For integer values of υ_m, the matrix $\boldsymbol{\psi}_{\mathbf{F}}(\upsilon_m)$ consists of a singular sub-diagonal $(j = i + \upsilon,\ i = 0,...,N-1)$. Figure 40 shows the structure of the matrix $\mathbf{M}_{l,m}$ for $\mathbf{O} = \mathbf{F}^H$ across different values of υ_l and τ_m. As a result, the overall matrix $\mathbf{H}_{eq}$ in (4.35) exhibits the slow off-band diagonal decay.

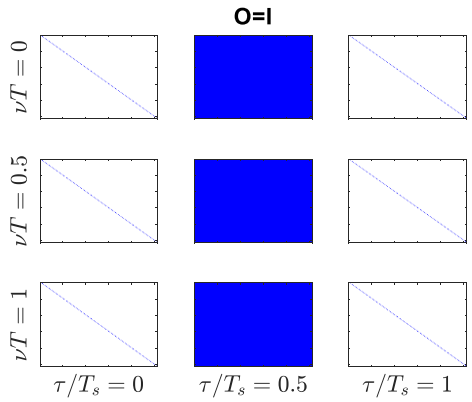

Figure 41: Structure of component matrix $\mathbf{M}_{l,m}$ for $\mathbf{O} = \mathbf{I}$,

The dual ONB (in the sense of time-frequency duality) is the Kronecker Delta (KD) basis, $\mathbf{O} = \mathbf{I}$, which is used for single carrier. The equivalent channel matrix $\mathbf{H}_{eq}$ exhibits a similar slow off-band diagonal decay, which can be analyzed in the same way by substituting $\mathbf{O} = \mathbf{I}$ in the expression for the component matrix given by (4.39) and visualized in Fig. 41.

$$\begin{aligned} \mathbf{M}_{l,m} &= D(\boldsymbol{\upsilon}_l)\mathbf{F}^H D(\boldsymbol{\tau}_m)\mathbf{F} \\ &= D(\boldsymbol{\upsilon}_l)\underbrace{\mathbf{F}^H D(\boldsymbol{\tau}_m)\mathbf{F}}_{\boldsymbol{\psi}(\boldsymbol{\tau}_m)} \end{aligned} \tag{0.158}$$

The lack of confinement of OFDM as well as Single carrier was – as expected – evident in the discrete time treatment in matrix form. The discrete time treatment is more representative of the actual system implementation than the continuous treatment. Therefore, the search for ONBs must be focused on discrete (finite dimensional) ONBs. It is important to note that ONBs in continuous time do not immediately yield ONBs in discrete time by uniform sampling. In fact, only Fourier ONBs possess this property, i.e. sampled versions of the continuous time form inherit orthogonality. Thus, well-known continuous time polynomial ONBs – such as Legendre, Chebyshev, Bessel – are not admissible candidates.

4.8.2 DPS Signaling $\mathbf{O} = \mathbf{S}$

DPS is a finite set of vectors (finite dimensionality N) that form an ONB. In addition, DPS vectors satisfy a property that relates them to the class of so called *Quasi-orthogonal Polynomials* defined in [40]. Following this definition, the finite set of length N discrete variable polynomials, $p_l[n]$, is said to satisfy quasi-orthogonality of order (k,r) with respect to a non-negative weight $w[n]$ when the following conditions hold:

$$\begin{aligned} &\left\langle p_l[n], p_m[n] \right\rangle = \sum_{n=0}^{N-1} w[n] p_l[n] p_m^*[n] = 0 \text{ for } l \neq m \pm jr \\ &p_{-m}[n] = 0,\ j = 0,...,k\ ,\ n = 0,...,N-1 \end{aligned} \tag{0.159}$$

Quasi-orthogonality can be stated in matrix form as $\{\mathbf{M}\}_{l,m} = 0$ for $l \neq m \pm jr$ for the matrix $\mathbf{M} = \mathbf{P}^H \mathbf{D}(\mathbf{w}) \mathbf{P}$, where $\mathbf{P} = [\mathbf{p}_1, ..., \mathbf{p}_N]$, $\mathbf{p}_l = [p_l[1], ..., p_l[N]]^T$, and $\mathbf{D}(\mathbf{w})$ is a diagonal matrix based on $\mathbf{w} = [w[1], ..., w[N]]$. Thus, for $r = 1$ quasi-orthogonality becomes the condition on the aforementioned matrix $\mathbf{M}$ to have non-zero elements only in the band of diagonals $[-k, k]$.

The DPS basis matrix $\mathbf{S} = [\mathbf{s}_1, ..., \mathbf{s}_N]$, with columns arranged in descending order of the corresponding eigenvalue, is observed to approximately satisfy quasi-orthogonality with respect to any of the DC shifted versions of the basis vectors, $\mathbf{v}_i = \mathbf{s}_i + c_i$ where $c_i = \min(\mathbf{s}_i)$, serving as a weight for the inner product. The order of quasi-orthogonality, i.e. the band width, increases monotonically with the order i of the DPS weight vector $\mathbf{s}_i$. Thus, small band widths are limited to the low order component windows.

$$\mathbf{s}_l{}^H D(\mathbf{v}_i) \mathbf{s}_m \leq \varepsilon \text{ for } l \neq m \pm j,\ j = 0, ..., k_i \tag{0.160}$$

where $\varepsilon = f(k_i)$ with f (.) being a monotonically decreasing function.

For time-varying channels with no delay dispersion, the subset of components with orders $1, ..., \lceil \upsilon_{\max} \rceil + 1$ of a DPS basis matched to the max frequency dispersion $\upsilon_{\max}$ is known to span the subspace of all channel realizations [41]. Thus, when DPS signaling is used the equivalent channel matrix is given by:

$$\mathbf{S}^H \mathbf{D}(\mathbf{h}) \mathbf{S} = \sum_{i=1}^{\lceil \upsilon_{\max} + 1 \rceil} \alpha_i \mathbf{S}^H \mathbf{D}(\mathbf{s}_i) \mathbf{S} \tag{0.161}$$

A consequence of the quasi-orthogonality property is that bandedness will be satisfied for all such channel realizations and the band width of the matrix will be determined by the highest order DPSS basis component $\mathbf{s}_{\lceil \upsilon_{\max} \rceil + 1}$.

The property of DPSS being quasi-orthogonal with respect to any purely time dispersive channel is of limited use since such channels are readily in diagonal form when SC transmissions are applied. However, in the presence of time-dispersion and the channel becoming doubly dispersive, the DPSS equivalent channel matrix inherits a weaker version of the bandedness property where the band width k_m decreases with column position as shown in Fig. 40:

$$\mathbf{s}_l^H \mathbf{H} \mathbf{s}_m \leq \varepsilon \text{ for } l \neq m \pm j,\ j = 0, \ldots, k_m \tag{0.162}$$

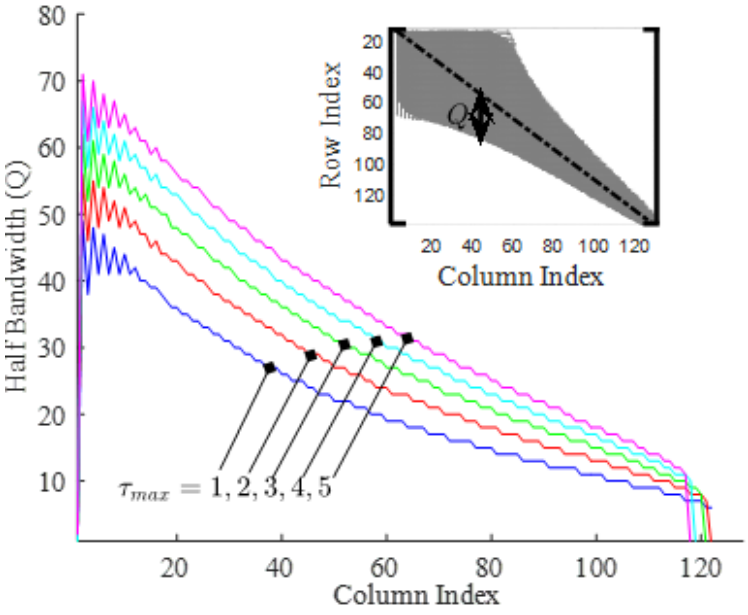

Figure 42: Half Band Width Q of ψ_S for Different Values of Maximum Delay.

Despite not being strictly banded, the non-uniform bandedness in DD channels is still useful when compared to Gabor (OFDM and pulse shaped OFDM) and SC signaling in DD channels which exhibit comparatively slow decay in the skew-diagonal direction.

Applying component analysis to the equivalent channel matrix by substituting $\mathbf{O} = \mathbf{S}$ in (4.35) gives:

$$\begin{aligned} \mathbf{M}_{l,m} &= \mathbf{S}^H D(\boldsymbol{\upsilon}_l) \mathbf{F}^H D(\boldsymbol{\tau}_m) \mathbf{F} \mathbf{S} \\ &= \underbrace{\mathbf{S}^H D(\boldsymbol{\upsilon}_l) \mathbf{S}}_{\boldsymbol{\varphi}_S(\boldsymbol{\upsilon}_l)} \underbrace{\mathbf{S}^H \mathbf{F}^H D(\boldsymbol{\tau}_m) \mathbf{F} \mathbf{S}}_{\boldsymbol{\psi}_S(\boldsymbol{\tau}_m)} \end{aligned} \tag{0.163}$$

Unlike in the case of bases $\mathbf{I}$ and $\mathbf{F}$, there are no purely diagonal factors now. Instead, there is a strictly banded factor $\boldsymbol{\varphi}_{\mathbf{S}}(\upsilon_l)$ due to the quasi-orthogonality property explained in (4.42) and a non-banded factor $\boldsymbol{\psi}_{\mathbf{S}}(\tau_m)$ which is dependent on the channel delay. For bases $\mathbf{I}$ and $\mathbf{F}$ the matrix factor $\boldsymbol{\psi}_{\cdot}(.)$ will have a non-banded slowly decaying pattern for non-integer values of delay and Doppler respectively due to the Dirichlet factor. However, for the DPSS basis, the pattern has a much higher rate of decay and can be approximated by a strictly limited tapered band. As shown in the top right of Fig. 40, the half band width is given by $\left\{\max|j-i|:\left|[\boldsymbol{\psi}_{\mathbf{S}}]_{i,j}\right|\geq 10^{-6}\right\}$ which is the furthest distance from the main diagonal at each location j.

4.9 Channel Adapted Signaling

Adapting/matching the waveform parameters according to the operating channel parameters results in the highest resilience [42]. In fact, CP-OFDM employs a simple form of channel adaptation/matching by setting the length of the cyclic prefix to be longer than the channel delay spread, $\tau_{\max}$. As a result, CP-OFDM is capable of preserving the structure of the encoded information after passing through a random time-dispersive channel with delays within the specified bound.

The structural distortion can be defined as the degree by which the distinct information units are mixed, i.e. the Inter-Symbol Interference (ISI). In the discrete channel treatment, the degree of banded-ness of the equivalent channel matrix, $\mathbf{H}_{eq}$, reflects the structural distortion. This can be quantified by the effective bandwidth, B_{ε}, within which significant energy $(>\varepsilon)$ is contained, which we define as:

$$B_{\varepsilon} = \min B \text{ s.t. } \left\|\text{off}_{B}(\mathbf{H}_{eq})\right\| < \varepsilon \tag{0.164}$$

where $\text{off}_B(\mathbf{H}_{eq})$ is a matrix with the following elements $\left\{\text{off}_B(\mathbf{H}_{eq})\right\}_{i,j} = \left\{\mathbf{H}_{eq}\right\}_{i,j}$ for $|i-j| > B$ and 0 otherwise.

4.9.1 Joint Approximate Bandwidth Reduction (JABR)

The joint approximate bandwidth reduction can be considered as a generalized/extended form of the joint approximate diagonalization objective [43]. It is formulated as the following minimization problem over a set of matrices $\mathbf{R}_k$ with the design variable $\mathbf{W}$ subject to unitary constraints:

$$\arg\min_{\mathbf{W}} \sum_{k=1}^{N} \left\| \text{off}_B\left(\mathbf{W}^{\mathrm{H}}\mathbf{R}_{\mathrm{k}}\mathbf{W}\right)\right\|_F^2 \quad \text{s.t. } \mathbf{W}^H\mathbf{W} = \mathbf{I} \tag{0.165}$$

The operation $\text{off}_B\left(\mathbf{A}\right)$ used in (4.46) can be rewritten in terms of matrix operations as follows:

$$\text{off}_B\left(\mathbf{A}\right) = \mathbf{A} - \sum_{r=-B}^{B} \mathbf{Z}^r \,\text{ddiag}\left(\mathbf{Z}^{-r}\mathbf{A}\right) \tag{0.166}$$

where $\text{ddiag}\left(\mathbf{A}\right)$ returns a diagonal matrix with elements of $\mathbf{A}$ on the main diagonal, and $\mathbf{Z}$ is the circular shift matrix with elements $\left[\mathbf{Z}\right]_{i,j} = \delta\left(\text{mod}(i-j-1, N)\right)$.

As in [44] minimization techniques such as steepest descent and Newton's method can be applied to attain local minima. It is expedient to find compact matrix expressions for the Gradient/Jacobian, which is sufficient for the steepest descent solver, and the Hessian which is additionally required for a Newton's method based solver.

Equation (4.46) can be rewritten in terms of the matrix variable $\mathbf{W}$ as follows:

$$\arg\min_{\mathbf{W}}\left(\sum_{k=1}^{N}\mathrm{tr}\left[\mathbf{W}^{H}\mathbf{R}_{k}^{H}\mathbf{W}\mathbf{W}^{H}\mathbf{R}_{k}\mathbf{W}\right]\right.$$
$$\left.-\sum_{k=1}^{N}\mathrm{tr}\left[\sum_{r=-B}^{B}\mathrm{ddiag}\left(\mathbf{W}^{H}\mathbf{R}_{k}^{H}\mathbf{W}\mathbf{Z}^{r}\right)\mathrm{ddiag}\left(\mathbf{Z}^{-r}\mathbf{W}^{H}\mathbf{R}_{k}\mathbf{W}\right)\right]\right) \quad (0.167)$$
$$\text{s.t. } \mathbf{W}^{H}\mathbf{W}=\mathbf{I}$$

The gradient for the objective function shown in (4.48) is given by:

$$\mathbf{D}_{U}=2\left(\mathbf{R}_{k}^{H}\mathbf{R}_{k}\mathbf{W}+2\mathbf{R}_{k}\mathbf{R}_{k}^{H}\mathbf{W}\right)$$
$$-2\sum_{r=-B}^{B}\left(\mathbf{R}_{k}^{H}\mathbf{V}_{r}\mathrm{ddiag}(\mathbf{V}_{r}^{H}\mathbf{R}_{k}\mathbf{W})+\mathbf{R}_{k}\mathbf{V}_{r}\mathrm{ddiag}(\mathbf{W}^{H}\mathbf{R}_{k}^{H}\mathbf{V}_{r})\right) \quad (0.168)$$

CHAPTER 5 EVALUATION OF DPS SIGNALING WAVEFORM: RECEIVER AND TRANSMITTER ASPECTS

The choice of a signaling waveform has consequences on the overall performance of a communication system as well as the complexity of the processing operations involved. In general, a tradeoff relationship exists between complexity and performance. Complexity manifests in a number of factors that have a tradeoff relationship amongst themselves. The same is true for performance metrics which can be traded for one another.

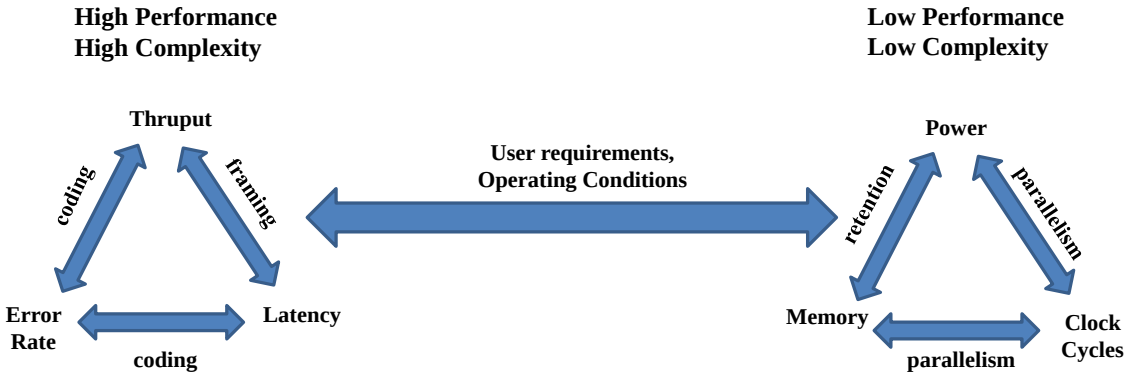

Figure 43: Overall Communication System Performance-Complexity Tradeoff

Figure 43 shows the system level performance-complexity tradeoff involving the different parameters of a communication system. However, this tradeoff can be applied on a smaller scale to the individual building blocks that exist in the transmitter and receiver.

The focus of this chapter will be the evaluation of the DPS waveform in terms of its impact on the performance-complexity tradeoff aspect for the different receiver and transmitter function blocks.

5.1 Channel Estimation Accuracy vs. Minimal Pilot Usage Tradeoff: Data-to-Pilot Isolation

Pilot-aided channel estimation in the context of OFDM signaling operating in DD channels was presented in Chapter 2. Due to dispersion, channel estimation pilots are contaminated by neighboring data symbols which compromises the accuracy of the channel estimate. The interference caused by data leakage appears as the second term in (2.67), Section 2.5.2, Chapter 2. The dispersion spread is reflected in the equivalent channel matrix by the width of the diagonal band about the main diagonal. In OFDM, the pilot tones are surrounded by a guard region of width equal to the nominal width of the diagonal band, $2\upsilon_{\max}$ (maximum normalized Doppler) of the equivalent channel matrix, in order to contain the contamination due to neighboring data. However, the off-band diagonals (diagonals excluding the central diagonal band) are not insignificant and decay slowly, thus causing their influence to extend outside the guard zone in the form of Inter-Symbol Interference (ISI). The *off-band slowly decaying* ISI is a result of specular channel components with fractional Doppler frequencies relative to the subcarrier spacing as indicated by (4.38) in Chapter 4. For single carrier the time domain channel matrix exhibits the same behavior due to specular channel components with fractional delays relative to the sampling period as indicated by (4.39).

In contrast, when DPS basis signaling is used the equivalent channel matrix exhibits rapid off-band diagonal decay resulting in reduced ISI.

5.1.2 Pulse-shaped OFDM using primary DPS pulse shape

Applying pulse shaping is effective in improving off-band diagonal decay but this comes at the expense of losing orthogonality between the pulse-shaped subcarriers which is detrimental to numerical stability. In [45], it was found that using the primary component (corresponding to the largest eigenvalue) of the DPS basis for pulse shaping resulted in

improved off-band diagonal decay, due to the optimal confinement property of DPS, in addition to preserving approximate orthogonality.

Denoting the primary pulse shape by $\mathbf{s}_1$ (the first column of the DPS basis matrix $\mathbf{S}$) and the signaling basis by $\mathbf{O} = D(\mathbf{s}_1)\mathbf{F}$ when incorporated into the component matrix expression given by (4.35) in Section 4.8.1, Chapter 4 we get:

$$\begin{aligned}\mathbf{M}_{l,m} &= \left(\mathbf{D}(\mathbf{s}_1)\mathbf{F}\right)^H \mathbf{D}(\upsilon_l)\mathbf{F}^H\mathbf{D}(\tau_m)\mathbf{F}\mathbf{D}(\mathbf{s}_1)\mathbf{F} \\ &= \mathbf{F}^H\mathbf{D}(\mathbf{s}_1)^H \mathbf{D}(\upsilon_l)\mathbf{F}^H\mathbf{D}(\tau_m)\mathbf{F}\mathbf{D}(\mathbf{s}_1)\mathbf{F} \\ &= \underbrace{\mathbf{F}^H\mathbf{D}(\mathbf{s}_1)\mathbf{D}(\upsilon_l)\mathbf{F}^H}_{\psi_{\mathbf{s}_1}(\upsilon_l)}\mathbf{D}(\tau_m)\mathbf{F}\mathbf{D}(\mathbf{s}_1)\mathbf{F}\end{aligned} \tag{0.169}$$

where $\mathbf{D}(.)$ generates a diagonal matrix from its vector argument.

By the approximate orthogonality property, the third factor is approximated by $\mathbf{F}\mathbf{D}(\mathbf{s}_1)\mathbf{F} \approx \mathbf{I}$ and (5.1) becomes:

$$\mathbf{M}_{l,m} \approx \underbrace{\mathbf{F}^H\mathbf{D}(\mathbf{s}_1)\mathbf{D}(\upsilon_l)\mathbf{F}^H}_{\psi_{\mathbf{s}_1}(\upsilon_l)}\mathbf{D}(\tau_m) \tag{0.170}$$

Equation (5.2) shows a form similar to that in (4.38) with the factor $\psi_{\mathbf{s}_1}(\upsilon_l)$ equal to the DFT of the DPS vector $\mathbf{s}_1$ as a function of diagonal locations $(k-l)$:

$$\psi_{\mathbf{s}_1}(\upsilon_l) = \sum_{n=0}^{N-1} s(n)e^{j2\pi(k-l+\upsilon_l)n/N} \tag{0.171}$$

Thus, $\mathbf{s}_1$ is the optimal window shape in terms of band confinement.

Using $\mathbf{s}_1$ pulse shaping despite being optimal does not have the same rapid out of band decay as the DPS basis.

5.1.3 Pilot Patterns

Channel estimation can be valid for a frame consisting of multiple consecutive blocks when the parameters τ_j, υ_i of the specular channel components do not vary over the period of a frame.

For a frame consisting of R consecutive blocks, the input-output relationship is given by:

$$\mathbf{z}[r] = \mathbf{O}^H \mathbf{H}_{\mathbf{t}}[r]\mathbf{O}\mathbf{x}[r] + \mathbf{O}^H \mathbf{n}[r] \text{ for } r = 0,...,R-1 \qquad (0.172)$$

where:

$\mathbf{H}_{\mathbf{t}}[r] = \left(\boldsymbol{H}[r] \circ \mathbf{F}^H\right)\mathbf{F}$, $\boldsymbol{H}[r] = \sum_{l=0}^{L-1}\sum_{m=0}^{M-1} \gamma_{l,m} \boldsymbol{\upsilon}_l[r] \boldsymbol{\tau}_m^H$, and $[\boldsymbol{\upsilon}_l]_n = e^{-j2\pi\upsilon_l((r-1)N+n)/N_t}$ for n=0,…,N-1.

The choice of the pilot pattern is dependent on the type of signaling used. Within the context of ONB signaling discussed in the previous chapter, the signaling ONB determines the pilot arrangement used.

Multi-Kronecker Delta (MKD) is the standard pilot pattern used for both OFDM, $\mathbf{O} = \mathbf{F}$, and SC, $\mathbf{O} = \mathbf{I}$, in DD channels, and consists of multiple Kronecker Delta (KD) pilot clusters placed uniformly across a single block. Each KD pilot cluster has the form $\mathbf{c}^T = [0^T_{(c-1)/2}, 1, 0^T_{(c-1)/2}]$, c being the size of the cluster, enclosed by $g/2$ guards on each side to control the ISI contamination.

A more frugal pilot pattern, i.e. less wasteful in terms of pilot resources, is the Single Kronecker Delta (SKD) which uses only one pilot cluster per block. This is made possible when the channel estimation is done based on a multi-block frame.

MKD Pilot Pattern

For MKD, M pilot clusters are placed uniformly across a block and the positions are identical for all blocks in the frame. The set of pilot locations in the r^{th} block is given by (5.5) which is independent of r:

$$O_r := \{ m\lfloor N/M \rfloor + i,\ i = 0,..,c-1,\ m = 0,..,M-1 \} \tag{0.173}$$

where M is the number of clusters per block.

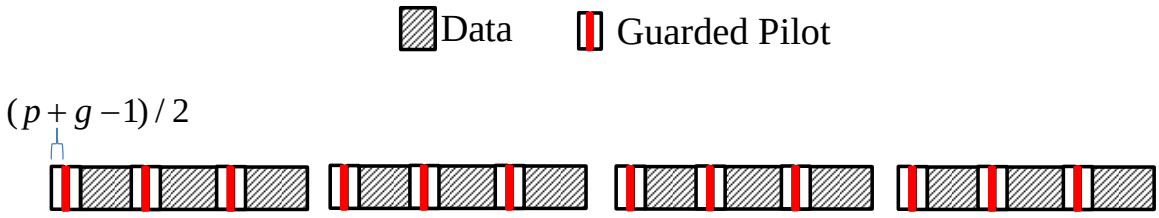

Figure 44: MKD Pilot Arrangement consisting of *M*=3 Uniformly Spaced Pilot Clusters over a Frame of 4 Symbols.

SKD Pilot Pattern

For SKD, a single pilot cluster is placed in each block which is less wasteful in pilot resources but also less robust to ill-conditioning due to improper pilot placement. Two variations of the SKD placement are used:

1) SKD-U: To use a single pilot cluster per block when $\mathbf{O = I}$ or $\mathbf{O = F}$ signaling ONBs are used, the cluster placement must be different across blocks. The set of pilot locations in the r-th block is given by:

$$O_r := \{ (r-1)\lfloor N/R \rfloor + i,\ i = 0,...,c-1 \} \tag{0.174}$$

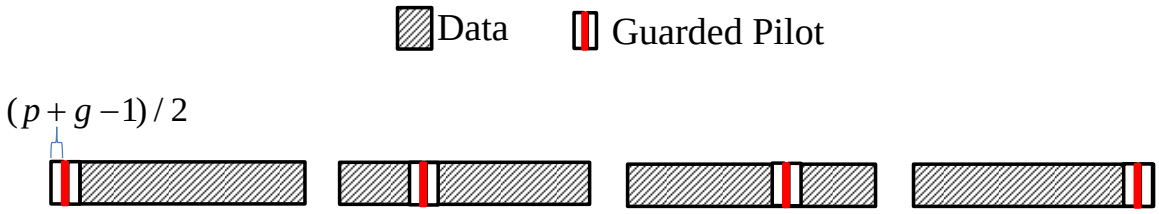

Figure 45: SKD-U Pilot Arrangement Spread over a Frame of 4 Symbols.

2) SKD-E (Edge): For DPS signaling, $\mathbf{O}=\mathbf{S}$, pilot clusters can be placed in the same location in all blocks. This makes it possible to take advantage of the narrow bandwidth of the equivalent channel matrix in the case of DPS signaling. The set of pilot locations is independent of the block index r and is given by:

$$O_r := \{e+i,\ i=0,...,c-1\} \tag{0.175}$$

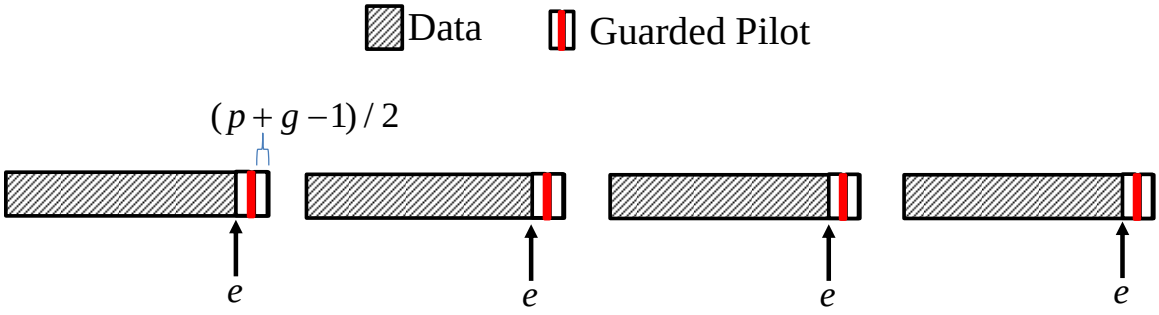

Figure 46: SKD-E Pilot Arrangement with Cluster Edge Location e.

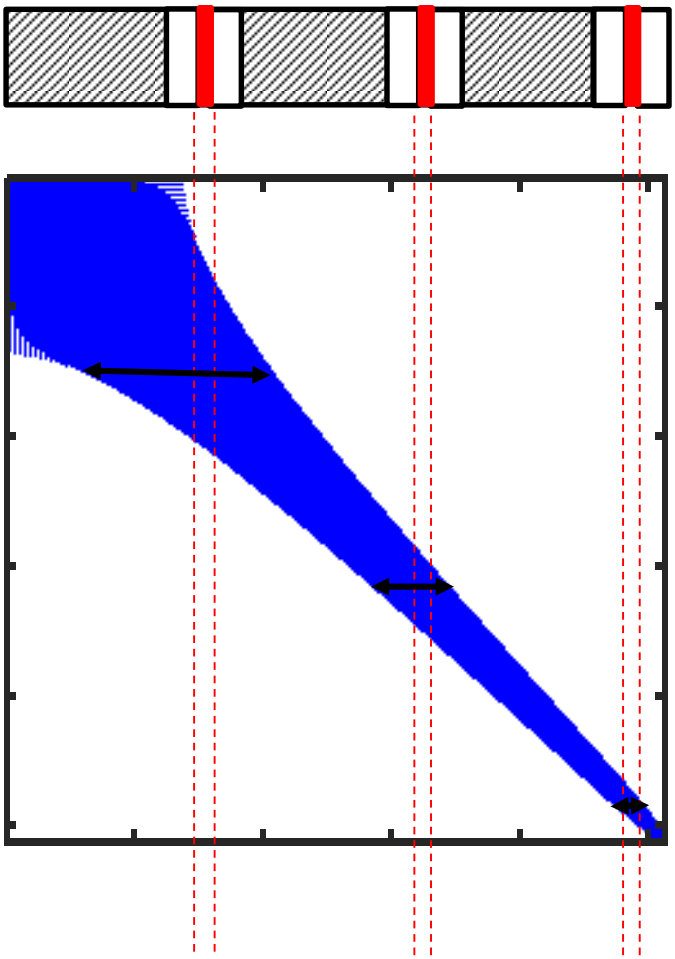

Figure 47: $\mathbf{O} = \mathbf{S}$ Channel Matrix Structure Showing Susceptibility of Different Pilot Locations to Data Contamination According to the Local Band Width of the Matrix Indicated by Double Arrows.

The impact of the choice of pilot location on the data-to-pilot contamination is determined by the equivalent channel matrix. For ONBs $\mathbf{O}=\mathbf{I}$ $\mathbf{O} = \mathbf{I}$, $\mathbf{O} = \mathbf{F}$, and approximate τ ONB $\mathbf{O}=D(\mathbf{s}_1)\mathbf{F}$ $\mathbf{O} = D(\mathbf{s}_1)\mathbf{F}$ the band width is uniform across all column locations. However, for $\mathbf{O} = \mathbf{S}$ the band width narrows monotonically for column locations farther to the right. Figure 47 shows the extent of data symbols, depicted by double arrows, that contribute to pilot contamination for different pilot locations.

5.1.4 BEM based LS Estimation

The specular channel model given in (4.4), Section 4.1, Chapter 4 is given in matrix form as follows:

$$\boldsymbol{H} = \sum_{l=0}^{L-1} \gamma_l \upsilon_l \boldsymbol{\tau}_l^H = \mathbf{N}\boldsymbol{\Gamma}\mathbf{T}^H \tag{0.176}$$

where $\mathbf{N} = [\upsilon_l, .., \upsilon_{L-1}]$, $\mathbf{T} = [\boldsymbol{\tau}_0, .., \boldsymbol{\tau}_{L-1}]$ and $[\boldsymbol{\Gamma}]_{l,k(\tau_l)} = \gamma_l$ with $\upsilon_l \le \upsilon_{l+1}$ and $k(\tau_l) \ge k(\tau_k)$ for $\tau_l \ge \tau_k$.

The construction of the matrix $\boldsymbol{H}$ from the specular Doppler-Delay components is given by Fig. 47.

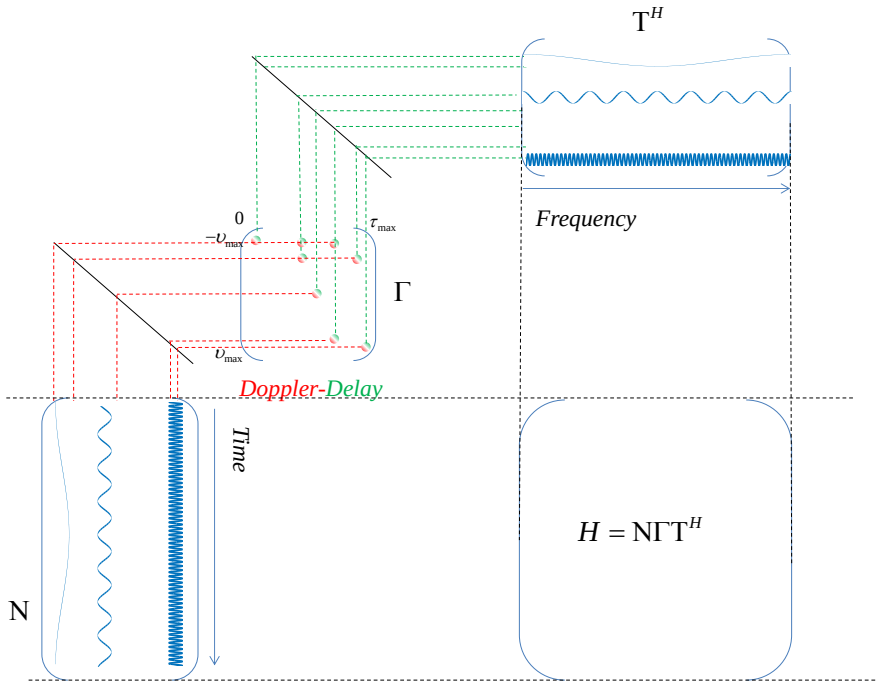

Figure 48: Synthesis of Time-varying Transfer Function *H* from Specular Components in Matrix Γ

When the coordinates of the Delay-Doppler components are not known, the matrices $\mathbf{N}$ and $\mathbf{T}$ in (5.8) are replaced by oversampled uniform DFT matrices $\tilde{\mathbf{N}}$, $\tilde{\mathbf{T}}$, and $\tilde{\boldsymbol{\Gamma}}$, with dimensions $NR \times NR\upsilon_{\max}$ $NR \times NR\upsilon_{\max}$, $N \times NR\tau_{\max}$, and $NR\upsilon_{\max} \times NR\tau_{\max}$ respectively. Substituting into (5.4), dropping the noise term, we get after some algebraic manipulation:

$$\begin{aligned}\mathbf{z}[r] &= \mathbf{O}^H \boldsymbol{\varphi}_t[r]\left(\mathbf{I}_{|\Gamma|}\otimes\mathbf{F}^H\right)\boldsymbol{\varphi}_f\left(\mathbf{I}_{|\Gamma|}\otimes\mathbf{F}\right)\left(\mathbf{I}_{|\Gamma|}\otimes\mathbf{O}\mathbf{x}\right)\bar{\boldsymbol{\gamma}} \\ &= \mathbf{O}^H \boldsymbol{\varphi}_t[r]\bar{\bar{\mathbf{F}}}^H \boldsymbol{\varphi}_f \bar{\bar{\mathbf{F}}}\bar{\bar{\mathbf{O}}}\bar{\mathbf{x}}_p\bar{\boldsymbol{\gamma}}\end{aligned} \tag{0.177}$$

where

$$\boldsymbol{\varphi}^t[r] = \mathrm{diag}\left(\mathbf{I}_{NR\tau_{\max}}\otimes\left[\tilde{\upsilon}_1[r]^H,...,\tilde{\upsilon}_{NR\upsilon_{\max}}[r]^H\right]^H\right),\qquad \left[\tilde{\mathbf{N}}\right]_{n,k} = e^{-j2\pi nk/(NR)},\qquad \tilde{\gamma}_{i,j} = [\Gamma]_{i,j},$$

$$\boldsymbol{\varphi}^f = \mathrm{diag}\left(\left[\mathbf{1}^H_{NR\upsilon_{\max}}\otimes\tilde{\boldsymbol{\tau}}_1{}^H,...,\mathbf{1}^H_{NR\upsilon_{\max}}\otimes\tilde{\boldsymbol{\tau}}_{NR\tau_{\max}}{}^H\right]^H\right),\qquad \bar{\boldsymbol{\gamma}} = \left[\tilde{\gamma}_{1,1},...,\tilde{\gamma}_{1,NR\tau_{\max}},....,\tilde{\gamma}_{NR\upsilon_{\max},NR\tau_{\max}}\right]^H$$

and $\left[\tilde{\mathbf{T}}\right]_{n,k} = e^{-j2\pi nk/(NR)}$.

Partitioning the input vector into exclusive data and pilot vectors, $\mathbf{x} = \mathbf{x}_p + \mathbf{x}_d$, and selecting indices in the set $\mathcal{O}_r$:

$$\mathbf{z}[r]^{(\mathcal{O}_r)} = \mathbf{O}^{H(\mathcal{O}_r)}\boldsymbol{\varphi}_t[r]\bar{\bar{\mathbf{F}}}^H \boldsymbol{\varphi}_f \bar{\bar{\mathbf{F}}}\bar{\bar{\mathbf{O}}}\bar{\mathbf{x}}_p\bar{\boldsymbol{\gamma}} + \boldsymbol{\varepsilon} \tag{0.178}$$

where $\boldsymbol{\varepsilon} = \mathbf{O}^{H(\mathcal{O}_r)}\boldsymbol{\varphi}_t[r]\bar{\bar{\mathbf{F}}}^H \boldsymbol{\varphi}_f \bar{\bar{\mathbf{F}}}\bar{\bar{\mathbf{O}}}\bar{\mathbf{x}}_d\bar{\boldsymbol{\gamma}}$ representing data-to-pilot contamination.

Stacking the observations from R symbols:

$$\bar{\mathbf{z}} = \boldsymbol{\psi}\bar{\bar{\mathbf{F}}}^H \boldsymbol{\varphi}_f \bar{\bar{\mathbf{F}}}\bar{\bar{\mathbf{O}}}\bar{\mathbf{x}}_p\bar{\boldsymbol{\gamma}} + \bar{\mathbf{n}} \tag{0.179}$$

where

$$\boldsymbol{\psi} = \left[\left(\mathbf{O}^{H(O_r)}\boldsymbol{\varphi}_t[r]\right)^H,...,\left(\mathbf{O}^{H(O_r)}\boldsymbol{\varphi}_t[R]\right)^H\right]^H,\quad \bar{\mathbf{z}} = \left[\mathbf{z}[1]^{(O_1)H},...,\mathbf{z}[R]^{(O_R)H}\right]^H$$

leads finally to the LS estimate for the channel BEM coefficients given by:

$$\tilde{\bar{\gamma}} = \left(\boldsymbol{\psi} \overline{\overline{\mathbf{F}}}^{H} \boldsymbol{\varphi}_f \overline{\overline{\overline{\mathbf{F}\mathbf{O}\mathbf{x}_p}}} \right)^{\dagger} \bar{\mathbf{z}} \tag{0.180}$$

5.1.5 Simulation Results

Simulation experiments consist of transmissions using the four signaling bases: $\mathbf{O} = \mathbf{I}$, $\mathbf{O} = \mathbf{F}$, $\mathbf{O} = \mathbf{D}(\mathbf{s}_1)\mathbf{F}$, and $\mathbf{O} = \mathbf{S}$, modulated by QPSK symbol blocks across 1000 DD channel realizations and using the pilot symbol for LS estimation of the channel coefficients. For simplicity, the following assumption is made:

Assumption1 (Oracle Knowledge): The channel coefficient matrix $\tilde{\boldsymbol{\Gamma}}$ is sparse with only a subset (indices considered known) of its elements non-zero.

Using Assumption 1 does not affect the validity of the results since techniques exist, such as Lasso [46] that can exploit sparsity to attain performance close to that of Oracle knowledge.

The channel estimation performance is evaluated using the metric of Normalized Mean Square Error (NMSE) averaged over the DD channel generated according to a 2-D OCE-BEM dictionary having the following parameters:

- $N = 256$
- $\upsilon_{\max} = 0.004$
- $\tau_{\max} = 0.015$
- Number of blocks per frame $R = 8$
- Sparsity order $|\boldsymbol{\Gamma}| = 12$
- SKD-E pilot location $e = 200$
- MKD $M = 4$ clusters per symbol.

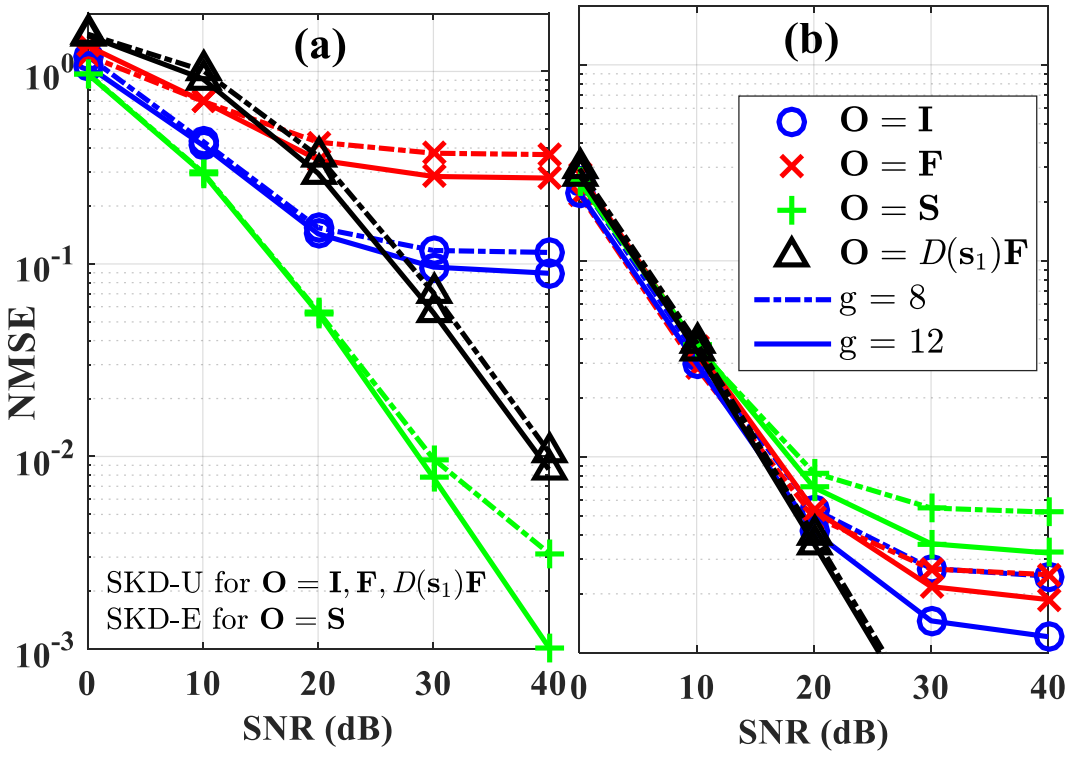

Figure 49: NMSE vs SNR (a) SKD-U, SKD-E, (b) MKD

Figure 49 shows the channel estimation NMSE for SNR values over the range 0-40dB. For the SKD-U and SKD-E pilot schemes, as SNR increases, the data-to-pilot contamination effect starts to become prominent. An error floor is quickly reached for ONBs $\mathbf{F}$ and $\mathbf{I}$ but not for $\mathbf{D}(\mathbf{s}_1)\mathbf{F}$ (floor arises at higher SNRs) and $\mathbf{S}$ due to the good isolation of pilots. Increasing the guard zone width only reduces the error floor marginally, except when using $\mathbf{S}$ due to the rapid decay of ISI. Another performance determining factor, in addition to data-to-pilot isolation, is the pilot arrangement as it impacts the coherence (ill-conditioning) of the channel coefficient estimation matrices (varies across realizations due to the sparsity and oracle knowledge). Over the realizations used, the conditioning of the matrices for $\mathbf{S}$ is better than for $\mathbf{D}(\mathbf{s}_1)\mathbf{F}$, thus suggesting that a frugal pilot scheme is more suitable for DPS signaling compared to $\mathbf{D}(\mathbf{s}_1)\mathbf{F}$.

For MKD, the NMSE error floor due to ISI for ONBs $\mathbf{F}$ and $\mathbf{I}$ is significantly lowered compared to SKD due to the higher power (lower interference-to-signal ratio) that comes

with using multiple clusters. For MKD with ONB $\mathbf{S}$, a limiting error floor arises due to the dominance of high interference on pilots placed away from the edge .

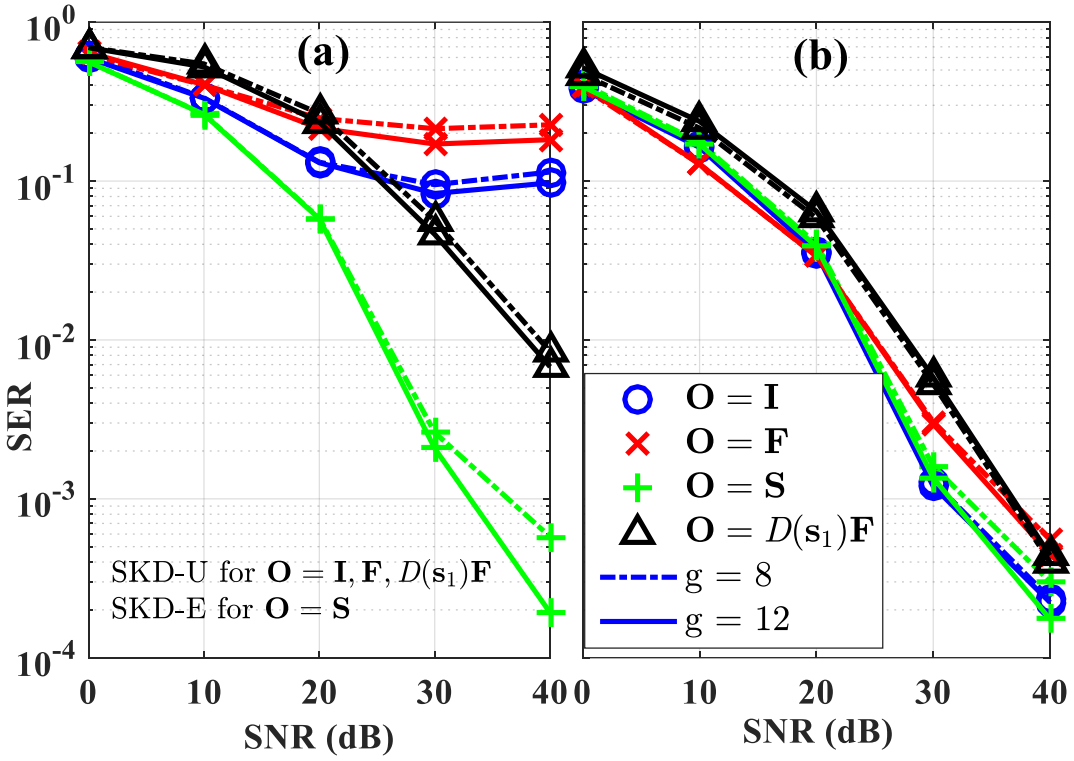

Figure 50: SER vs SNR (a) SKD-U and SKD-E, (b) MKD

Figure 49 shows that the resulting SER performance is in agreement with the NMSE performance in Fig. 48. For MKD, a significant reduction in SER is obtained for $\mathbf{I}$, $\mathbf{F}$, and $\mathbf{D}(\mathbf{s}_1)\mathbf{F}$ as a result of improvement in channel estimation NMSE. However, despite $\mathbf{D}(\mathbf{s}_1)\mathbf{F}$ having the lowest NMSE at high SNRs, its corresponding SER is not the lowest. At high SNRs, the conditioning of the equivalent per-symbol channel matrices, which depend on the capacity of the channel ensemble for the given parameters $\upsilon_{\max}, \tau_{\max}$, becomes the dominant factor in impacting SER performance as opposed to channel NMSE. Thus, the SER improvement attained by using more pilots can be obtained when using fewer pilots with $\mathbf{S}$ as the signaling ONB.

5.2 SER Performance vs. Equalization Complexity Tradeoff

In TI channels OFDM has the advantageous property of being a universal diagonalizer for the equivalent channel matrix over all possible realizations given an adequate CP length is used. This property facilitates low complexity single tap equalization which is one of the reasons of OFDMs superiority over other signaling schemes. In doubly dispersive channels this property of OFDM is lost. In fact, no signaling scheme exists [47] that has the universal diagonalizer property due to the absence of a common set of eigenfunctions for Doubly Dispersive channel realizations.

The lack of diagonal structure in the equivalent channel matrix for both OFDM and SC in Doubly Dispersive (DD) channels translates to an increase in the computational complexity of the equalization step due to the non-trivial matrix inversion. However, since the matrix is not full but approximately banded considerable savings in computational complexity can be attained by exploiting this structure. Operations involving diagonally banded matrices have a computational complexity comparable to that of a full matrix with row or column dimension equal to the width of the matrix band. In [25, 48, 49] the inverse of the ICI affected OFDM channel matrix after truncation to its diagonal band $[-Q, Q]$ was found to be a suitable equalizer with complexity linear in the number of subcarriers, i.e. $O(NQ^2)$. The parameter Q controls the Residual Inter-Component Interference (R-ICI) after equalization at the expense of additional complexity. The rate of reduction in R-ICI with Q is dependent on the decay rate of the out-of-band diagonals which in turn is determined by the choice of signaling waveform. A slow sinc function decay is a well-known characteristic of strictly time-limited block transmissions (rectangular pulse shape) which can be alleviated by pulse shaping (windowing) the transmitted signal [50]. Alternatively [26], a window is applied to the received signal that is specifically tailored to the channel statistics which are then assumed to be known a priori.

Discrete Prolate Spheroidal Sequences exhibit quasi-orthogonality in doubly dispersive channels. The resulting equivalent channel matrix attains a banded structure with rapid out-of-band decay compared to that obtained from Gabor Frames using windows of duration

equal to the symbol period. This rapid decay property allows elements outside an appropriately chosen diagonal band of the matrix to be considered negligible, thereby facilitating computational savings with minimal loss in performance.

5.2.1 Equalization using inverse of banded approximation

The degree of bandedness of a matrix enables low complexity equalization using an incomplete version of the matrix, the diagonal band, without incurring considerable loss in performance. One such equalizer is the MMSE-BLE equalizer described in [25]. The strictly banded version of the channel matrix $\tilde{\mathbf{H}} = \mathbf{T}[Q] \circ \mathbf{H}$ is obtained through multiplication with the mask $\left[\mathbf{T}(Q)\right]_{i,j} \neq 0$ for $|i-j| < Q$ giving the equalizer:

$$\mathbf{G} = (\tilde{\mathbf{H}}^H \tilde{\mathbf{H}} + \gamma^{-1}\mathbf{I}_N)^{-1}\tilde{\mathbf{H}}^H \tag{0.181}$$

Obtaining $\mathbf{G}$ involves inversion of a matrix with half band width $2Q$. The key step to reducing the equalization complexity is through $\mathbf{LDL}^H$ decomposition, which involves the sequence of steps laid out in the first column of Table 3, with the corresponding complexity given in the second column.

Table 4: Complexity Analysis of steps involved in Equalization

Equalization Step	Number of Operations
$(\tilde{\mathbf{H}}^H \tilde{\mathbf{H}} + \gamma^{-1}\mathbf{I}_N)$	$N(2Q^2 + 3Q + 1)$
$\mathbf{LDL}^H$	$N(2Q^2 + 5Q)$
$\hat{\mathbf{y}} = \mathbf{L}^{-1}\mathbf{y}$	$2QN$
$\hat{\mathbf{x}} = \mathbf{L}^{-H}\mathbf{y}$	$2QN$
$\mathbf{x} = \Lambda^H \hat{\mathbf{x}}$	$(2Q+1)N$

For the DPS basis, an additional computational cost is incurred in the conversion of the received signal from the time domain to the basis domain which is N^2 compared to $N \log_2 N$ in the case of OFDM. Figure 51 shows a comparison of the total computational complexity for window processing and DPS basis selection.

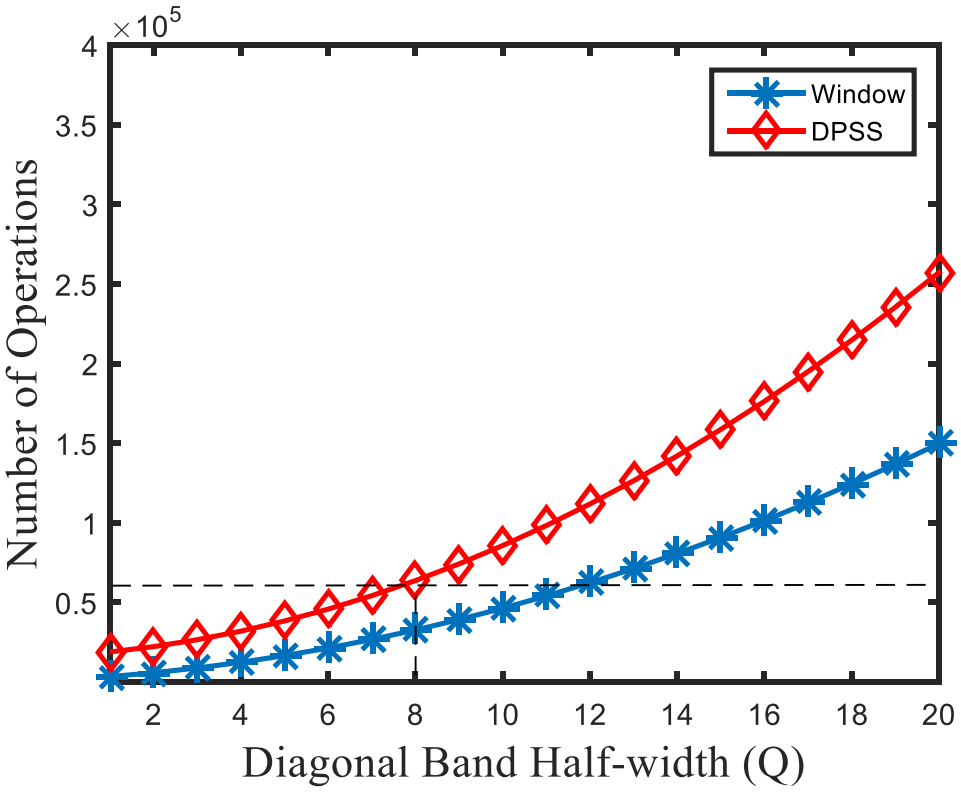

Figure 51: Equalization complexity vs. half width of banded approximation

From a complexity standpoint DPS signaling is at a disadvantage. In severe Doubly Dispersive conditions, the typical range of half band widths used in the banded approximation to yield acceptable performance and significant complexity savings compared to the full matrix is $Q = 8 - 12$. Within this range, DPS complexity is comparable to that of OFDM, as shown in Fig. 51. However, as will be shown in the following section the SER performance of DPS exceeds that of OFDM and other bases by orders of magnitude for the same choice of Q.

5.2.2 Simulation Results

The performance of the equalizer is evaluated in terms of the Symbol Error Rate (SER) for a QPSK signal block of size $N = 256$ through simulation over 1000 channel realizations with the following parameters: maximum normalized frequency spread $\upsilon_{\max} = 0.004$ and delay spread $\tau_{\max} = 0.015$. Note that the chosen frequency dispersion parameter corresponds to the severe time-varying channel conditions that are representative of prospective scenarios of operation involving frequencies as high as 60 GHz and speeds of 500 km/h.

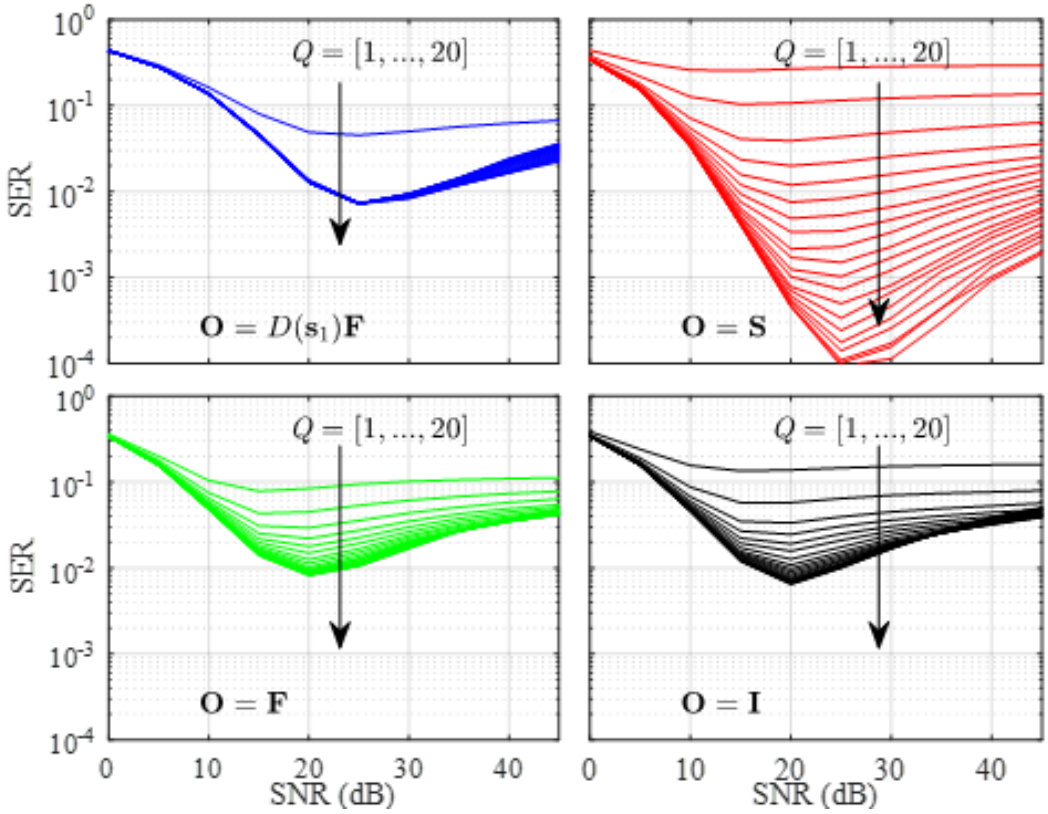

Figure 52: SER versus SNR performance across different values of the band width parameter $Q = 1, \cdots, 20$

Figure 52 shows the SER versus SNR for different half band widths of the banded approximation. For all bases, the general trend is a reduction in the SER floor with an increase in Q, with the difference between bases being the rate of reduction. For bases $\mathbf{O} = \mathbf{F}$ and $\mathbf{O} = \mathbf{I}$, the rate of reduction in the SER floor level steadily decreases until a

point of saturation is reached where the SER level settles at ~10^{-2}. For $\mathbf{O} = \mathbf{D}(\mathbf{s}_1)\mathbf{F}$, the rate of reduction of SER floor starts out very high but almost immediately thereafter SER saturates at a level of 10^{-2}. However, for $\mathbf{O} = \mathbf{S}$, there is no saturation in the rate of SER reduction with Q.

Note that all bases exhibit a remarkable increase in SER as SNR increases beyond the point when the SNR is $20\,\mathrm{dB}$. The latter phenomenon has been investigated by examining the condition number of the banded versions of the individual channel realizations. For the given channel parameters, a large percentage of channel realizations is ill-conditioned. In addition, the banded approximation appears to exacerbate the ill-conditioning if it were not for the regularizing term $\gamma^{-1}\mathbf{I}_N$ in (5.14). At high SNRs, the regularizing term vanishes, causing blow-up in the equalization output and a significant rise in the number of errors. This can be understood to be a characteristic property determined by the channel ensemble for the given parameters, reminiscent of the channel capacity in MIMO and its dependence on the conditioning of the MIMO channel matrix.

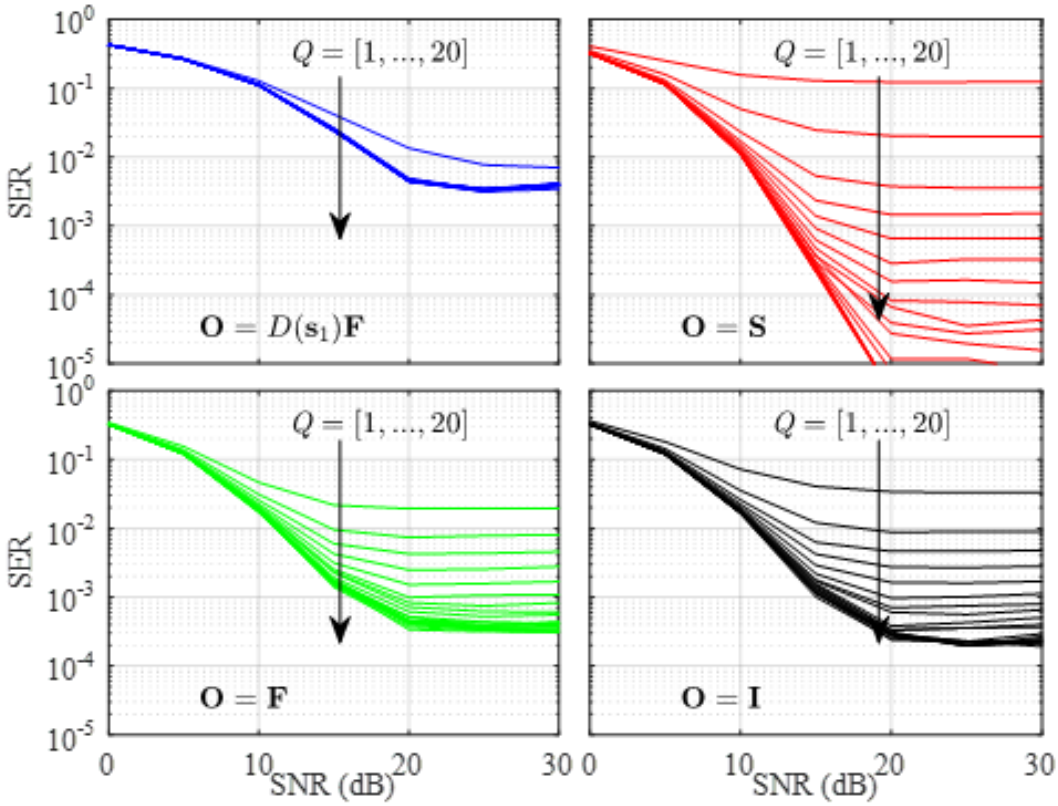

Figure 53: SER versus SNR performance across different values of the band width parameter $Q = 1, \cdots, 20$

Using a Single Input Multiple Output (SIMO) scheme the channel ill-conditioning effect can be alleviated. Figure 53 shows the SER performance for the same parameters as those for Fig. 49 but with 2 RX antennas where the channel and equalizer matrices are given by:

$$\begin{aligned} \mathbf{G} &= (\bar{\bar{\mathbf{H}}}\bar{\bar{\mathbf{H}}}^H + \gamma^{-1}\mathbf{I}_N)^{-1}\bar{\bar{\mathbf{H}}}^H \\ \bar{\bar{\mathbf{H}}} &= [\tilde{\mathbf{H}}_1^H \tilde{\mathbf{H}}_2^H]^H \end{aligned} \tag{0.182}$$

The increase in SER with SNR effect has been eliminated due to the improvement of the channel conditioning. Additional gains are a drop in SER saturation floor for bases $\mathbf{O} = \mathbf{F}$ and $\mathbf{O} = \mathbf{I}$, and an increase in the rate of SER drop versus SNR due to the diversity effect. On the other hand, no significant improvement is seen for $\mathbf{O} = \mathbf{D}(\mathbf{s}_1)\mathbf{F}$ with respect to the saturation of SER reduction with increase in Q as now it lags behind in performance compared to bases $\mathbf{F}$ and $\mathbf{I}$.

5.3 Summary

The choice of signaling basis plays a central role in defining the structure of the equivalent channel matrix. Using a (non-Gabor) DPS basis was shown to lead to rapid decay in the out-of-band elements of the equivalent channel matrix. This rapid decay property can be exploited in facilitating enhancement in the two core receiver functions.

First, an enhancement in channel estimation accuracy with minimal (frugal) use of pilot resources can be achieved. This is made possible by placing pilots in locations where the matrix diagonal band has the least width. Simulations show an order of magnitude better SER performance for DPS relative to other waveforms.

Second, a tradeoff between computational complexity and performance is made possible due to the rapid off-band decay, which – unlike signaling schemes based on the Gabor basis– leads to significant gains in SER improvement for banded approximations with half bands orders of magnitude smaller than the matrix size. In addition, the 2 RX antenna SIMO scheme used in alleviating the ill-conditioning of the banded channel matrix approximations is shown to be most effective with the DPS signaling scheme.

CHAPTER 6 DIRECTION OF VELOCITY DIVERSITY FOR RAPIDLY TIME VARYING CHANNELS

The characteristic signal impairing effect caused by RTV channels is Doppler spread. Roughly speaking, for values of the parameter $\upsilon_{\max} \times N < 0.1$ the effect of the channel is perceived as a ***Block Fading*** phenomenon where, at an average frequency proportional to $\upsilon_{\max}$, the channel gain level drops to null levels destroying an entire block of contiguous symbols. The length of the block is equal to the fade duration, which is inversely proportional to $\upsilon_{\max}$. For RTV channels, $\upsilon_{\max} \times N < 0.1$ and the "fading" view is no longer suitable since an individual symbol no longer experiences a constant/flat gain but instead the symbol pulse shape is altered multiplicatively. This situation is potentially more benign than block fading, since no full symbol is completely irrecoverable due to a multiplication by zero.

On the top of Fig. 53 the block fading case is shown where – when the channel gain falls below a certain detection threshold – the affected symbols are lost, which is not the case for the RTV channel shown in the bottom.

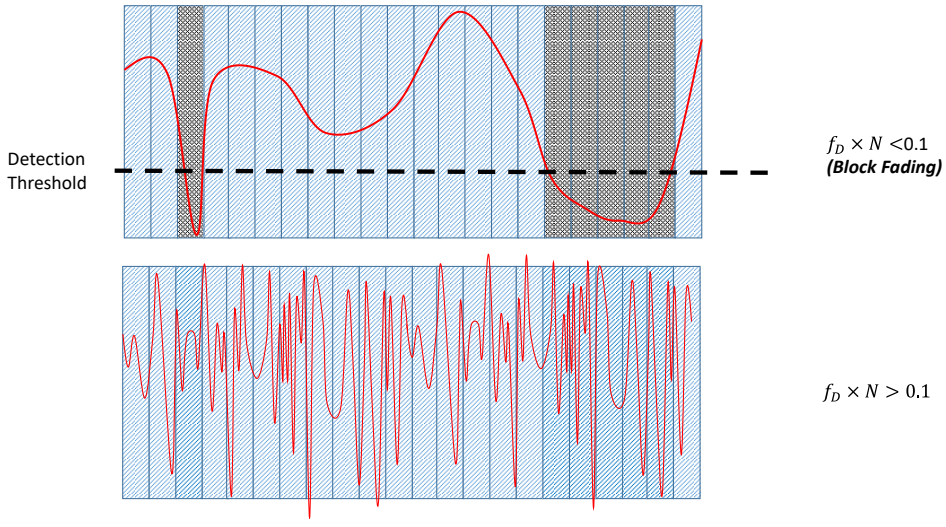

Figure 54: (Top) Block/Flat fading (Bottom) Multiple fades per symbol duration

As explained in previous chapters, a DD RTV channel acts on the pulse shape through a matrix (channel) vector (samples per symbol) product. Since the symbol pulse shape can be restored by inverting the matrix, an irrecoverable situation arises when the matrix is either singular or ill-conditioned.

In the block fading case, diversity techniques are used to reduce the probability of completely destroyed pulses by relying on multiple versions of a symbol, each affected by an independent channel. Similarly, such techniques can be used for the RTV case but with a different objective, which is to increase the chances of not having singular channel matrices.

In the following sections the principles of antenna array spatial sampling [51] [52] will be discussed, which will then serve as the foundation for a novel diversity method referred to as Direction of Velocity Diversity (DoVD).

6.1 Linear (1-D) space-sampling

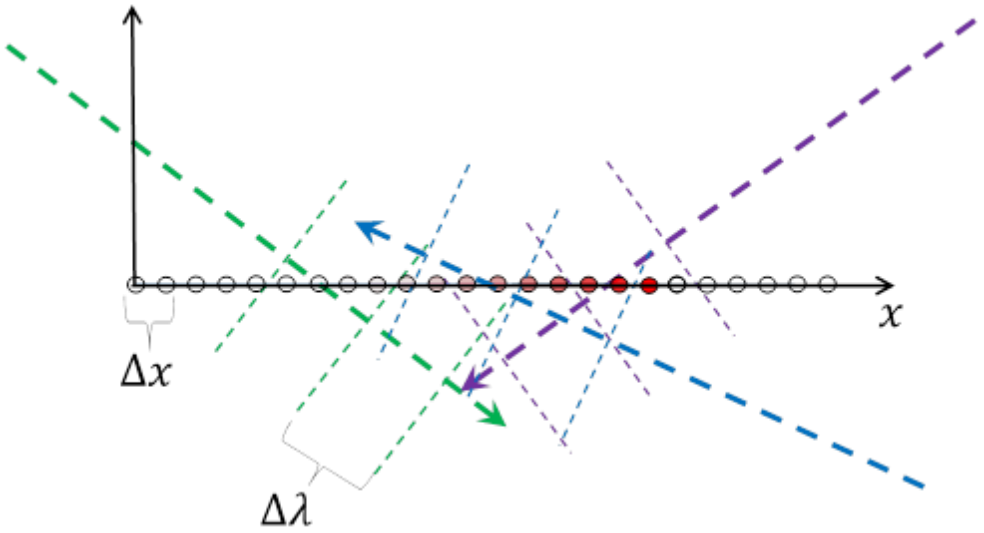

Figure 55: Linear spatial sampling of a multi-path signal

Figure 54 shows three waves impinging on a linear array. Space sampling occurs by scanning across the array elements simulating the effect of a physically moving sensor along the positive *x* axis where the fading red indicates the temporal scanning across the elements. As a result, a Doppler frequency shift will be induced in each wave component. To avoid spatial sampling aliasing the sensor spacing Δx, which corresponds to the spatial sampling interval, must be less than the wavelength λ. This guarantees that the channel Doppler is not undersampled.

However, another sampling condition is to not undersample the baseband signal which requires the spacing between the antenna elements to be:

$$\Delta x < \frac{2v_{scan}}{BW} \tag{0.183}$$

where v_{scan} is the scanning velocity across the array elements, and *BW* is the bandwidth of the baseband signal.

Thus, the antenna element spacing that guarantees no aliasing and thus the equivalent to a continuous time treatment is the following:

$$\Delta x < \min\left(\frac{2v_{scan}}{BW}, \lambda\right) \tag{0.184}$$

Focusing on the case of an OFDM signal and RTV channel condition $1 < \upsilon_{\max} \times N < 2$, where the channel exceeds 1 cycle of fluctuation over the OFDM symbol duration, the element spacing becomes determined mainly by the signal bandwidth, $BW = f_s$:

$$\Delta x < \frac{2v_{scan}}{f_s} \tag{0.185}$$

Using a plane wave model, the signal at the output of the antenna scanning commutator is given by:

$$y[n] = f\left(\frac{n\Delta x}{v_{scan}}\right)\sum_{l=0}^{P-1} e^{j(\omega\frac{n\Delta x}{v_{scan}} - \vec{k_l}.\overrightarrow{n\Delta x})} \tag{0.186}$$

where P is the number of multipath components clustered to appear with indiscernible delay separation.

It is important to note that the sampling occurs at the RF stage. A complication of this is aliasing interference from out-of-band signals, which can be addressed using pre-select RF filters after each antenna element before the commutator.

Even though subsampling the RF modulated signal will down-convert the baseband signal with no distortion, signal attenuation due the sinc droop can be a potential problem.

Dropping the carrier term and introducing the angle of arrival variable θ_l for the l-th path, , (6.4) becomes:

$$y[n] = f\left(\frac{n\Delta x}{v_{scan}}\right)\sum_{l=0}^{P-1} e^{-jn\frac{2\pi\Delta x}{\lambda}\cos(\theta_l)} \tag{0.187}$$

Based on (6.5), under the multiple Doppler cycles per symbol condition, a correspondence can be made between an individual symbol and its spatial span through which the antenna scans, as illustrated in Fig. 56. This visualization will be instrumental in the treatments to follow since it allows us to effectively replace all variables in time by their space equivalents, such as the parameter $\upsilon_{\max} \times N$ being replaced by its equivalent to λ_S (wavelengths per symbol).

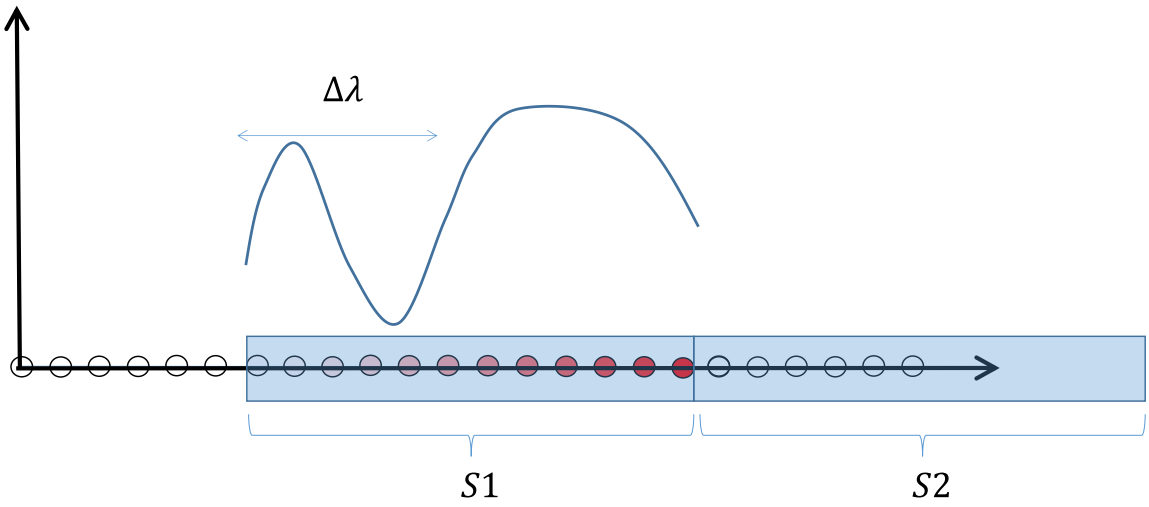

Figure 56: Time-to-space correspondence

6.2 Circular (2-D) space-sampling

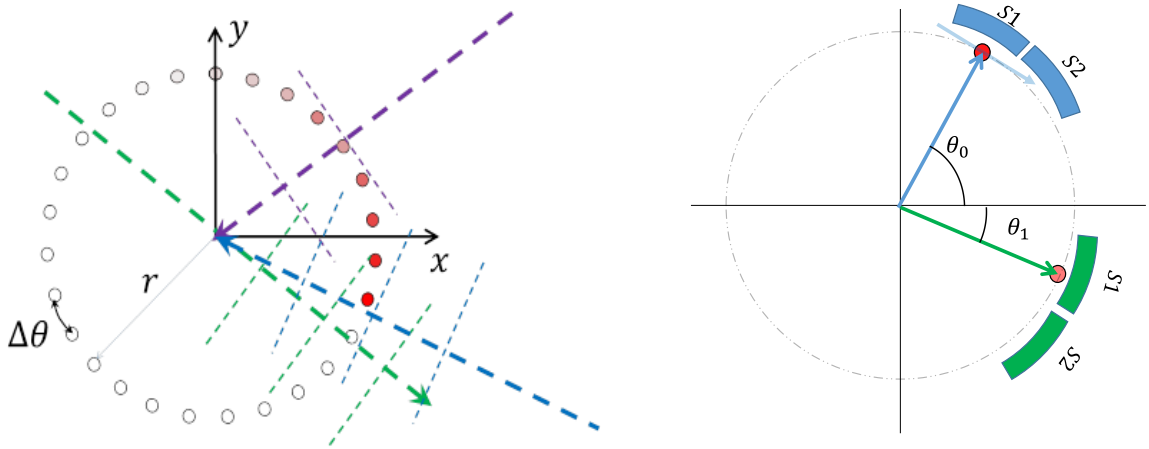

Figure 57: Circular Antenna Array Sampling

Placing the antenna sensors in a circular arrangement makes it possible to simulate continuous movement. For the symbol spatial span, scanning occurs over small arcs on the circular path which can be approximated by a linear tangential movement as illustrated on the right side of Fig. 57.

At a particular instant in time a certain symbol is being received at all antenna locations. Therefore, at the same time and at different angular locations θ_0 and θ_1, due to two antennas scanning commutators, the same symbol is being received but the channel effect is different as given by the following equations;

at angle θ_0:

$$y_0[n] = f\left(\frac{n\Delta x}{v_{scan}}\right)\sum_{l=0}^{P-1} e^{-jn\frac{2\pi\Delta x}{\lambda}\cos(\theta_l)} \tag{0.188}$$

at angle θ_1:

$$y_1[n] = f\left(\frac{n\Delta x}{v_{scan}}\right)\sum_{l=0}^{P-1} e^{-jn\frac{2\pi\Delta x}{\lambda}\cos(\theta_l+\theta_1-\theta_0)} \tag{0.189}$$

From (6.6) and (6.7) the different path components are adding with different phase angles resulting in different channel realizations that can potentially have different eigenvalue structures.

The results in Fig. 58 show the inverse channel condition (ICC) numbers for 100 independent 2-tap channel realizations when viewed at 2 different angles spaced by $\pi/6$.

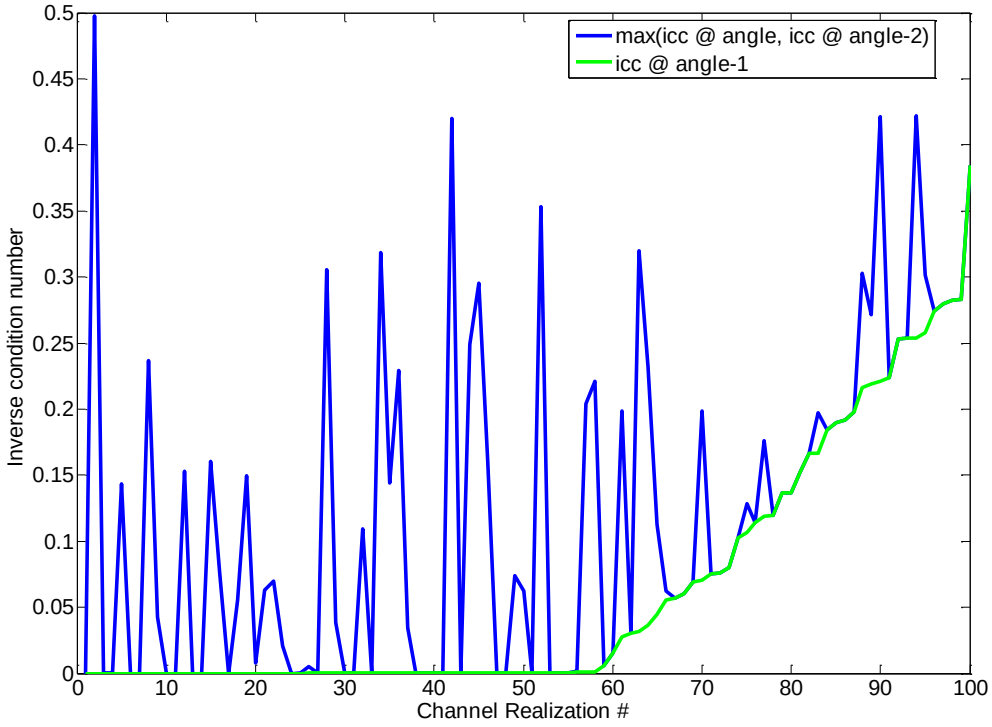

Figure 58: Inverse condition number for channel viewed at 2 different angles

The green trace represents the ICC number at a certain angle θ_0 arranged in ascending order. The blue trace is the maximum ICC number at angles θ_0 and $\theta_0 + \pi/3$ for the same realization. The left portion of the green trace corresponds to the single angular view of the channel which corresponds to very low ICC numbers, i.e. non-invertible matrices. For the same realizations, many of the channels at the second angular view are invertible. Hence the addition of the second angular view resulted in a diversity benefit. Adding more angular views can result in even more diversity gain.

CHAPTER 7 CONCLUSION AND FUTURE WORK

7.1 Conclusion

Most existing transceivers can be considered Fourier-centric where complex sinusoids play a central role in the internals of the core building blocks. From the channel perspective, complex sinusoids constitute the fundamental building blocks in the wireless baseband equivalent channel model; exemplified by the time-varying transfer function. In addition, complex sinusoids are used as signaling waveforms for data transmission through the channel.

The dominant mode of transmission in modern communications is in the form of finite length blocks having approximately finite bandwidth. As a result, the time-frequency space becomes projected to an essentially limited time and frequency subspace where complex sinusoids are no longer the signaling of choice due to their sensitivity to frequency dispersion. In addition, Kronecker delta signals (which are the duals of complex sinusoids) also suffer from the same vulnerability due to bandwidth limitations.

In the essentially limited time-frequency subspace, the DPS basis was found to be more compact in representing the channel behavior as compared to the DFT basis twhichdoes not achieve compactness due to the leakage effect. However, the same inadequacy due to leakage appears as increased ISI when the DFT basis is used for signaling. Using the DPS basis for signaling was shown to overcome the inadequacies of the DFT basis to a great extent. Thus, a new transceiver architecture was born where both the channel aspects as well as the signaling are DPS-based.

7.2 Future Work

Our proposed transceiver architecture has the DPS basis as its core component for most baseband functions. The DPS basis can also be of utility in understanding how the manipulation of the motion of an antenna can shape the behavior of the channel realizations.

A complete analysis of the diversity that results from changing the reference angle and how it relates to the DPS is still incomplete.

In addition, a study of the feasibility of the hardware RF aspects of the rotating antenna configuration needs to be conducted; such as the achievable switching speed of the RF switches relative to the platform velocity.

In Chapter 4, the DPS basis was shown to have a bandwedness advantage over Gabor signaling waveforms. This confirms the existence of a solution for the JABR optimization problem. The JABR problem being non-convex makes the search for the optimal solution highly dependent on the initial solution. Investigating the existence of solutions having higher bandedness compared to the DPS basis remains an intriguing prospect.

REFERENCES

[1] K. Said and A. L. Beex, "Per-symbol ICI mitigation for frequency non-selective time-varying channels," in *2015 IEEE International Symposium on Signal Processing and Information Technology (ISSPIT),* , 2015, pp. 449-453.

[2] K. Said and A. L. Beex, "Per-symbol ICI mitigation for low-dimensional doubly dispersive channels using pilot restoration," *2015 IEEE International Symposium on* in *Signal Processing and Information Technology (ISSPIT),* , 2015, pp. 460-465.

[3] D. Gabor, "Theory of communication. Part 1: The analysis of information," *Journal of the Institution of Electrical Engineers-Part III: Radio and Communication Engineering,* vol. 93, pp. 429-441, 1946.

[4] D. Slepian, "On bandwidth," *Proceedings of the IEEE,* vol. 64, pp. 292-300, 1976.

[5] G. Wunder, M. Kasparick, S. ten Brink, F. Schaich, T. Wild, I. Gaspar*, et al.*, "5GNOW: Challenging the LTE design paradigms of orthogonality and synchronicity," in *Vehicular Technology Conference (VTC Spring), 2013 IEEE 77th*, 2013, pp. 1-5.

[6] R. P. Ramachandran and P. Kabal, "Bandwidth efficient transmultiplexers. II. Subband complements and performance aspects,", *IEEE Transactions on Signal Processing,* vol. 40, pp. 1108-1121, 1992.

[7] G. Strang and T. Nguyen, *Wavelets and filter banks*: SIAM, 1996.

[8] Y.-P. Lin, S.-M. Phoong, and P. Vaidyanathan, *Filter bank transceivers for OFDM and DMT systems*: Cambridge University Press, 2010.

[9] M. Niedzwiecki, *Identification of time-varying processes*: Wiley New York, 2000.

[10] A. M. Sayeed and B. Aazhang, "Joint multipath-Doppler diversity in mobile wireless communications,", *IEEE Transactions on Communications,* vol. 47, pp. 123-132, 1999.

[11] L.-L. Lock, X. Kong, and R. J. Barton, "Simulation of time-varying, frequency-selective multipath fading channels for spread-spectrum waveforms," in *1999. Conference Record of the Thirty-Third Asilomar Conference on Signals, Systems, and Computers,* , 1999, pp. 1675-1679.

[12] L. Rugini, P. Banelli, R. C. Cannizzaro, and G. Leus, "Channel Estimation and Windowed DEF for OFDM with Doppler Spread," in *2006 IEEE International Conference on Acoustics, Speech and Signal Processing, 2006. ICASSP 2006 Proceedings.*, 2006, pp. IV-IV.

[13] A. P. Kannu and P. Schniter, "Design and analysis of MMSE pilot-aided cyclic-prefixed block transmissions for doubly selective channels," *IEEE Transactions on Signal Processing,* , vol. 56, pp. 1148-1160, 2008.

[14] D. Slepian, "Prolate spheroidal wave functions, Fourier analysis, and uncertainty—V: The discrete case," *Bell System Technical Journal,* vol. 57, pp. 1371-1430, 1978.

[15] T. Zemen and C. F. Mecklenbräuker, "Time-variant channel estimation using discrete prolate spheroidal sequences," *IEEE Transactions on Signal Processing,* vol. 53, pp. 3597-3607, 2005.
[16] D. Slepian, "Some comments on Fourier analysis, uncertainty and modeling," *SIAM review,* vol. 25, pp. 379-393, 1983.
[17] C. F. Mecklenbraüker, A. F. Molisch, J. Karedal, F. Tufvesson, A. Paier, L. Bernadó, *et al.*, "Vehicular channel characterization and its implications for wireless system design and performance," *Proceedings of the IEEE,* vol. 99, pp. 1189-1212, 2011.
[18] Z. Tang, R. C. Cannizzaro, G. Leus, and P. Banelli, "Pilot-assisted time-varying channel estimation for OFDM systems,", *IEEE Transactions on Signal Processing,* vol. 55, pp. 2226-2238, 2007.
[19] Y. R. Zheng and C. Xiao, "Simulation models with correct statistical properties for Rayleigh fading channels," *Communications, IEEE Transactions on,* vol. 51, pp. 920-928, 2003.
[20] H. Liu and G. B. Giannakis, "Deterministic approaches for blind equalization of time-varying channels with antenna arrays," *IEEE Transactions on Signal Processing,* vol. 46, pp. 3003-3013, 1998.
[21] C. E. Shannon, "A mathematical theory of communication," *ACM SIGMOBILE Mobile Computing and Communications Review,* vol. 5, pp. 3-55, 2001.
[22] I. Daubechies, *Ten lectures on wavelets*: SIAM, 1992.
[23] J. Benedetto, C. Heil, and D. Walnut, "Uncertainty principles for time-frequency operators," *Continuous and Discrete Fourier Transforms, Extension Problems and Wiener-Hopf Equations,* pp. 1-25, 1992.
[24] J. J. Benedetto, C. Heil, and D. F. Walnut, "Gabor systems and the Balian-Low theorem," in *Gabor analysis and algorithms*, ed: Springer, 1998, pp. 85-122.
[25] L. Rugini, P. Banelli, and G. Leus, "Low-complexity banded equalizers for OFDM systems in Doppler spread channels," *EURASIP Journal on Advances in Signal Processing,* vol. 2006, pp. 1-13, 2006.
[26] P. Schniter, "Low-complexity equalization of OFDM in doubly selective channels," *IEEE Transactions on Signal Processing,* vol. 52, pp. 1002-1011, 2004.
[27] G. Leus, "On the estimation of rapidly time-varying channels," in *Signal Processing Conference, 2004 12th European*, 2004, pp. 2227-2230.
[28] P. S. Rossi and R. R. Muller, "Slepian-based two-dimensional estimation of time-frequency variant MIMO-OFDM channels," *IEEE Signal Processing Letters,* vol. 15, pp. 21-24, 2008.
[29] F. Pena-Campos, R. Carrasco-Alvarez, O. Longoria-Gandara, and R. Parra-Michel, "Estimation of fast time-varying channels in OFDM systems using two-dimensional prolate," *IEEE transactions on wireless communications,* vol. 12, pp. 898-907, 2013.
[30] P. P. Vaidyanathan, *Multirate systems and filter banks*: Pearson Education India, 1993.
[31] B. Farhang-Boroujeny, "OFDM versus filter bank multicarrier," *IEEE signal processing magazine,* vol. 28, pp. 92-112, 2011.
[32] C. Heil, "A discrete Zak transform," 1989.

[33] R. W. Chang, "Orthogonal frequency multiplex data transmission system," ed: Google Patents, 1970.
[34] B. Hirosaki, S. Hasegawa, and A. Sabato, "Advanced groupband data modem using orthogonally multiplexed QAM technique," *IEEE Transactions on Communications,* vol. 34, pp. 587-592, 1986.
[35] B. Saltzberg, "Performance of an efficient parallel data transmission system," *IEEE Transactions on Communication Technology,* vol. 15, pp. 805-811, 1967.
[36] H. Bölcskei, P. Duhamel, and R. Hleiss, "Orthogonalization of OFDM/OQAM pulse shaping filters using the discrete Zak transform," *Signal Processing,* vol. 83, pp. 1379-1391, 2003.
[37] P. Siohan, C. Siclet, and N. Lacaille, "Analysis and design of OFDM/OQAM systems based on filterbank theory," *IEEE transactions on signal processing,* vol. 50, pp. 1170-1183, 2002.
[38] L. Zhang, P. Xiao, A. Zafar, A. ul Quddus, and R. Tafazolli, "FBMC System: An Insight into Doubly Dispersive Channel Impact," *IEEE Transactions on Vehicular Technology,* 2016.
[39] G. K. Kaleh, "Channel equalization for block transmission systems," *IEEE Journal on Selected Areas in Communications,* vol. 13, pp. 110-121, 1995.
[40] N. Al-Dhahir, M. Uysal, and H. Mheidat, "Single-carrier frequency domain equalization," 2008.
[41] T. Zemen and C. F. Mecklenbrauker, "Time-variant channel estimation using discrete prolate spheroidal sequences," *IEEE Transactions on Signal Processing,* vol. 53, pp. 3597-3607, 2005.
[42] B. Le Floch, M. Alard, and C. Berrou, "Coded orthogonal frequency division multiplex [TV broadcasting]," *Proceedings of the IEEE,* vol. 83, pp. 982-996, 1995.
[43] A. Belouchrani, K. Abed-Meraim, J.-F. Cardoso, and E. Moulines, "A blind source separation technique using second-order statistics," *IEEE Transactions on signal processing,* vol. 45, pp. 434-444, 1997.
[44] J. H. Manton, "Modified steepest descent and newton algorithms for orthogonally constrained optimisation. part i. the complex Stiefel manifold," in *Sixth International Symposium on Signal Processing and its Applications,. 2001,* 2001, pp. 80-83.
[45] I. Raos, S. Zazo, and I. Arambasic, "Slepian pulses for multicarrier OQAM," in *Signal Processing Conference, 2006 14th European,* 2006, pp. 1-5.
[46] W. U. Bajwa, J. Haupt, A. M. Sayeed, and R. Nowak, "Compressed channel sensing: A new approach to estimating sparse multipath channels," *Proceedings of the IEEE,* vol. 98, pp. 1058-1076, 2010.
[47] F. Hlawatsch and G. Matz, *Wireless communications over rapidly time-varying channels*: Academic Press, 2011.
[48] L. Rugini and P. Banelli, "Windowing techniques for ICI mitigation in multicarrier systems," in *Signal Processing Conference, 2005 13th European*, 2005, pp. 1-4.
[49] L. Rugini, P. Banelli, and G. Leus, "Simple equalization of time-varying channels for OFDM," *IEEE communications letters,* vol. 9, pp. 619-621, 2005.

[50] F. J. Harris, "On the use of windows for harmonic analysis with the discrete Fourier transform," *Proceedings of the IEEE,* vol. 66, pp. 51-83, 1978.
[51] R. Bains and R. R. Müller, "Using parasitic elements for implementing the rotating antenna for MIMO receivers," *IEEE Transactions on Wireless Communications, ,* vol. 7, pp. 4522-4533, 2008.
[52] B. Zaidel and R. Muller, "On Adjacent Channel Interference Mitigation for Rotating MIMO Receivers," 2015.